Thallium Bromide as an Alternative Material for Room-Temperature Gamma-Ray Spectroscopy and Imaging

by

William Koehler

A dissertation submitted in partial fulfillment
of the requirements for the degree of
Doctor of Philosophy
(Nuclear Engineering and Radiological Sciences)
in The University of Michigan
2016

Doctoral Committee:

Professor Zhong He, Chair
Assistant Professor Marek Flaska, Pennsylvania State University
Professor Kimberlee Kearfott
Assistant Professor Kai Sun

To all the people who took time to explain how wrong I was, even when I was so sure I was right.

ACKNOWLEDGEMENTS

It is very clear to me that without the help and support of countless mentors, colleagues, family, and friends, none of this work would have been possible. I am especially grateful to my advisor, Professor Zhong He, who took a chance on a physics major from a liberal arts school with virtually no gamma ray detection experience. He consistently provided constructive feedback and, despite working long hours, was never too busy to discuss research ideas. His breadth of knowledge and critical understanding of fundamental principles was truly invaluable. I would also like to thank the rest of my committee members: Professors Kim Kearfott, Marek Flaska, and Kai Sun. They took time to understand my work and question my methods to ensure scientific rigor.

Equally important to the success of this work, was the collaborative and high-standard environment Professor He created in the Orion group. It has truly been a pleasure working with such insightful and creative minds. I would especially like to thank the students before me, Feng Zhang, Willy Kaye, Yuefeng Zhu, Miesher Rodrigues, and Crystal Thrall, for taking the time to answer my many questions and help me as I was getting started. Thank you to Sean O'Neal, who was a great sounding board, especially with the development of new techniques, and Jim Berry, whose electrical and machining knowledge is sprinkled throughout this thesis. I would also like to thank David Goodman and Bennett Williams for providing a thoughtful review of the first draft of this thesis. Finally, to the group members (and honorary group member) who transcended collaborators and became lifelong friends: Hao Yang,

Steven Brown, Jeff Fein, and Michael Streicher. You made my time in Ann Arbor not only scientifically rewarding, but also very fun.

I am also indebted to the many mentors and friends who influenced me before my University of Michigan career. From Kenyon College, Professor Terry Klopcic, Jon Edwards, Evan Pease, and Matt Siewny, and from Los Alamos National Laboratory, Dr. Steve Tobin.

It is impossible for me to overstate the gratitude I feel towards my family, without whom, none of this would be possible. My parents, Kurt and Mary, always supported me and encouraged me to follow my own path. They instilled in me a passion for learning which is still strong today. My brothers and sisters, Matthew, Kate, Damien, Anneliese, Mohan, and Richard, were equally supportive, even while they kept telling me to hurry up and move back to Portland. Finally, my deepest gratitude is for my future wife, Elizabeth, whose never-ending love and support was a true gift. You provided me with many escapes through countless adventures which did more to reset me emotionally and mentally than I realized at the time. There is more of you in this writing than you could know.

∗This work was funded by a Graduate Research Fellowship through the National Science Foundation and multiple contracts through the Domestic Nuclear Detection Office of the Department of Homeland Security.

TABLE OF CONTENTS

LIST OF FIGURES

Figure

LIST OF TABLES

Table

ABSTRACT

Thallium Bromide as an Alternative Material for Room-Temperature Gamma-Ray Spectroscopy and Imaging

by

William E. Koehler

Chair: Zhong He

Thallium bromide is an attractive material for room-temperature gamma-ray spectroscopy and imaging because of its high atomic number (Tl: 81, Br: 35), high density (7.56 g/cm^3), and a wide bandgap (2.68 eV). In this work, 5 mm thick TlBr detectors achieved 0.94% FWHM at 662 keV for all single-pixel events and 0.72% FWHM at 662 keV from the best pixel and depth using three-dimensional position sensing technology. However, these results were limited to stable operation at $-20\,^{\circ}$C. After days to months of room-temperature operation, ionic conduction caused these devices to fail. Depth-dependent signal analysis was used to isolate room-temperature degradation effects to within 0.5 mm of the anode surface. This was verified by refabricating the detectors after complete failure at room temperature; after refabrication, similar performance and functionality was recovered.

As part of this work, the improvement in electron drift velocity and energy resolution during conditioning at $-20\,^{\circ}$C was quantified. A new method was developed to measure the impurity concentration without changing the gamma ray measure-

ment setup. The new method was used to show that detector conditioning was likely the result of charged impurities drifting out of the active volume. This space charge reduction then caused a more stable and uniform electric field. Additionally, new algorithms were developed to remove hole contributions in high-hole-mobility detectors to improve depth reconstruction. These algorithms improved the depth reconstruction (accuracy) without degrading the depth uncertainty (precision). Finally, spectroscopic and imaging performance of new 11 x 11 pixelated-anode TlBr detectors was characterized. The larger detectors were used to show that energy resolution can be improved by identifying photopeak events from their Tl characteristic x-rays.

CHAPTER I

Introduction

1.1 Gamma Radiation

Gamma rays are high frequency ($> 10^{19}$ Hz) electromagnetic waves produced by nuclear de-excitation. Each isotope has unique energy levels governed by quantum mechanics; therefore, the emitted radiation energy, equal to the difference between the final and initial energy levels, is characteristic of the decaying isotope. As a result, an unknown radioactive sample can be identified by measuring the energy of the emitted characteristic gamma rays.

Unlike charged radiation (alpha-particles, beta-particles, and protons), gamma rays cannot be directly detected. Instead, they must transfer part or all of their energy to electrons through one of three major interactions: photoelectric absorption, Compton scattering, or pair production. Other interactions, (γ, p), (γ, n), (γ, f), etc., can also occur, but are unlikely at energies considered here (30 keV - 3 MeV).

Photoelectric absorption occurs when an incident gamma ray interacts with an absorber atom, transferring all of its energy (minus the binding energy) to the kinetic energy of an inner shell electron. This photoelectron then loses its energy to the detector material through Coulomb interactions. An outer shell electron quickly drops to fill the inner orbital, emitting a characteristic x-ray. The x-ray is usually captured close to the interaction site because of its short mean free path. The probability

of photoelectric absorption increases with the atomic number (Z) of the detector material:

$$P_{Photo} = C\frac{Z^n}{E_\gamma^{3.5}} \tag{1.1}$$

where C is a constant, E_γ is the incident energy, and n varies from 4 to 5 [1]. Photoelectric absorption preserves the most information about the gamma-ray energy, therefore, it is the preferred interaction for isotope identification. The strong dependence of photoelectric cross section on the atomic number, indicates that high-Z materials are desired for high-sensitivity gamma-ray spectroscopy.

Compton scattering occurs when a gamma ray interacts with an outer shell or 'free' electron, transferring a fraction of its energy to the electron. The scattered gamma-ray energy is related to its scattering angle by the Compton formula:

$$E' = \frac{E}{1 + \frac{E}{m_0c^2}(1 - \cos\theta)} \tag{1.2}$$

where E is the initial gamma-ray energy and θ is the scattering angle.

The final major interaction mechanism is pair production, which is most likely to occur at high gamma-ray energy and atomic number. A gamma ray undergoing pair production interacts with an atomic nucleus and is converted to an electron-positron pair. The threshold for this interaction is 1.022 MeV, the energy required to produce two particles each with 511 keV rest mass energy. Gamma-ray energy in excess of 1.022 MeV is transferred as kinetic energy to the electron-positron pair. Understanding the possible range of gamma-ray energies and how the gamma rays are going to interact with matter is critical for selecting detector materials.

1.2 Traditional Gamma-Ray Detectors

Inorganic scintillators and semiconductors are two material types traditionally used for gamma-ray detection and spectroscopy. Scintillators are generally cheaper,

easier to grow in large volumes, have faster timing characteristics, and better detection efficiency. On the other hand, semiconductor detectors typically have superior energy resolution.

1.2.1 Scintillators

Inorganic scintillators convert deposited gamma-ray energy into visible light by producing a photoelectron which loses energy through electron-hole pair generation. Generated electron-hole pairs are quickly trapped by intentionally-doped activator sites which de-excite through photon emission. Light is converted back to electrons at a photocathode. These electrons are accelerated through successively higher dynode voltages inside a photo multiplier tube (PMT). At each stage in the PMT, electrons gain enough kinetic energy from inner-dynode voltages to create secondary electron emissions when they strike the next dynode. Electron multiplication is required to amplify signals before preamplifier readout. During each readout stage (deposited energy to light conversion, light to photoelectrons, multiplication through the dynodes) proportionality is maintained. Therefore, the final number of electrons entering the preamplifier circuit immediately following the PMT, is proportional to the deposited energy and spectroscopy is possible. While maintaining proportionality is not required, it simplifies calibration and operation. Each readout stage degrades the energy resolution due to statistical fluctuations.

Inorganic scintillators are popular for high detection efficiency applications because of their relatively high atomic numbers (see Eq. 1.1), high densities, and ability to achieve large volumes. They also exhibit faster timing characteristics compared to semiconductors. Timing performance is limited by activator de-excitation times which can be as fast as 50 ns. The most widely used inorganic scintillator is thallium-doped sodium iodide (NaI(Tl)). Commercially available NaI(Tl) coupled to a PMT has achieved 7% FWHM at 662 keV [2]. Higher atomic number inorganic scintillators

like bismuth germinate (BGO) are more efficient than NaI(Tl), but have worse energy resolution. Of all inorganic scintillators, lanthanum bromide ($LaBr_3$(Ce)) exhibits the best energy resolution, achieving sub 3% FWHM at 662 keV [3].

1.2.2 Semiconductors

While scintillators are relatively cheap and easy to grow to large volumes, current energy resolution is limited to $\sim$ 3% FWHM at 662 keV due to the relatively large energy required to create electrons at the photocathode (W = 100 eV/electron) and larger Fano factor. Semiconductors, on the other hand, have a band structure with bandgap energies ranging from 0.6-3 eV, resulting in a lower average energy to produce a charge carrier (W = 3-6 eV/e-h pair). As a result, commercially available semiconductor detectors, most notably high purity germanium (HPGe), can achieve sub 0.2% FWHM at 662 keV [1], allowing better isotope identification, especially in the presence of many sources or high background. However, HPGe has a small bandgap (0.7 eV) and requires cooling to liquid nitrogen temperatures (77 K) to reduce thermally-generated leakage current. Larger bandgap semiconductors like thallium bromide (TlBr) and cadmium zinc telluride (CZT) can operate at room-temperature without significant thermal noise.

In semiconductors, high-energy electrons or positrons created via photoelectric effect, Compton scatter, or pair production create secondary electron-hole pairs inside the active volume. A bias voltage is applied across the semiconductor to collect the generated charge at the electrodes. Because the number of generated electron-hole pairs is proportional to deposited energy, spectroscopy is possible. Again, proportionality is not necessary, but greatly simplifies calibration.

1.3 Room-Temperature Gamma-Ray Spectrometers and Imagers

Gamma ray detection and imaging is important for nuclear security and safeguards, reactor operation, and radiological cleanup because, as described above, characteristic gamma rays provide a unique signature of radioactive material. For example, using gamma-ray spectroscopy and imaging, border security inspectors can locate and identify weapons material from natural occurring radioactive material (NORM), reactor operators can locate and remove holdup in processing pipes, and cleanup specialists can identify and prioritize contaminated areas based on the relative danger of different contaminants. In each of these examples, added imaging capabilities decreases identification time and reduces dose to operators.

Large bandgap semiconductors can operate at room temperature because of low thermal noise. Room-temperature operation allows for better portability and much faster 'turn on' times (time between when the device is turned on and when it is ready for use). The cooling time for HPGe can be as long as 24 hours, greatly increasing its turn on time. Commercially available CZT detectors are ready for use less than three minutes after the device is turned on [4]. In all three examples above, except for possibly border security where detectors can be stationary, portability and fast turn on times are extremely advantageous.

CZT is the most mature room-temperature semiconductor detector material [5, 6, 7, 8, 9]. The large bandgap (1.64 eV) is sufficient to reduce thermal excitation and allow room-temperature operation. Pixelated detectors using digital readout can achieve 0.4% FWHM at 662 keV for single-pixel events [10].

1.4 Thallium Bromide

1.4.1 Advantages of TlBr

Thallium bromide (TlBr) is an alternative room-temperature semiconductor detector material. Table 1.1 shows a comparison of material properties between TlBr and other popular semiconductors. Compared to CZT, TlBr has a significantly higher effective atomic number (~ 80 compared to ~ 50 for CZT) and density. This results in much greater stopping power for high-energy gamma rays, increasing efficiency by about a factor of 3 at 662 keV. Additionally, the higher effective atomic number increases the expected photo-fraction at 662 keV (see Eq. 1.1) from ~ 0.12 for CZT to ~ 0.37 for TlBr. Finally, the melting point for TlBr is only 460 °C and it has a simple cubic structure; therefore, simple melt-based techniques like the traveling motlen zone (TMZ) method can be used for both growth and purification [11, 12]. These properties should reduce the cost of TlBr compared to CZT.

Like all other materials in Table 1.1, the principle advantage of TlBr over HPGe (or Ge) is the large bandgap, which allows for room-temperature operation without significant thermal noise. Additionally, due to its low atomic number, Ge typically has a much lower photo-fraction compared to other materials in Table 1.1. HgI_2 is the most similar to TlBr and was also investigated by researchers because of its high density and the high atomic number of Hg [13, 14, 15]. However, consistent sub-1% FWHM at 662 keV has not been demonstrated and the devices must undergo a substantial conditioning phase at every bias [16, 17, 18].

1.4.2 TlBr Development: Previous Work and Current Technology State

In 1947, Robert Hofstadter was the first to experimentally demonstrate that thallium halides could be used as radiation counters [19]. His first sample was 2 mm thick and was comprised of 40% TlBr and 60% TlI. The detector showed a Ra response

Table 1.1: Material comparison between popular semiconductor detectors.

Material	Atomic Number	Density (g/cm^3)	Bandgap (eV)	W (eV/pair)
Ge	32	5.33	0.72	3.6
HgI_2	80, 53	6.4	2.13	4.2
CdZnTe	48, 30, 52	6.1	1.64	4.7
TlBr	81, 35	7.6	2.68	5.5

after it was annealed at 350 °C and operated at −115 °C. In 1984, Hofstadter also showed that TlBr could provide spectroscopy and achieved 19% FWHM for ^{241}Am alpha particles.

In 1990, Shah et al. improved crystal quality through zone purification techniques and were able to manufacture 0.5-0.7 mm thick TlBr detectors with electron and hole mobility-lifetime products ($\mu_e\tau_e$ and $\mu_h\tau_h$) in the 10^{-6} cm^2/V range [20]. They calculated the electron-hole pair generation energy to be 6.5 eV. Throughout the 1990s and early 2000s, most TlBr development focused on increasing $\mu\tau$ through various growth, purification, and annealing techniques [21, 22, 23, 24]. By 2005, $\mu_e\tau_e$ reached 10^{-3} cm^2/V range, approaching CZT values [25]. Fig. 1.1a (copied from Ref. [26] but updated to include results from this work) shows the evolution of $\mu\tau$ for both electrons and holes [11, 20, 21, 22, 23, 24, 27, 28]. Similarly, Fig. 1.1b shows the 662 keV energy resolution over time, broken up by detector type [11, 12, 24, 27, 28, 29, 30, 31, 32]. Over the past fifteen years there has been significant improvement in both $\mu\tau$ and energy resolution, making TlBr a viable alternative room-temperature semiconductor detector material.

As shown in Fig 1.1b, TlBr has made significant progress and can now achieve sub-1% energy resolution at 662 keV. However, these results are mostly limited to −20 °C operation where the detector is stable [32]. After days to months of room-temperature operation, the detectors start to degrade (photopeak centroids decrease and energy resolution gets worse) and ultimately fail. The failure, or polarization, is

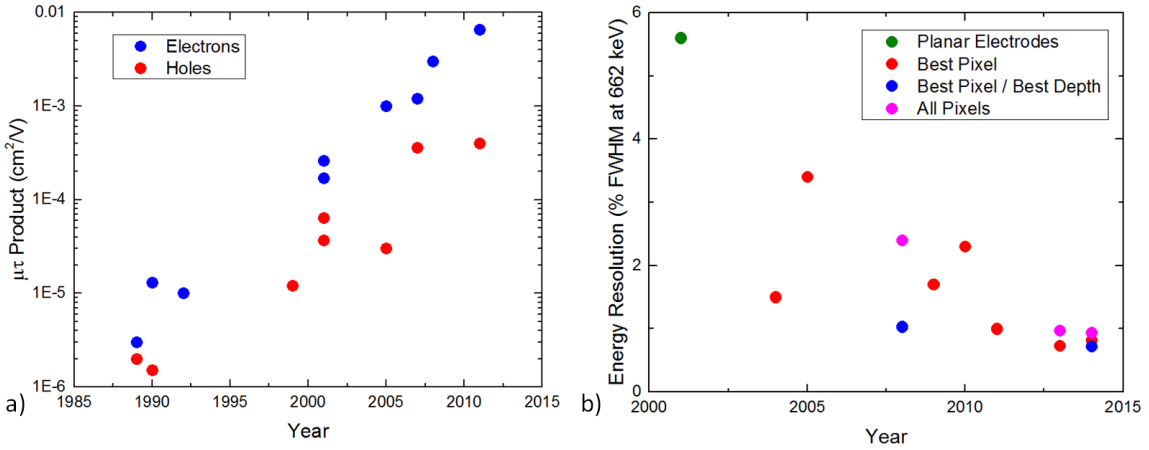

Figure 1.1: a) Evolution of mobility-lifetime product for electrons and holes. b) Energy resolution improvement throughout TlBr development. The colors indicate detector and electrode type.

characterized by saturated leakage currents on both the cathode and anode electrodes and no measurable preamplifier signals. The prevailing theory suggests that Tl^+ and Br^- (or their respective vacancies) migrate as a result of the electric field, inducing ionic conduction [33, 34]. According to the theory, the ionic current results in space charge buildup under the electrodes, creating an electric field in the opposite direction of the applied field. Eventually, the internal field is not strong enough to collect the generated electrons before significant trapping occurs [25, 30, 33, 35]. More recent work concludes that Br vacancies (V^+_{Br}) are the dominate cause of ionic conduction. When the V^+_{Br}s reach the cathode, charge is injected at the anode by the creation of Au-Br bonds. This creates a barrier region at the surface which eventually causes polarization [36]. This is consistent with work showing that failure mechanisms occur near the electrodes [37].

Stable room-temperature operation has been achieved by applying Tl electrodes [30] and periodically switching the bias polarity [38]. Unfortunately, Tl is extremely toxic, complicating the electrode fabrication process. Additionally, stable performance for longer than three days has not been experimentally demonstrated without switching the bias polarity. Further study is required to determine whether Tl

electrodes can achieve long-term (months) room-temperature stability. Periodically switching the bias is undesirable for pixelated detectors, in which the anode must be pixelated for optimal signal generation. Working from the hypothesis that electrode material is chemically interacting with the bulk, researchers have tried various surface preparations and different electrode metals [36, 39, 40]. This work has shown some promise, but is currently limited to planar devices and alpha-particle characterization. Despite attempts to reduce room-temperature polarization, the most consistent way to achieve long-term operation is to cool the detector to $-20\,^{\circ}\mathrm{C}$ where ionic current is reduced by two orders of magnitude.

1.5 Contributions of this Work

This work addresses the unique challenges of applying pixelated CZT methodology and data processing to TlBr. Contributions were made to characterizing the underlying mechanisms that cause conditioning and polarization in TlBr and improving $-20\,^{\circ}\mathrm{C}$ performance. In the process, three new methods were developed and are detailed in Chapter III.

Underlying differences between charge generation in CZT and TlBr was explored through simulations in Chapter IV. Results were used to predict optimal pixel sizes which minimize both single-pixel, double-interaction events and charge sharing events. Both types of events are considered misclassification. Additionally, a correction factor for calculating the mobility-lifetime product in single-polarity charge-sensing detectors with non-ideal weighting potentials was created and calculated for different electrode configurations.

Chapter V characterizes the performance of $-20\,^{\circ}\mathrm{C}$ operation and details implementation of newly developed algorithms to account for hole motion in high-hole-mobility detectors. These algorithms were used to improve depth reconstruction from the cathode-to-anode ratio. The depth reconstruction accuracy was compared to un-

filtered and timing methods using a collimated fan beam. Additionally, a new method was developed using LED stimulation to simultaneously measure material proprieties (resistivity, mobility, trapping site concentration) and detector characteristics (electron drift time, signal deficit, spectroscopic performance). This method was used to determine that conditioning in cooled TlBr detectors was caused by trapped charge redistribution which improves the internal electric field.

Improvement and understanding of TlBr detectors at room temperature is detailed in Chapter VI. Depth-dependent signals were used to isolate polarization degradation to within 0.5 mm of the anode surface. Detectors were refabricated after some surface material was removed to verify that bulk material was unaffected by polarization. Return to performance after refabrication was demonstrated.

Finally, in Chapter VII, the methodology developed for 3 x 3 pixelated detectors was applied to new 11 x 11 pixelated detectors. These detectors were tested in a new single-module digital ASIC system with a two-stage peltier cooler designed to maintain $-18\,^{\circ}\mathrm{C}$ operation. Using this system, gamma ray imaging was demonstrated for the first time with TlBr.

CHAPTER II

Theory

2.1 The Shockley-Ramo Theorem

The Shockley-Ramo theorem [41, 42] provides a simple method to calculate time-dependent induced signals on any electrode due to moving charge in a radiation detector. The theorem states that induced charge on an electrode is equal to generated charge (q) multiplied by the electrode's weighting potential (ϕ_0) at q's location:

$$Q = -q \cdot \phi_0(z) \tag{2.1}$$

where z is the interaction depth from the anode. A similar expression can be written for the induced current:

$$i = q \cdot v \cdot E_0(z) \tag{2.2}$$

where v is the drift velocity and E_0 is the weighting field. The weighting potential and field are the electric potential and field under the following conditions:

1. The electrode of interest is set to 1 V
2. All other electrodes are set to 0 V
3. All space charge is ignored.

In a typical radiation detector, electrodes are connected to charge sensitive preamplifiers which measure the change in induced charge. Therefore, the total measured induced charge is equal to the generated charge times the change in weighting potential the charge moves through:

$$\Delta Q = -q \cdot [\phi_0(z_f) - \phi_0(z_i)] \tag{2.3}$$

In the special case of constant drift velocity (v_d), the time-dependent induced signal is:

$$Q(t) = -q \cdot [\phi_0(z_i + v_d t) - \phi_0(z_i)]. \tag{2.4}$$

For more complicated drift velocities ($v_d = v_d(z)$), it is easiest to solve Eq. 2.3 iteratively, using $z_{i+1} = z_f$ and $z_{f+1} = z_f + v_d(z_f) \cdot \Delta t$. In either case, the Shockly-Ramo theorem provides a simple method to calculate induced signals on any electrode for even the most complex electrode configurations.

Fig. 2.1a shows a pixelated electrode configuration similar to the one used in this work. The cathode was planar and the anode (positive electrode) was sub-divided into an array of pixels. Using the Shockley-Ramo theorem, the cathode weighting potential was calculated by setting the cathode voltage to 1 V and all anode pixel voltages to 0 V. The red curve in Fig. 2.1b shows the resulting linear weighting potential. The anode weighting potential was calculated by setting a single anode pixel voltage to 1 V, all other anode voltages to 0 V, and the cathode voltage to 0 V. The resulting weighting potential has a small slope through most of the bulk and increases rapidly to one near the anode, as shown in the blue curve of Fig. 2.1b.

Consider an interaction which occurs at location a in Fig. 2.1, closer to the cathode. As electrons drift toward the anode and are collected, they induce a signal proportional to the weighting potential change they drift through. The red arrow in

Fig. 2.1b shows the change in cathode weighting potential and the blue arrow shows the change in anode weighting potential. The same analysis holds for an interaction which occurs at location b, closer to the anode. Hole drift is ignored for this simple analysis because in TlBr, CZT, and most other room-temperature semiconductors $\mu_h\tau_h << \mu_e\tau_e$ and the holes do not contribute significantly to the signal.

Because the anode weighting potential has a small slope through most of the bulk, the anode weighting potential change is approximately one for both interactions (both blue arrows in Fig. 2.1b have approximately unit length). Therefore, from Eq. 2.3, the induced charge ΔQ on the pixelated anodes is equal to the generated charge q, regardless of the interaction depth. A pixelated configuration is said to be single-polarity charge sensing because most of the charge is induced near the anode; any holes moving toward the cathode do not go through a significant weighting potential change, and therefore do not contribute to the anode signal. Because the initial generated charge is proportional to the deposited energy (see Sec. 1.2.2), the anode voltage amplitude is also proportional to the deposited energy:

$$V_A = \frac{\Delta Q}{C_A} = \frac{N \cdot e_0}{C_A} \propto E_{dep} \tag{2.5}$$

where N is the number of electron-hole pairs generated by the incident radiation and C_A is the anode preamplifier feedback capacitance. Anode signals from multiple events can be histogramed to form energy spectra and the pixelated detector can be used to do spectroscopy.

The cathode signal induction (red arrows in Fig. 2.3b), is proportional to both interaction depth and deposited energy because of the linear weighting potential. Therefore:

$$V_C = \frac{N \cdot e_0 \cdot z}{C_C} \propto E_{dep} \cdot z \tag{2.6}$$

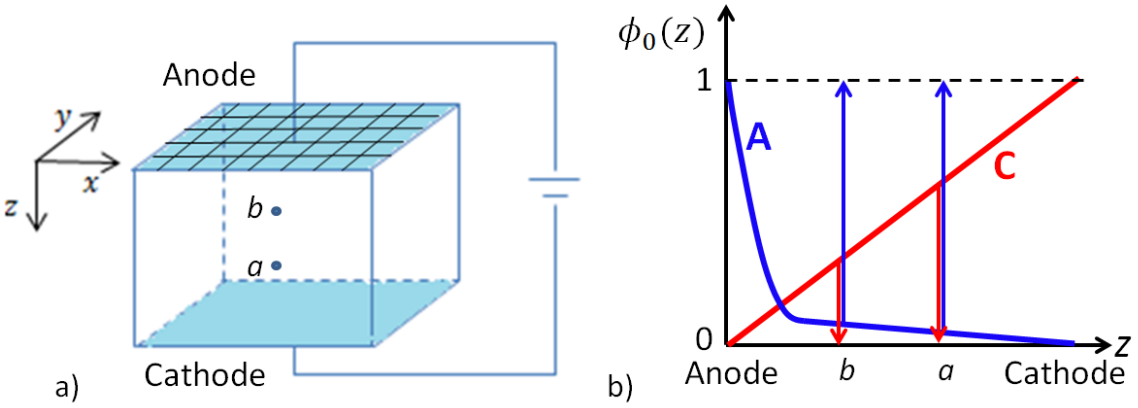

Figure 2.1: a) Schematic of a pixelated detector similar to the one used in this work. b) Hand-drawn approximation of the cathode (red) and anode (blue) weighting potentials. The arrows show the weighting potential change the electrons drift through when they are collected by the anode.

where C_C is the cathode preamplifier feedback capacitance and z is the distance from the anode electrode.

Because anode signals are proportional to deposited energy and cathode signals are proportional to deposited energy and interaction depth, the cathode-to-anode-signal-ratio (CAR) can be used to determine the gamma-ray interaction depth:

$$CAR = \frac{V_C}{V_A} = \frac{Ne_0C_Az}{Ne_0C_C} = A \cdot z \tag{2.7}$$

where A is a constant.

The CAR method to determine the depth of interaction was developed by He et. al and was first applied to coplanar grid detectors [43]. Later, it was applied to pixelated-anode detectors [6]. While anode signals are largely unaffected by hole motion, cathode signals increase with high-hole-mobility material. If this occurs, cathode signals are overestimated and the CAR is no longer proportional to interaction depth. Removing hole contributions to properly reconstruct interaction depths in high-hole-mobility detectors is discussed in Sec 3.3.2.

2.2 Depth Correction

When an electron cloud drifts to the anode, some charge is lost as a result of trapping. Additionally, events not at the cathode surface do not drift through the full anode weighting potential because the weighting potential is small but not negligible in the bulk. Therefore, the true induced signal can be estimated by:

$$\Delta Q(z) = q \cdot (1 - \phi(z)) \cdot \exp\left(\frac{z}{\mu_e \tau_e E}\right) \tag{2.8}$$

where $(1 - \phi(z))$ accounts for weighting potential loss and $\exp\left(\frac{z}{\mu_e \tau_e E}\right)$ accounts for trapping loss. As a result of these depth-dependent losses, the raw (no depth-correction) photopeak is widened, resulting in degraded energy resolution. Fig. 2.2a shows an example of a raw 662 keV spectrum from a 5 mm thick TlBr detector. The raw energy resolution was 4% FWHM at 662 keV.

The CAR was used to separate the energy spectrum into multiple CAR depth bins, as shown in Fig. 2.2b. There was a clear depth-dependence in the photopeak centroids that resulted in poor raw resolution. A unique gain, determined during calibration, was applied to each count in the spectrum depending on its CAR-estimated depth. By applying the depth correction, the photopeaks were moved to the solid blue line in Fig. 2.2b.

The final depth-corrected spectrum is shown in Fig. 2.2c. As a result of the individual gains applied to each CAR depth, the energy resolution improved to 1.24% FWHM. Using the interaction depth, weighting potential and trapping effects were corrected. The amount of improvement between raw and corrected performance depends on the amount of trapping within the detector material, which varies even within a single detector's volume.

In addition to correcting photopeak centroids and improving energy resolution, depth sensing is very useful for diagnosing resolution degradation effects. Through-

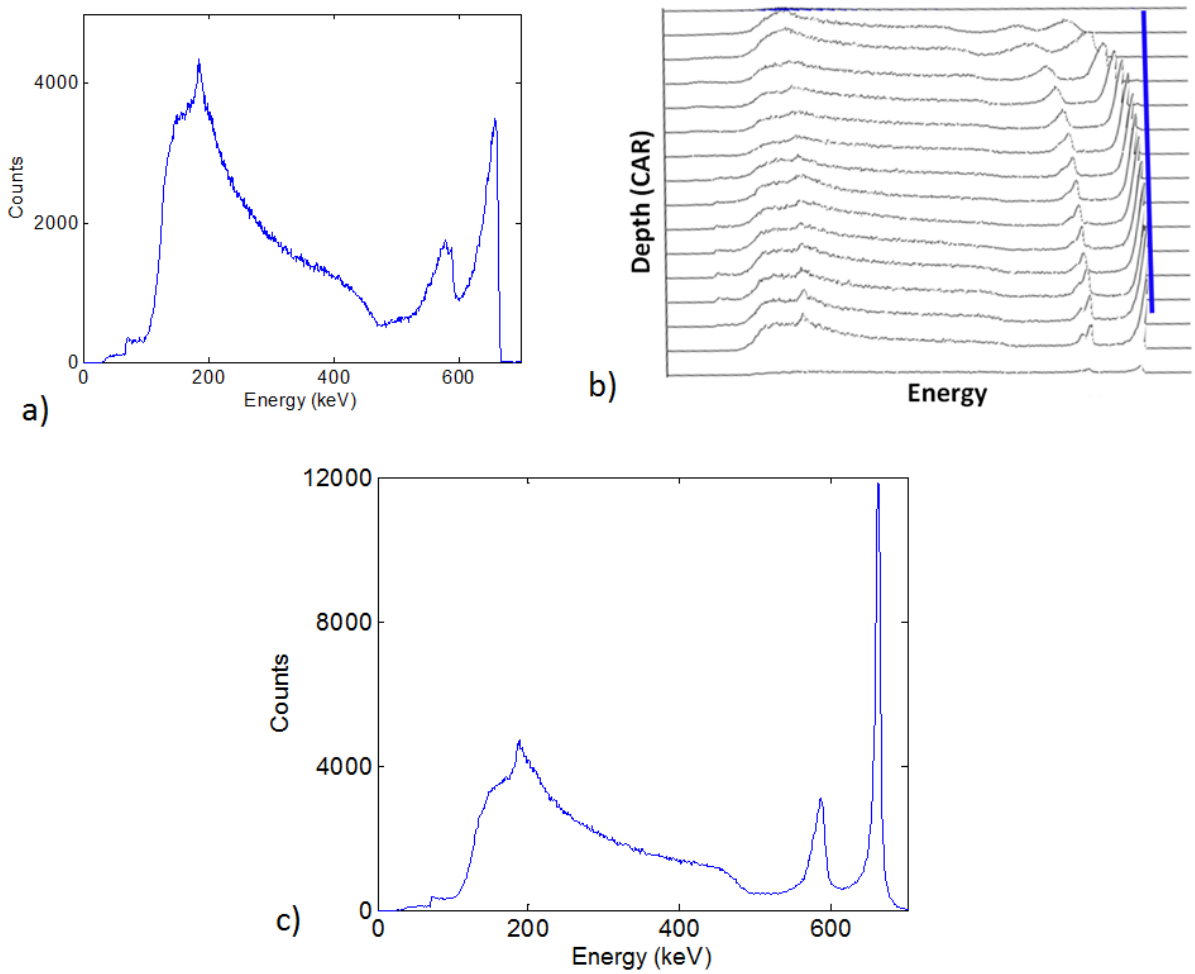

Figure 2.2: a) Raw energy spectrum from a mono-energetic ^{137}Cs source. b) Same energy spectrum broken up into different CAR (depth) bins. c) Depth corrected spectrum obtained by applying a gain to each CAR bin, aligning the photopeaks. The energy resolution improves from 4% to 1.24% FWHM at 662 keV.

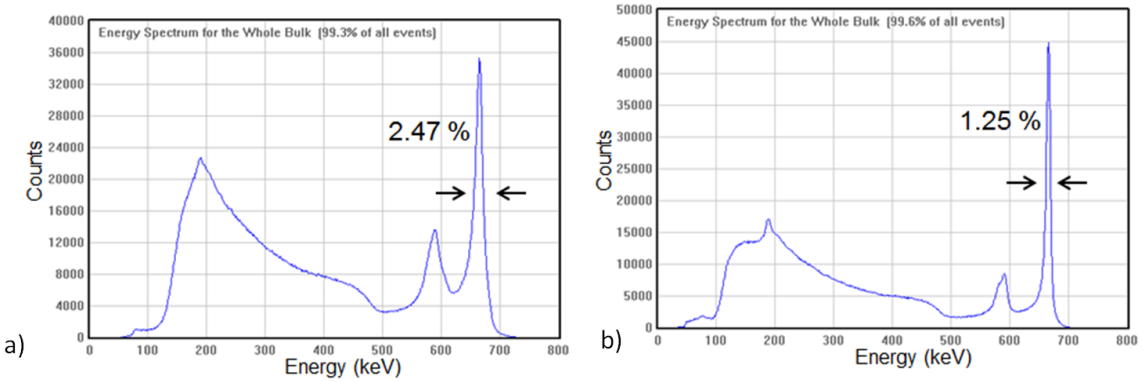

Figure 2.3: Single-pixel spectra for detector 935-34-AA2L (a) before and (b) after 2 mm was removed from the cathode side. The energy resolution improved from 2.47% to 1.25% FWHM at 662 keV after the poor region was removed.

out this work, the CAR was used to analyze depth-dependent photopeak centroids and resolution, and differentiate bulk degradation from surface degradation. For example poor energy resolution and low photopeak centroids near the cathode surface of detector 935-34AA2L indicated poor charge collection efficiency within 2 mm of the cathode surface, likely the result of heavy trapping. Fig. 2.3 shows the single-pixel energy spectra before and after the heavy-trapping region was removed. The energy resolution improved from 2.47% to 1.25% FWHM at 662 keV, indicating that depth-dependent analysis was able to identify the presence and extent of the heavy-trapping region. Using the CAR to correct for trapping and weighting potential effects, as well as separate bulk and surface degradation has been previously applied to CZT and TlBr [44, 45, 46].

So far, depth sensing has only been discussed for single-pixel interactions. However, it is possible (and common) for a gamma ray to Compton scatter under one pixel and undergo photoelectric absorption under another pixel. This results in two pixels collecting charge from a single gamma-ray event and is referred to as a two-pixel event. In this case, the CAR cannot provide the interaction depth because only one cathode signal is recorded (the planar cathode is shared by all pixels). For multiple-pixel events, electron drift times are used to calculate interaction depths. Because of

the linear cathode weighting potential, the cathode triggers right when the electron cloud starts to drift. In contrast, the anode triggers only when the electron cloud is collected because the anode weighting potential is close to zero throughout most of the bulk. Therefore, drift times can be calculated as the difference between anode and cathode trigger times. Event closers to the cathode will have longer drift times compared to center or anode-side events. Single-pixel events are used to correlate drift times from multiple-pixel events to CAR, and ultimately interaction depth. The drift time method to determine interaction depth for multiple-pixel events is discussed in great detail in Ref. [44].

Using CAR and drift time, interaction depths for any event can be determined. Additionally, because anode amplitudes are proportional to deposited energies, and x and y locations can be determined by the triggered pixel, pixelated CZT and TlBr detectors are 3-dimensional position and energy sensitive.

2.3 Compton Imaging

As discussed in Chapter I, imaging radiation sources is critical for border security, nuclear safeguards, contamination cleanup, and power plant safety. Compton imaging provides a straightforward method to image 400 keV to 3 MeV radiation sources [47, 48]. The Compton scattering formula (Eq. 1.2) can be rewritten as:

$$\cos(\theta) = 1 - \frac{m_o c^2 E_1}{E_0(E_o - E_1)} \tag{2.9}$$

where θ is the scattering angle, E_1 is the energy deposited in the first interaction and E_0 is the incident energy (sum of all depositions for photopeak events). Knowing the scattering angle from Eq. 2.9 and axis defined by the 3D locations of the Compton scatter and next interaction from depth sensing, limits the incident direction to a cone, referred to as a Compton cone. Fig. 2.4 (copied from Ref. [49]) illustrates a

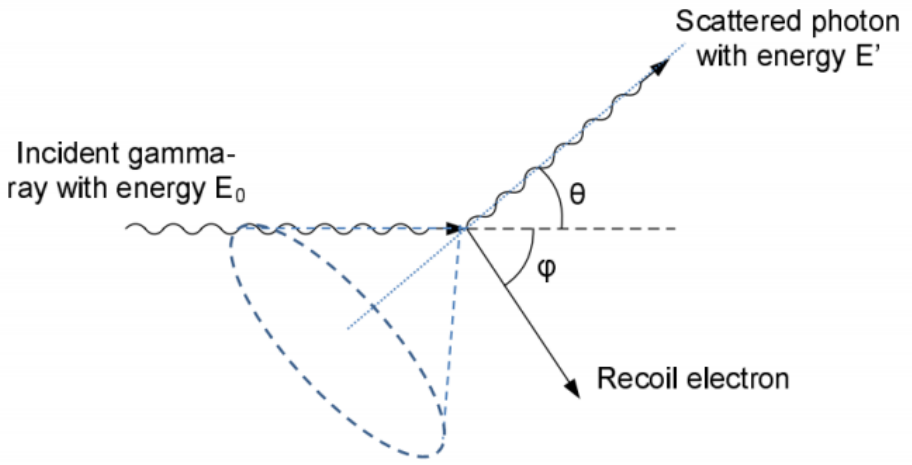

Figure 2.4: Example of a Compton interaction and corresponding Compton cone.

Compton interaction and the corresponding Compton cone.

When Compton cones are projected onto 2D spherical coordinates of 3D space, Compton rings are formed. The sum of overlapping Compton rings from many events produce a radiation image with hot spots (high overlap regions) corresponding to the spacial distribution of gamma ray emission. Compton imaging has been successfully implemented using a single CZT detector [4, 50] and more complex array systems [49, 51, 52].

CHAPTER III

TlBr Detector Fabrication and Characterization Methodology

3.1 Detector Fabrication

All TlBr discussed in this work was grown by Radiation Monitoring Devices Inc. (RMD). 5N-pure starting TlBr, purchased from a vendor, was purified and grown using the Traveling Molten Zone (TMZ) method. During pre-growth TMZ purification, a heater was used to melt a portion of the TlBr as it moved down the crystal (see Fig. 3.1a). The impurity solubility was greater in the liquid TlBr compared to the solid TlBr, causing impurities to concentrate in the melted region. As the melt moved down the crystal, it pulled impurities with it. At the end of the purification process, the seed (left side of Fig. 3.1b) had a much lower impurity concentration compared to the tail (right side of Fig. 3.1b). Therefore, detectors made from the seed end were expected to perform better than detectors from the tail end. During purification, the heater was moved relatively quickly (50 mm/hr) because material structure was unimportant. After zone refining, the heater speed was reduced to 2.5-5 mm/hr for one final pass to ensure a single TlBr crystal. Fig. 3.1b shows a TlBr ingot after purification and growth.

After crystal growth, the ingots were cut with a wire saw, lapped, and polished

with 3 μm grain Al_2O_3 paper. Before the electrodes were applied, the crystals were etched in 5-20% bromine in menthol, depending on the selected surface treatment. The electrodes were deposited in an evaporation chamber using a shadow mask. For most detectors, a 20 nm layer of Cr was applied to help mitigate chemical reactions between the contact and electrode. Finally, an 80 nm Au layer was applied as the main electrode material.

Two detector types were used in this work. The first was nominally 5 x 5 x 5 mm^3 with a 3 x 3 pixelated anode and planar cathode (see Fig. 3.2a). The anode shadow mask was a 4 x 4 pattern but the outer pixels on two sides were bonded together to form a guard ring (see Fig. 3.2b). An additional thin guard ring also circumscribed the entire anode. Because only inner 3 x 3 pixels were read out, the device active volumes were reduced to 45 mm^3. The pixel pads were 0.9 x 0.9 mm^2 with 1 mm pixel pitch. Therefore, a 100 μm gap existed between pixels. Each anode pixel was hand wired to the ceramic substrate board using fine palladium wires and carbon paste. As a result, the 3 x 3 pixelated detectors were very fragile..

The second detector type was a much larger 12 x 12 x 5 mm^3 detector with 11 x 11 pixelated anodes. The anodes had the same 0.9 x 0.9 mm^2 pixel pad area and 1 mm pixel pitch. A thin guard ring surrounded the anodes (see Fig. 3.2c). These detectors were flip-chip bonded to substrate boards compatible with the CZT Polaris systems [44], by Polymer Assembly Technology. A fully assembled 11 x 11 detector is shown in Fig. 3.2d. Due to bonding, only a single wire (cathode) was used on the entire detector, resulting in much more robust devices.

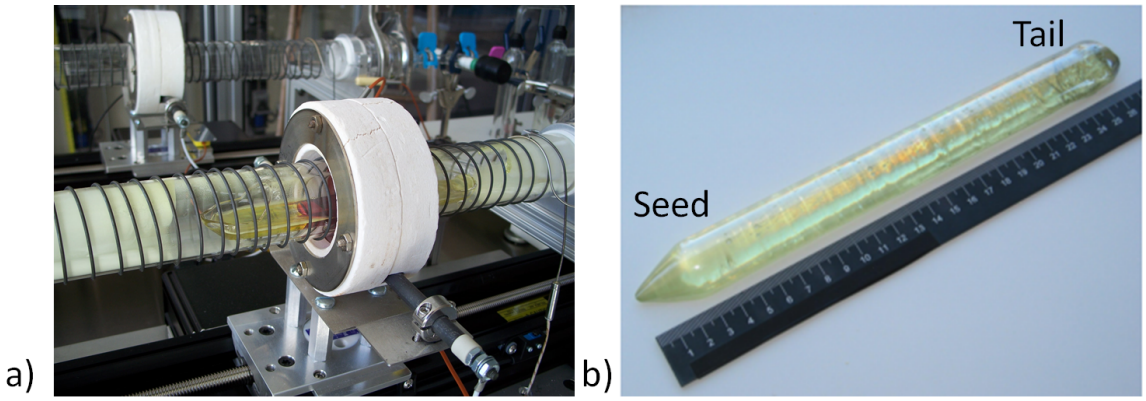

Figure 3.1: a) TMZ apparatus and b) final crystal. Images courtesy of A. Churilov and Y. Ogorodnik from RMD.

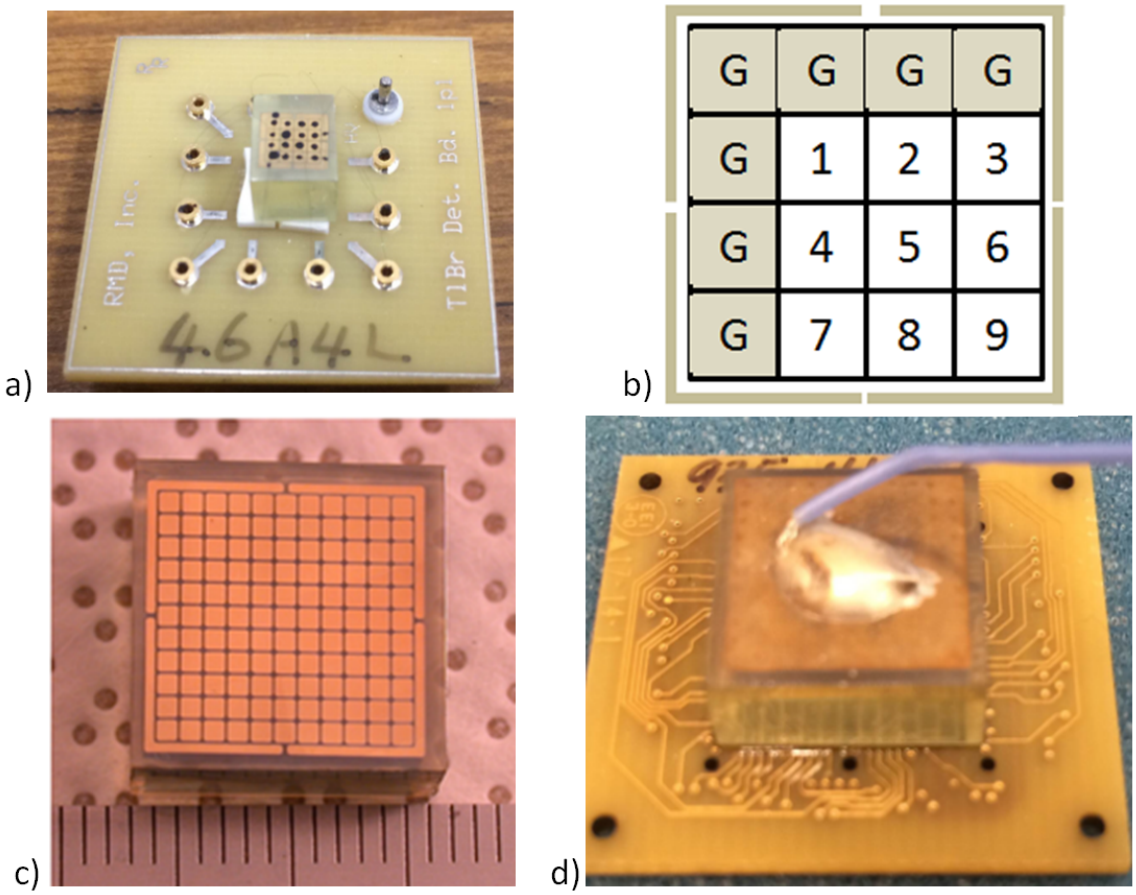

Figure 3.2: a) 3 x 3 pixelated detector mounted to a ceramic substrate. Fine palladium wires connected the anodes to the substrate. b) Schematic of the 3 x 3 anode layout. Two lines of outer pixels were bonded together to form a larger guard ring. c) 11 x 11 pixelated anode before filp-chip bonding. d) Assembled 11 x 11 detector. The cathode wire is the only wire on the device.

3.2 Experimental Setup

3.2.1 3 x 3 Pixelated Detector Standard Readout

As described in Section 3.1, two detector types were used throughout this work: 3 x 3 pixelated detectors and 11 x 11 pixelated detectors. As a result, two readout systems were required. The 3 x 3 detectors were read out using a custom printed circuit board (see Fig. 3.3 for board layout). The nine pixelated anodes and planar cathode signals each had individual eV-Product 5093 preamplifiers attached to the PCB board. The board and preamplifiers were enclosed in an Al box that was placed into a Thermotron S-1.2-3200 environmental chamber for precise temperature control ($< 0.1\,^{\circ}$C deviation). The preamplifier outputs were digitized by computer operated 14-bit Gage cards which could sample from 1 kHz to 125 MHz depending on the application. During most testing, the waveforms were digitized in 512 points sampled every 100 ns (10 MHz), yielding a total collection time of 51.2 μs. The 3 x 3 detectors were used for in-depth material characterization, determining performance capabilities, diagnosing degradation effects, and testing new algorithms. As a result, the Gage card versatility was required.

Fig. 3.4a shows a picture of the Al test box and PCB board. The preamplifiers were connected to the underside of the board. Fig. 3.4 shows a block diagram of the 3 x 3 pixelated detector system setup. The HV power supply was connected to the cathode through a noise filtering circuit and protective capacitor. A 6 V power supply was used to power the preamplifiers.

3.2.2 3 x 3 Pixelated Detector Collimator and LED Readout

New algorithms were developed as part of this work to account for the motion of holes in some TlBr detectors to properly reconstruct interaction depths. A thin slit collimator was used to expose a single depth to 662 keV gamma rays. Therefore,

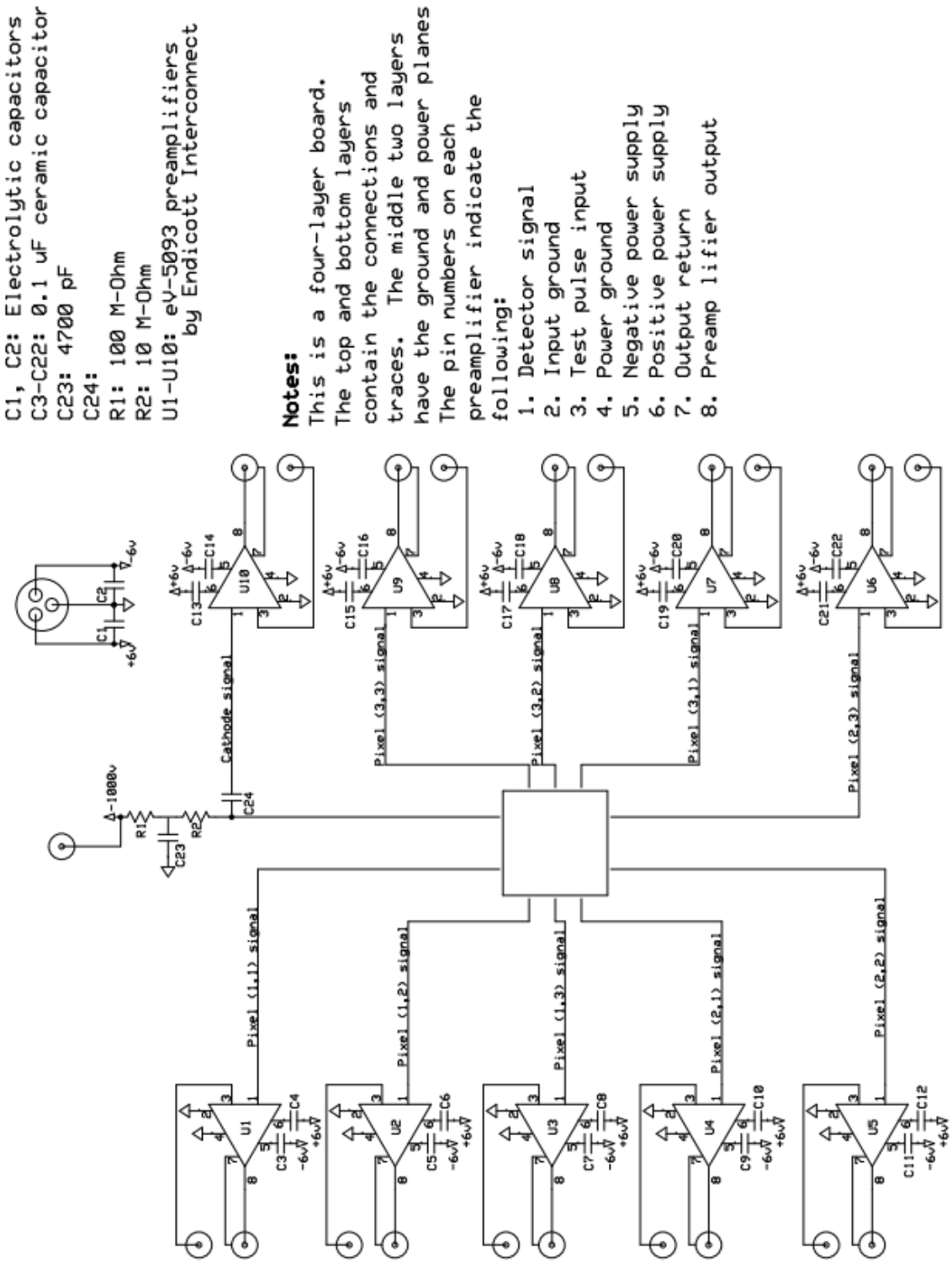

Figure 3.3: Printed circuit board schematic. The detector was placed in the center and each channel (nine anodes and cathode) had its own preamplifier.

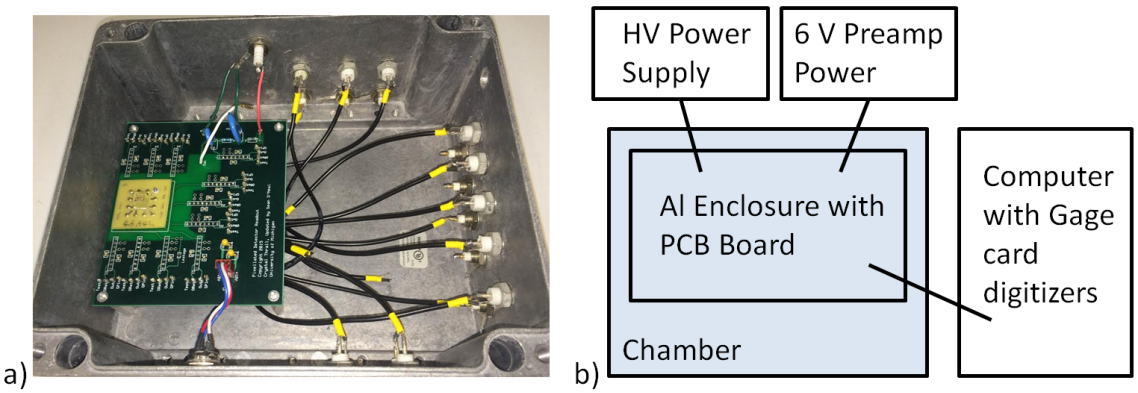

Figure 3.4: a) Picture of the Al enclosure and PCB board. b) Block diagram of the 3 x 3 experimental setup.

the true interaction depth was known from the collimator position and true depths were compared to reconstructed depths from different reconstruction algorithms. The collimator was comprised of two, 4 cm thick slabs of tungsten, separated by 100 μm, and controlled by a positioning stage with 0.01 mm precision. The collimator system was placed inside the environmental chamber, directly next to the Al enclosure. Due to the Al enclosure geometry, the side faces of the detectors were approximately 2 cm from the collimator and 6 cm from the gamma-ray source. A block diagram of the collimator setup is shown in Fig. 3.5a.

An LED method was developed to map trapping concentrations as a function of time during operation. The method used the setup described in Sec. 3.2.1 but with a 2.1 eV (sub-bandgap) LED right at the surface of the (optically transparent) TlBr detectors. The LED was powered by a separate power supply system that monitored the current; therefore, the light intensity was precisely controlled. Fig. 3.5b shows the LED setup. For some experiments, the 2.1 eV LED was replaced with a 3.1 eV (above bandgap) LED.

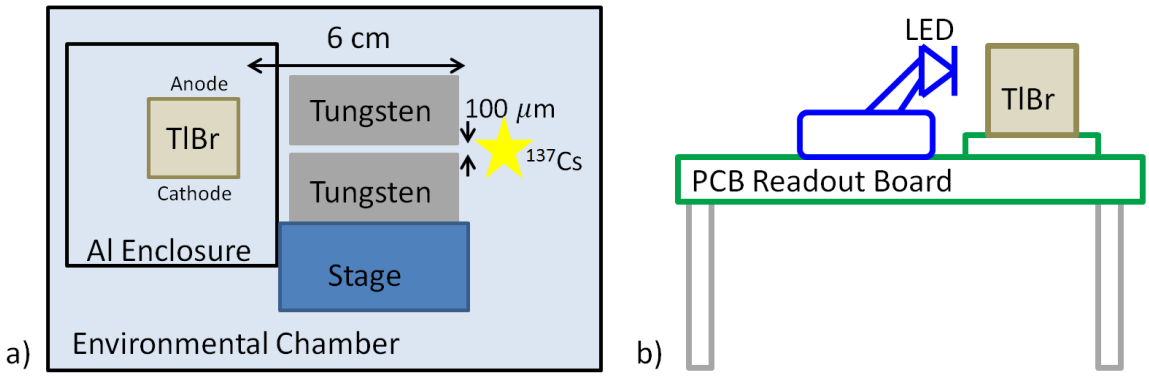

Figure 3.5: a) Block diagram of the collimator setup used to ensure gamma-rays interactions at a single depth. b) Standard setup with an added LED to determine trapping concentrations.

3.2.3 11 x 11 Pixelated Detector Standard Readout

The 11 x 11 detector readout was done with an IDEAS Application-Specific-Integrated-Circuit (ASIC) similar to the one described in detail in Ref. [53]. Detectors were flip-chip bonded and mounted to a substrate with three, 42-pin connectors. Detectors were connected to a front end card with an embedded 128 channel UM-VAD ASIC designed for CZT readout. Each channel preamplifier was capable of sampling 160 points from 5 to 80 MHz depending on the application and detector material. The longest drift time (cathode-side events) for electrons in 5 mm thick detectors with 1000 V bias is approximately 8-10 μs. Therefore, a 5 MHz sampling frequency was typically used. This resulted in 32 μs sampling windows that captured the entire cathode waveforms.

ASICs were connected to an IDEAS Espresso board which housed the receivers, ADC, and FPGA, via a flexible ribbon cable. The receivers converted current pulses from the ASICs into voltage pulses for the ADC while supplying voltages and control signals to the ASICs. An off-the-shelf ZED board was used as a gateway between the Espresso board and computer. The ZED board also contained a CPU which could be used for data processing in the future; for the work presented here, the CPU capabilities were unused. Fig. 3.6 shows a block diagram of the 11 x 11 data

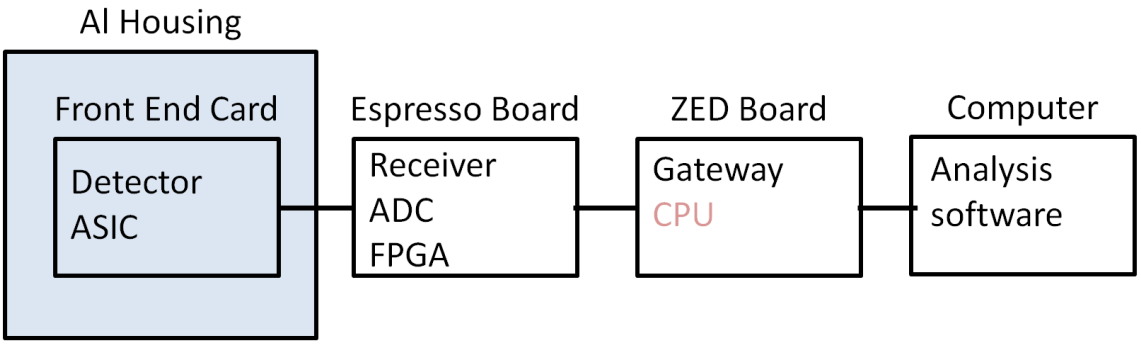

Figure 3.6: Block diagram of the 11 x 11 detector readout system. The major components of each part are listed inside the blocks. The ZED board CPU capabilities were unused.

acquisition system.

The 11 x 11 system was designed to be more portable than the 3 x 3 system (which requires an environmental chamber). Therefore, a cooling system was integrated directly into the detector housing. As described in Sec. 1.4.2, the most consistent way to achieve long-term stability with TlBr is to cool the detector to around $-20\,^{\circ}\mathrm{C}$. A two-stage peltier cooling system was used to cool the detectors. Peltiers were chosen because they are non-mechanical and do not add microphonic noise to the system. To cool the detectors, a Cu cold finger was thermally coupled to ASIC bottom plates which were thermally connected to the detectors through the three, 42-pin connectors. The other end of the cold finger was attached to a standalone peltier. The backside of the standalone pelter was thermally connected to an air-to-plate peltier unit with an attached heat sink and fan. The temperature was controlled by independently supplying power to each peltier. To optimize the cooling power, the inner peltier was set to a given voltage while the outer assembly was swept through a range of voltages. Fig. 3.7 shows the total power required by the two-stage cooling system to achieve various operating temperatures. Approximately 20 watts of power was required to cool the detector to $-18\,^{\circ}\mathrm{C}$.

Fig. 3.8a shows a block diagram of the cooling system. ABS plastic was used to support the cold finger and reduce condensation by displacing the air around the Cu.

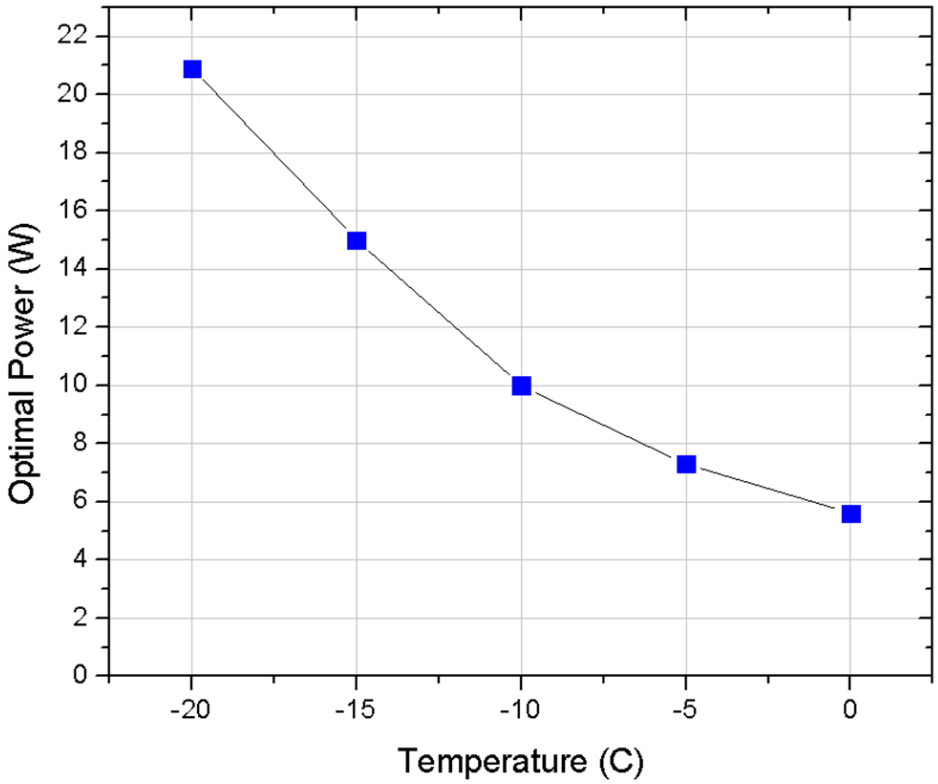

Figure 3.7: Power required to cool the detector to different operating temperatures.

To ensure maximum isolation, recesses were machined into the plastic supporting the PCB board (green board under the detector) for the underside components.

The enclosure walls were 8 mm thick. To facilitate collimation experiments, a 'window' was cut into the side nearest the detector. The 'window' wall thickness was 2 mm. Fig. 3.8b shows the enclosure side, highlighting the collimator window. An image of the entire 11 x 11 digital ASIC readout system is shown in Fig. 3.9.

3.3 Methods

3.3.1 Standard Gamma-Ray Processing

After the digitized waveforms were passed to the computer in both the 3 x 3 and 11 x 11 detectors systems, a suite of different digital filters [53] were applied depending on the application. A second software package was used to analyze the digital filter

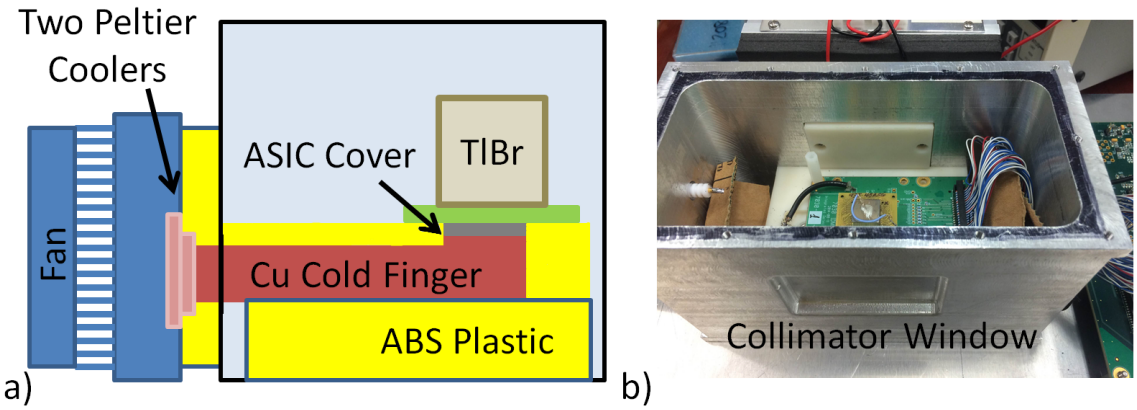

Figure 3.8: a) Block diagram of the two stage peltier cooling system. b) Side wall of the enclosure, highlighting the collimator window.

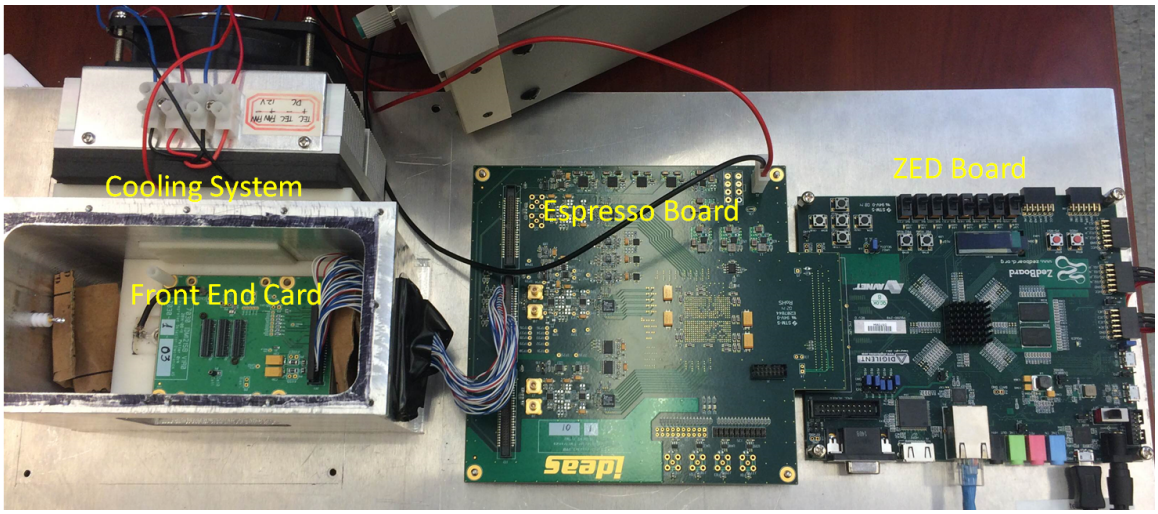

Figure 3.9: Image of the 11 x 11 digital ASIC readout system.

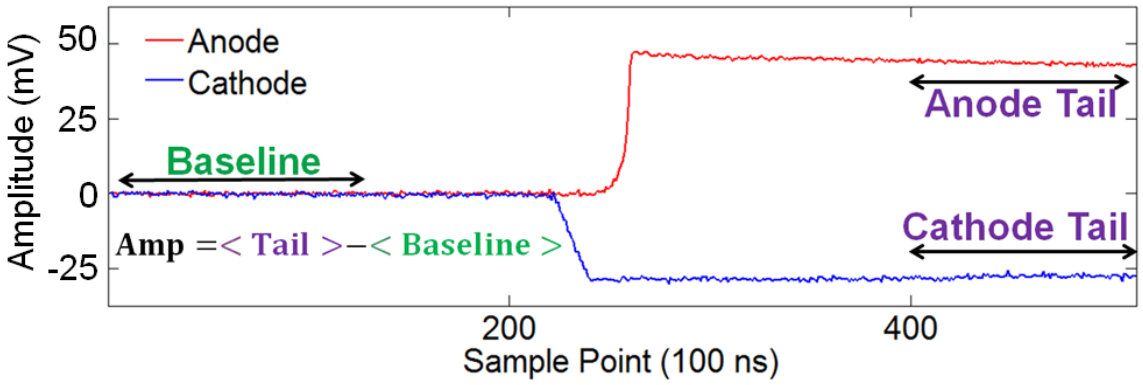

Figure 3.10: Sample waveform showing the use of simple subtraction.

output (energy and position information) [44]. Because of the small 3 x 3 detector size, data were analyzed in twenty-four hour sections for most experiments. For the 11 x 11 detectors, data were analyzed in four to six hour sections depending on the count rate.

3.3.1.1 Amplitude and Timing

For most data processed in this work, the cathode and anode amplitudes were determined using simple subtraction as shown in Fig. 3.10. One-hundred sampling points were used for the baseline and tail averages. Drift times were calculated as the difference between the anode (triggered when the electron cloud reaches the anode) and cathode (triggered when the electron cloud starts to drift) trigger times. A 1 μs CR-RC constant-fraction-timing (50%) fast shaper was used to pick-off the cathode and anode trigger times.

Gamma-ray spectra were corrected for electron trapping and weighting potential effects (both depth dependent) using the cathode-to-anode signal ratio (CAR) [6]. The CAR was also used to determine depth-dependent photopeak count rates, energy resolution, and photopeak centroids. These depth-dependent quantities were used to study material properties and isolate the degradation effects to the surface or bulk.

3.3.1.2 System Response Function Fitting

In some cases, more advanced and time-consuming System Response Function (SRF) fitting method was used to determine the amplitude and timing. SRF fitting was developed for CZT and is explained in great detail in Ref. [53]. For this processing method, a calibration system response function matrix was generated by averaging 662 keV photopeak waveforms at each depth and pixel. Simple subtraction and CAR were used to determine the amplitudes and depths to bin the waveforms for averaging. The resulting matrix expressed the expected waveforms in every pixel (P) at each depth (z):

$$WF = WF(P, z) \tag{3.1}$$

The P parameter could broken into the x-y coordinates of the pixel and the waveforms could be linearly scaled by an energy parameter (E):

$$WF = WF(x, y, z, E) \tag{3.2}$$

Once generated for a given detector, the system response function was used on any new dataset. During the fitting step, an unknown waveform pair (cathode and anode together) was compared to the system response function with various input parameters. A least squared solution was determined using the Newton-Raphson fitting method [53]. Simple subtraction and CAR were used for the initial E and z parameters. SRF fitting improves the performance compared to simple subtraction because of reduced noise through averaging.

3.3.1.3 Drift Velocity Profile

Depth-dependent electron drift velocity profiles provide unique information about internal electric fields:

$$v(z) = \mu \cdot E(z) \tag{3.3}$$

Previously, the cathode surfaces were exposed to alpha particles to determine the drift velocity profile via the differential cathode signals [32, 46]. Using alpha particles is cumbersome and requires increased dynamic range during acquisition because of the large energy depositions: typically 5.5 MeV alpha particles from ^{241}Am are used. A high dynamic range sacrifices the fidelity of lower energy gamma rays (E$\sim$1 MeV). Additionally, distinguishing alpha particles from gamma rays can be difficult due to shielding and geometric constraints. Even a thin layer of glue or epoxy can decrease the alpha particle energy to less than 1 MeV.

Using a similar differential method, depth-dependent drift velocity profiles were calculated using cathode-side photopeak events from 662 keV gamma rays. These events were selected by windowing on the high energy region of the cathode spectrum, as shown in Fig. 3.11a. The cathode signal amplitude is proportional to the deposited energy and the interaction depth (see Sec. 2.1). Therefore, photopeak events (largest energy) interacting at the cathode surface (largest weighting potential change) will have the largest cathode amplitude. Once cathode-side photopeak events were isolated, the waveforms were normalized to account for any amplitude differences. Typical energy resolutions ranged from 1 to 3% FWHM at 662 keV, therefore, photopeak events did not have the exact same amplitude. Because of the linear cathode weighting potential, a change in cathode amplitude is proportional to a change in depth. Thus, the depth-dependent drift velocity was calculated by dividing the change in cathode signal amplitude by the change in time for each of twenty or forty cathode-signal depth bins (see Fig. 3.11b-c).

Some TlBr detectors showed relatively high hole mobility and full hole collection was observed for photopeak interactions in the center of the detector. Fig. 3.12 shows a center event for a typical detector with high hole mobility. The first slope, 22 μs $<$ t $<$ 26 μs, was caused by the drift of both electrons and holes. The second slope, 26 μs $<$ t $<$ 42 μs, was caused by the drift of only holes. The electrons were

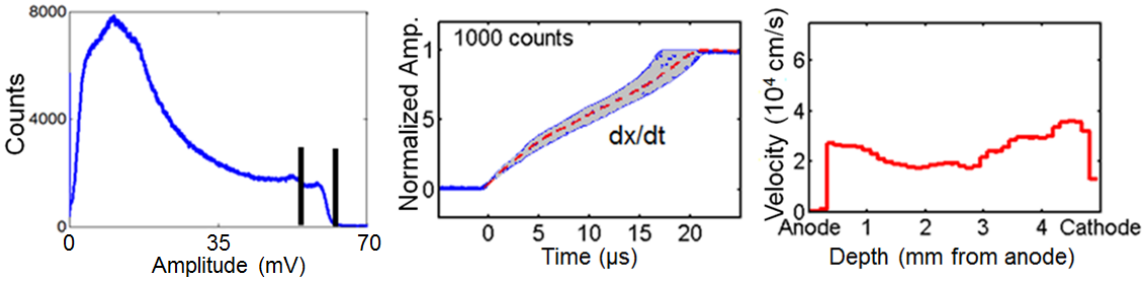

Figure 3.11: a) Cathode spectrum and window isolating cathode-side photopeak events. b) The normalized average cathode waveform of windowed events is shown as the dashed trace. c) The calculated electron drift velocity profile.

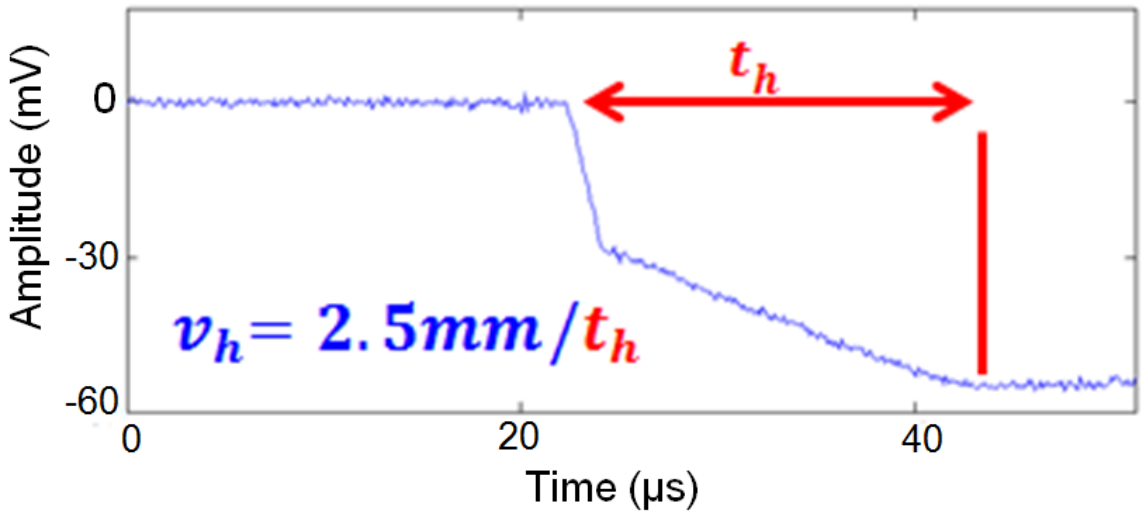

Figure 3.12: Sample waveform from a center event used to calculate the hole drift time for high hole mobility detectors.

fully collected at $t = 26$ μs due to a faster drift velocity, resulting in the observed kink in the waveform. The hole drift velocity was estimated by isolating center events, $0.48 < \text{CAR} < 0.52$, and dividing half the detector thickness (2.5 mm) by the hole drift time. Unlike with the electron drift velocity, this method only estimates an average value instead of a depth-dependent profile.

3.3.2 Accounting for the Motion of Holes

The CAR method to determine the interaction depth assumes that holes do not contribute to the cathode amplitude, either because they are trapped or because they

do not drift a significant length during the collection time. Some TlBr detectors show significant hole contributions to the cathode signal, resulting in poor depth reconstruction [32, 37]. A method was developed to account for hole motion and remove their contribution to cathode signals to properly reconstruct interaction depths using the CAR. Different approaches were required for detectors with different degrees of hole contributions.

As described in Sec. 3.2.2, a collimator was used to test the accuracy and precision of the different reconstruction algorithms. In order to know the true depth from the collimator position, the absolute cathode surface location was determined by sweeping the collimator through different positions around the cathode surface and recording photopeak count rates at each position, as shown in Fig. 3.13a. When no part of the gamma-ray beam was incident on the detector, only background counts were recorded (distance less than 1 mm in Fig. 3.13a). When the whole beam was incident on the detector, a maximum count rate was observed (distance greater than 2 mm on Fig. 3.13a). The cathode surface was set to 1.30 mm, corresponding to the midpoint rise in photopeak counts. All depths were then referenced from this cathode surface.

The depth resolution, or precision, of each reconstruction algorithm was calculated by fitting the count distribution of a single collimator position as shown in Fig. 3.13b. The Gaussian fit FWHM was used as the depth resolution.

3.3.2.1 Low Hole Mobility Detectors

The red trace in Fig. 3.14 shows the raw cathode signal from a detector with low, but significant, hole mobility. The first slope, 22 μs $<$ t $<$ 24 μs, was dominated by electron drift and the second slope, 24 μs $<$ t $<$ 50 μs, was caused by hole drift only. In order to use the CAR, hole components must be removed. To remove hole components, a fast shaper, shown in the blue trace of Fig. 3.14, was applied to raw waveforms. The shaped signal maximum corresponds to the electron collection

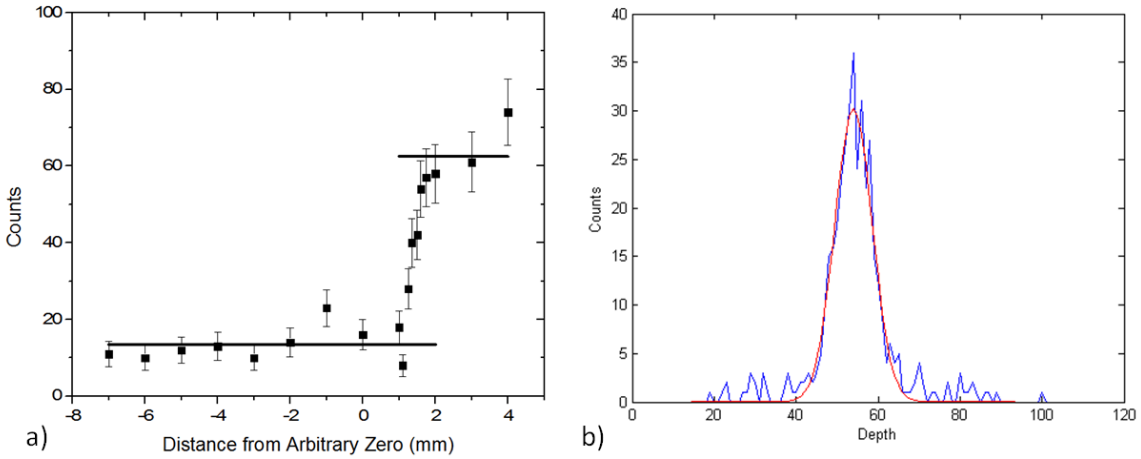

Figure 3.13: a) Detected counts when the collimator was swept across the cathode surface used to determine the absolute location of the cathode. b) Example count distribution for a single collimator position. The peak was fit with a Gaussian to determine the depth resolution.

time, in this case about t = 24 μs. A linear fit was applied to the hole component, 24 μs < t < 50 μs, which was then subtracted from the waveform. The result was the electron-only component of the waveform, shown in the black trace of Fig. 3.14, which is required for the CAR.

3.3.2.2 High Hole Mobility Detectors

For some TlBr detectors, μ_h/μ_e can be as large as 0.15 [54] and holes are fully collected in the sampling window, as shown in the red trace of Fig. 3.15. The hole mobility was measured from the drift time of center-of-detector events. Therefore, $\mu_h = D^2/2t_hV$, where D is the detector thickness, V is the applied bias, and t_h is the hole drift time from the center of the detector. In contrast, the electron mobility was measured from cathode-side events, therefore, $\mu_e = D^2/t_eV$. For cathode waveforms with full hole collection, a two part fit was used. The same fast shaper used in Fig. 3.14 was applied to determine the electron collection time, which was roughly 25 μs for the sample waveform shown in Fig. 3.15. A second fast shaper was applied to determine the hole collection time, roughly 35 μs, by filtering the second half of

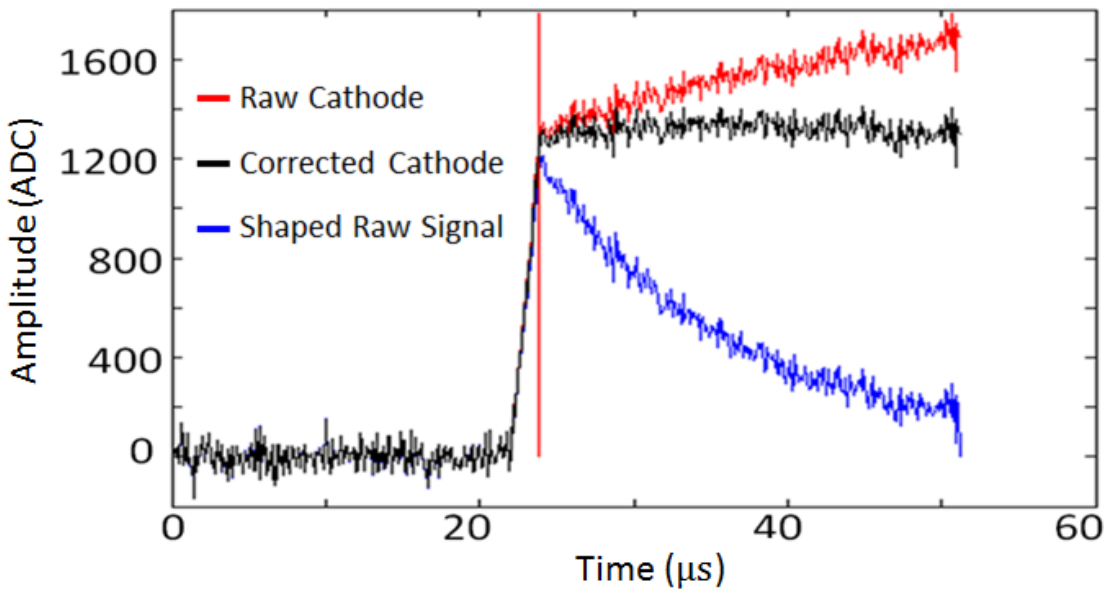

Figure 3.14: Raw cathode signal (red) showing the motion of holes (second slope in the waveform), electron only component (black) and shaped raw signal (blue).

the waveform (t $>$ 25 μs). The waveform was fit with a two-part piecewise linear function which was subtracted from the raw waveform. The resulting signal, shown in the black trace of Fig. 3.15, was the electron-only component used for the CAR.

The two part linear fit reconstructed the depth of interaction for most of the bulk. The algorithm failed for events near the cathode because the hole collection time was too close to the electron collection time, causing the second fast shaper to not peak at the hole collection time. Fig. 3.16 shows a cathode waveform for a near cathode-side event. The second slope-change, corresponding to the hole collection time, was not found, and no correction was applied. Therefore, the raw signal is identical to the corrected signal in the figure. A Newton-Raphson (NR) fitting method was used to overcome this issue.

An analytic expression was derived for the cathode preamplifier output signal shown in Fig. 3.17, given a linear weighting potential and constant electric field. The

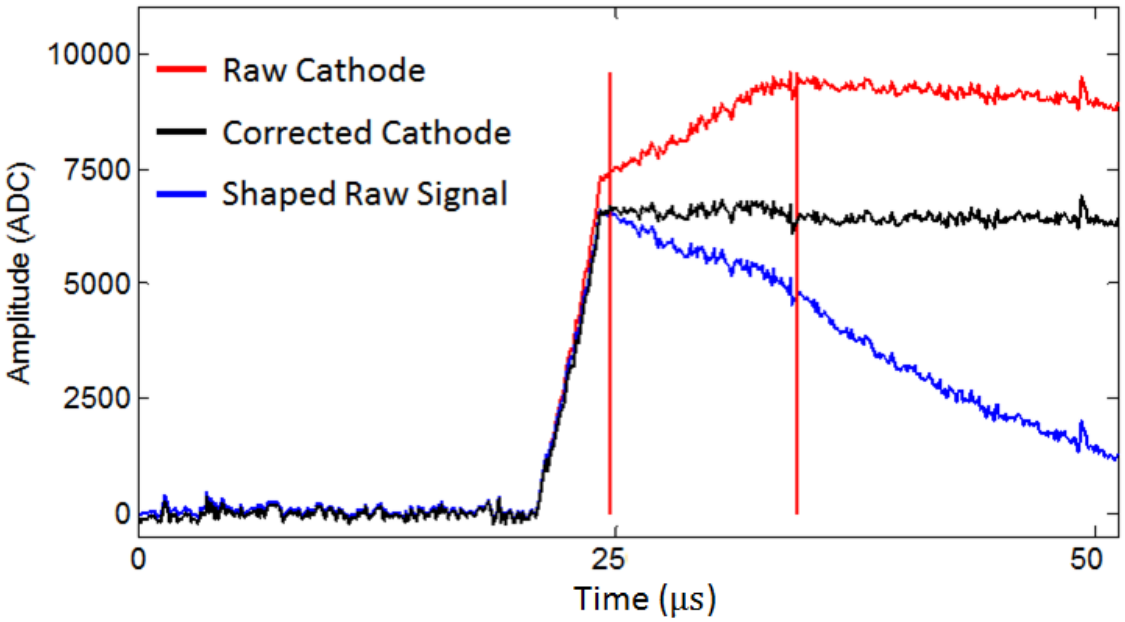

Figure 3.15: Raw cathode signal (red) showing the motion of holes which are eventually fully collected, electron only component (black) and shaped raw signal (blue).

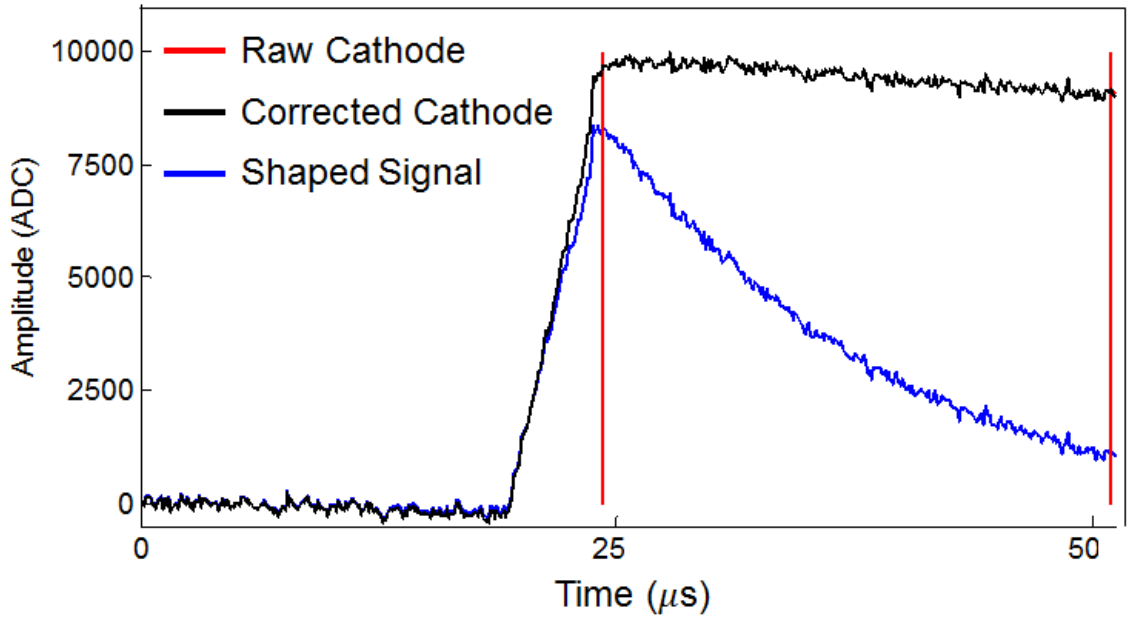

Figure 3.16: When the second slope-change point to too close to the first slope-change point, the two-part fitting algorithm fails.

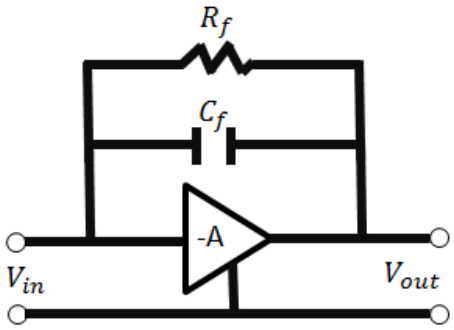

Figure 3.17: Simplified schematic for an eV-Products preamplifier.

electron contribution to the output signal is given by:

$$V_{e.c}(t) = -\frac{V_e RC}{t_e}\left(1 - e^{-t/RC}\right) \;\; for\; t < t_e$$

$$V_{e.c}(t) = -\frac{V_e RC}{t_e}\left(1 - e^{-t_e/RC}\right) e^{(t-t_e)/RC} \;\; for\; t > t_e$$

where $V_{e.c}(t)$ is the electron component to the total voltage, V_e is the maximum possible electron voltage, RC is the time constant of the preamplifier feedback circuit, and t_e is the electron collection time. A similar expression was derived for holes and the two were added together to obtain a forward model for the expected cathode waveform:

$$V(t) = V_{e.c.}(t) + V_{h.c.}(t)$$

$$V(t) = F(V_e, V_h, t_e, t_h, t) \tag{3.4}$$

The NR algorithm was applied to cathode waveforms by varying parameters in Eq. 3.4 to find the optimum, least-squares, values. The initial parameters for the NR algorithm were determined from the two-part fit method. An algorithm flow diagram is shown in Fig. 3.18.

Fig. 3.19 shows the NR algorithm applied to the same cathode waveform shown in Fig. 3.16. Unlike with the two-part linear fit, the hole component was captured. The least-squares electron component, $V_e = 9,069$ ADC, was then used in the CAR

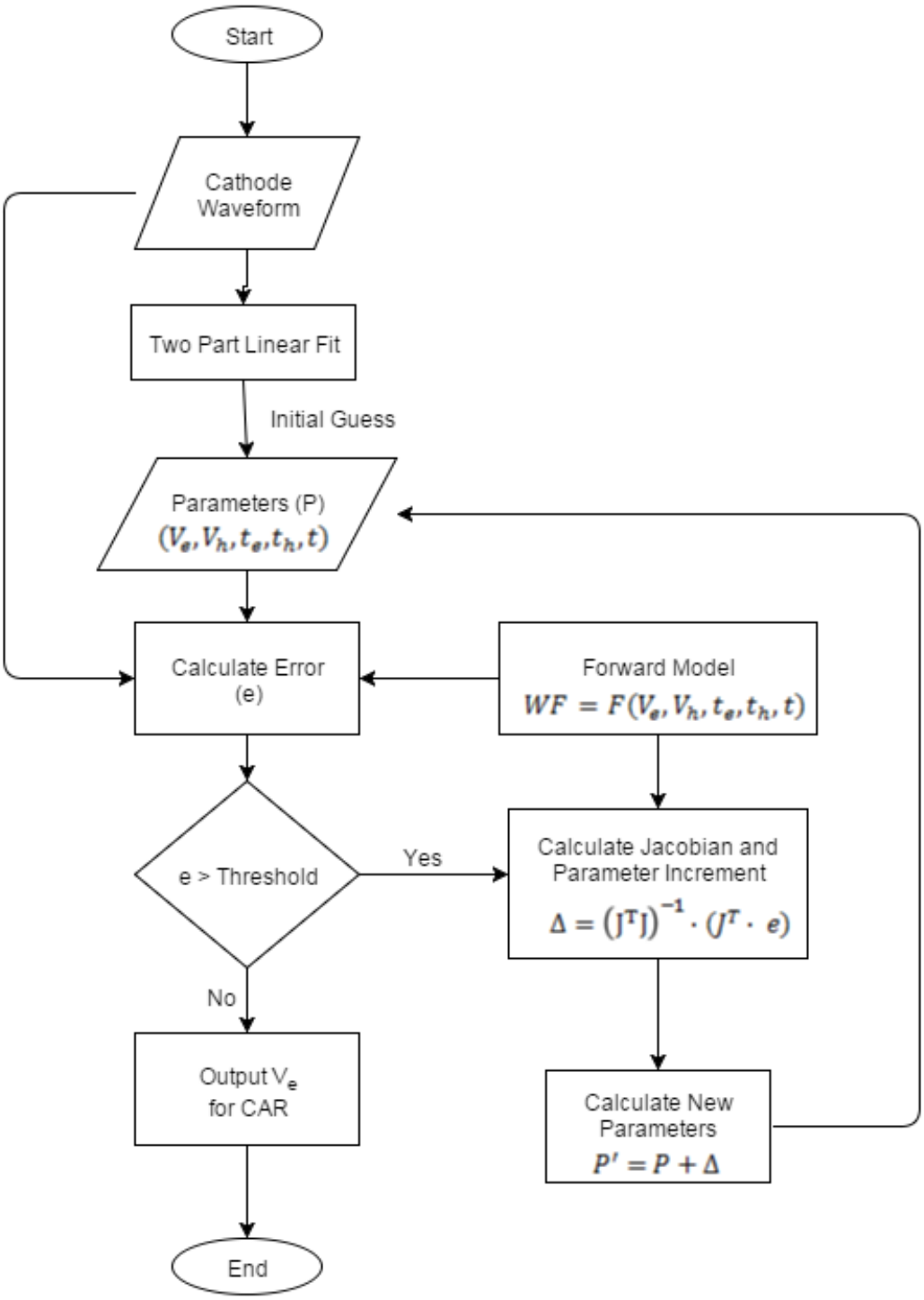

Figure 3.18: Flow diagram for the NR fitting algorithm.

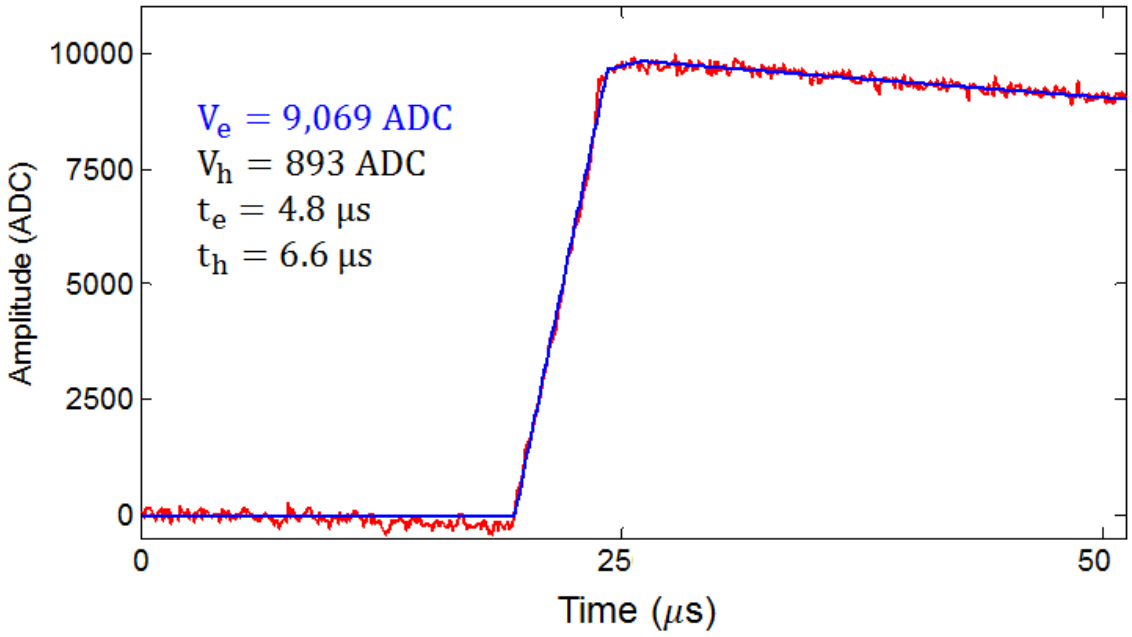

Figure 3.19: Application of the Newton-Raphson algorithm on the waveform shown in Fig. 3.16.

to calculate the interaction depth. The hole component for the event shown in Fig. 3.19 was $V_h = 893$ ADC, which was approximately 10% of the electron component. Therefore, capturing the hole component, which was not done with the two part fit, was critical for proper depth reconstruction.

The NR method achieved good depth reconstruction for all depths except right at the cathode surface (see Sec. 5.2.2). For depths near the cathode, hole collection times were less than electron collection times and there were no unique solutions to the least squares problem. Fig. 3.20 shows two forward model waveforms with the following parameters:

$$V(t) = F(10k\ ADC,\ 1k\ ADC,\ 5\mu s,\ 4.5\ \mu s,\ t)\ (red)$$

and

$$V(t) = F(11k\ ADC,\ 0,\ 5\mu s,\ 0,\ t)\ (blue)$$

The two waveforms are offset in time because they are otherwise indistinguishable. The NR algorithm fails when $t_h < t_e$, and the waveforms are degenerate.

A hybrid NR-Timing (NRT) method was developed to account for degenerate waveforms at the cathode surface. First, a mobility ratio $m = \mu_h/\mu_e$ was calculated using center-of-detector events with full hole collection for the hole mobility and cathode-side events for the electron mobility. Next, a timing spectrum was calculated for all events between the cathode side, $z = C$, and $z = C(1-m)$. The two-part slope method was used to determine the depth for this step because when the two-part slope method fails, the depth is overestimated, pushing the count closer to the cathode. Therefore, events within $C(1-m) < z < C$ will never be pushed to $z < C(1-m)$. Finally, the data were processed again and events within $C(1-m) < z < C$ were reconstructed using timing while events with $z < C(1-m)$ were reconstructed using the NR method. Timing was used in previous works to reconstruct all depths [32]. However, due to increased noise, depth resolution was poor compared to the NRT method (Sec. 5.2.2).

Accounting for hole motion to correct the CAR was only required for single-pixel events. Interaction depths for multiple-pixel events were calculated using timing, which is unaffected by hole motion. However, because timing for multiple-pixel events was correlated to interaction depth through a calibration from single-pixel events, improving interaction depths of single-pixel events will improve depth reconstruction for all events.

3.3.3 Leakage Current and LED Stimulation

The leakage current through a detector is a measurement of background concentrations of free charge carriers in the conduction band of a semiconductor. Concentration are dependent on temperature, number of trapped electrons, and any external stimulation source like an LED. A high voltage supply with an ammeter was used to

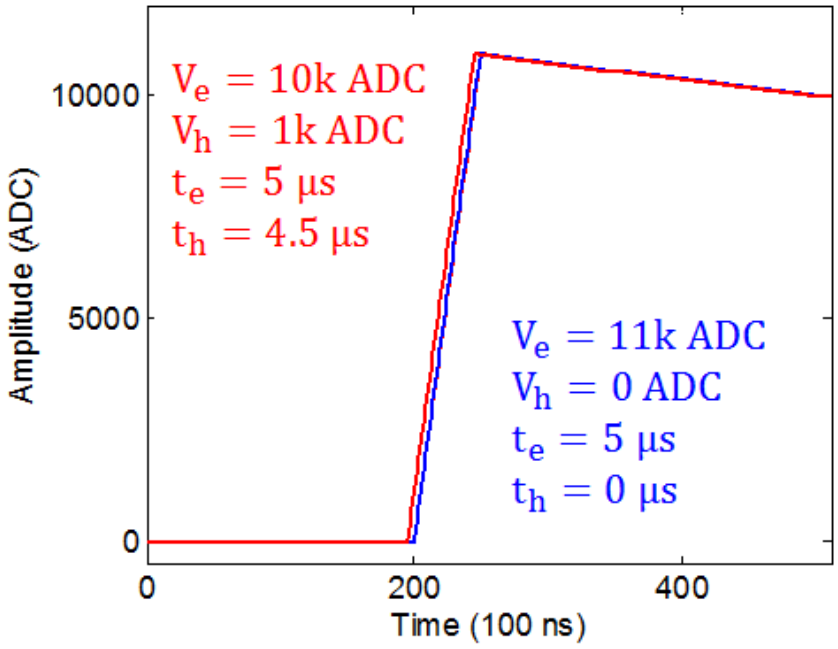

Figure 3.20: Degenerate waveforms exist near the cathode surface where the hole collection time is less than the electron collection time.

measure overall leakage currents through the detectors. This current was a combination of direct leakage from the cathode, through the bulk, to the anode, and any surface leakage. In order to study bulk material properties, leakage currents were measured on the pixels, which because of the guard ring, contained no contribution from surface leakage. Feedback resistor DC offsets were used to measure leakage currents through the pixels.

From the simplified schematic in Fig. 3.17, leakage currents were calculated for each pixel by measuring the DC offset of each preamplifier. Bulk detector leakage current must pass through the feedback resistor, the only DC path. From Ohm's Law, $I_{leak} = V_{DC}/R_f$, where I_{leak} is the leakage current, V_{DC} is the preamplifier output DC offset, and R_f is the feedback resistor value. The cathode preamplifier was AC coupled to the cathode electrode, therefore this method only worked on the pixelated anodes. Leakage currents were used to monitor steady-state concentrations as well as stimulated responses from an LED to calculate freed electron concentrations.

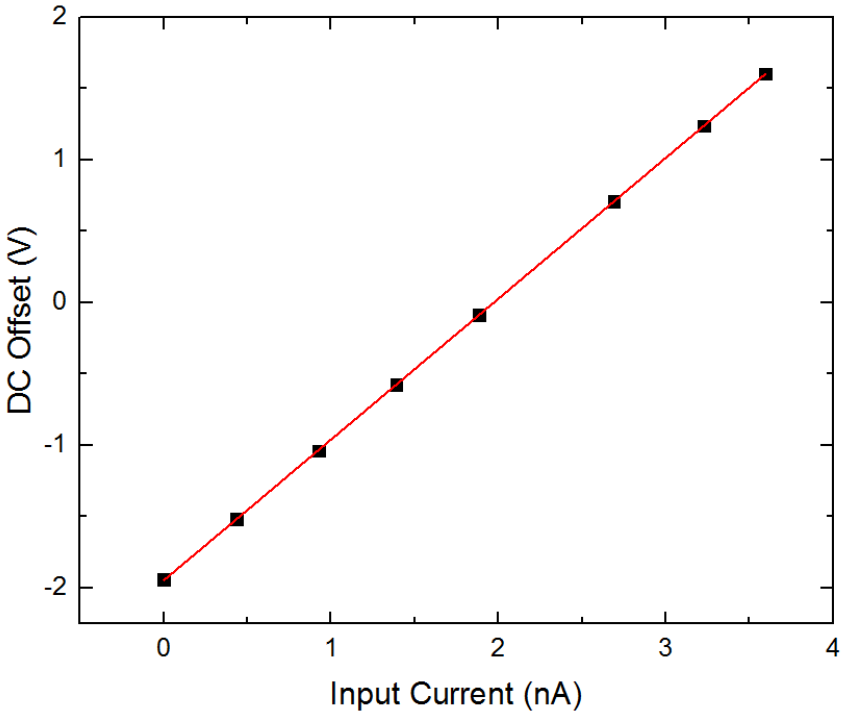

Figure 3.21: DC offset as a function of input current for the Channel 1 preamplifier. The slope of the best fit line is the feedback resistance.

The feedback resistor value was measured directly by connecting a 200 MΩ resistor in series with the preamplifier inputs. A variable voltage on the order of 1 V was used to generate nanoamps of current, while preamplifier outputs were connected to an oscilloscope where DC offsets were monitored. Fig. 3.21 shows the preamplifier response to various input currents. The feedback resistance is the slope of the best-fit line. I-V characteristics of all ten channels were measured and the average feedback resistor value was (9.71 ± 0.22) x 10^8 Ω. The average value was used for all leakage current calculations.

Freed electron concentrations were estimated by measuring leakage current change through pixel preamplifiers after the samples were illuminated with a Cree, Inc. 2.1 eV (sub-bandgap) through-hole LED. When the LED was turned on, sub-bandgap photons excited trapped electrons into the conduction band, increasing leakage current. Fig. 3.22 shows the pixel-by-pixel response of a TlBr detector to different LED in-

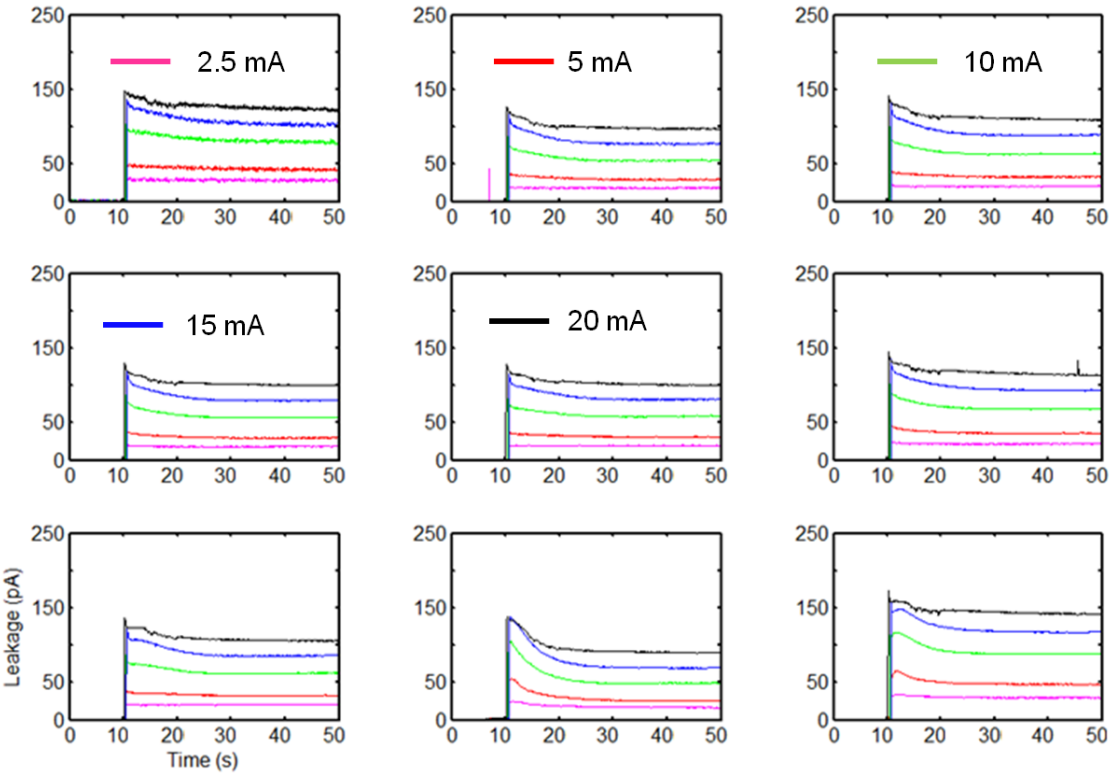

Figure 3.22: Pixel-by-pixel response to different LED intensities. The current through the LED is proportional to the emitted photon flux.

tensities. The LED was turned on after 10 s and an equilibrium current was reached after 20 s. In general, there was good linearity between the impulse current and LED current for LED currents less than 10 mA. Non-linearity occurred when the number of freed electrons was saturated. All measurements were done with LED currents less than 10 mA to maintain linearity.

The impulse current in each pixel as a result of LED photons is given by Eq. 3.5:

$$\Delta I = \Delta n v_e q A \tag{3.5}$$

where Δn is the increase corresponding to the concentration of detrapped electrons, v_e is the electron drift velocity, q is the electron charge, and A is the pixel pad area. Rearranging Eq. 3.5 results in an expression for the freed electron concentration as

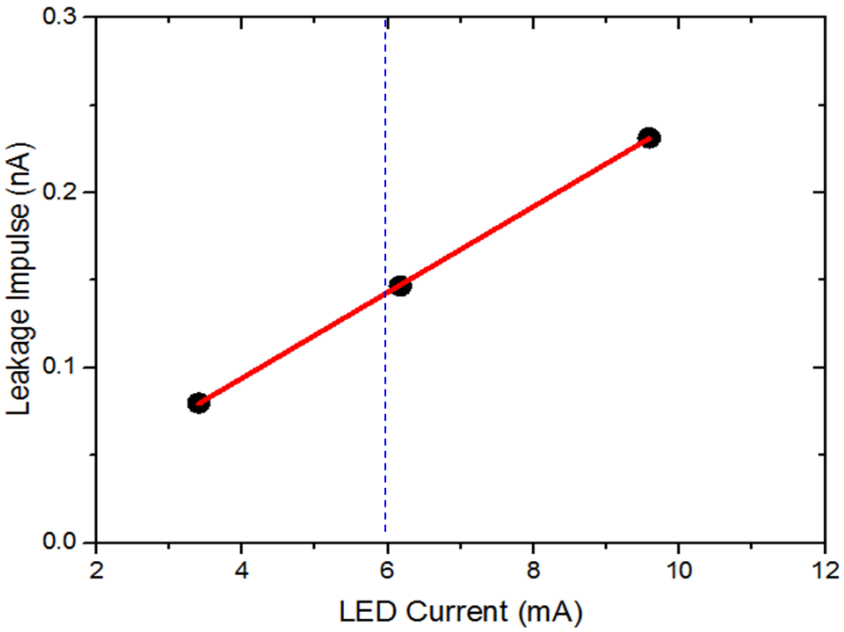

Figure 3.23: To calculate the leakage current impulse at exactly 6 mA, the impulse was measured at three LED currents and the linear best fit line was used to calculate the expected impulse at 6 mA.

a result of LED illumination:

$$\Delta n = \Delta I / v_e q A. \tag{3.6}$$

For detectors with low $\mu_h \tau_h$ compared to $\mu_e \tau_e$, hole drift velocities are negligible compared to electron drift velocities and currents are dominated by freed electrons. Therefore, this method was only used on detectors with low hole mobility.

During a typical LED experiment, the LED was used to illuminate detectors prior to each twenty-four-hour data acquisition and the impulse current, ΔI, was measured in each pixel. To ensure the same LED current (i.e. photon flux) was used for each experiment, impulses were measured for three LED currents, ∼3 mA, ∼6 mA, and ∼9 mA, and a linear best-fit line was used to determine the expected impulse at exactly 6 mA as shown in Fig. 3.23. This was done because it was difficult to accurately control the LED current. Uncertainty in the calculated impulse at 6 mA, derived from uncertainties in linear fit parameters, was propagated to freed electron concentration uncertainties.

In Sec. 5.3, drift velocities, indirect measures of the electric field, are correlated to freed electron concentrations. Waveforms from the first hour following LED stimulation were used to estimate these electron drift velocities using techniques described in Sec. 3.3.1.3. The LED was turned off during gamma ray data acquisition. Previous work has used light stimulation to remove space charge from TlBr [55] and even measure electron concentrations of solar cell semiconductor materials [56, 57]. The novelty of this approach, was that the same experimental setup (no change in bias, temperature, electrode configuration, etc.) was used to simultaneously measure freed electron concentrations and detector performance characteristics such as energy resolution and electric field profiles. This allowed for easy correlations between material properties and detector performance.

3.3.4 Mobility-Lifetime Characterization

The mobility-lifetime product ($\mu\tau$) is used to characterize the performance of semiconductor radiation detectors and determine the viability of new materials for gamma-ray spectroscopy and imaging. The traditional method to calculate electron mobility-lifetime product ($\mu_e\tau_e$) uses the Hecht relation:

$$Q = N_0 e_0 \frac{\mu_e \tau_e V}{D^2}\left[1 - exp\left(-\frac{D^2}{\mu_e \tau_e V}\right)\right] \tag{3.7}$$

where Q is the induced charge on the cathode or anode, N_0 is the number of electrons generated by the radiation interaction, e_0 is the electron charge, V is the applied bias, and D is the detector thickness [58]. Eq. 3.7 assumes a uniform electric field, uniform $\mu_e\tau_e$, and that interactions take place at the cathode surface. During the measurement, alpha-particles or low energy x-rays are used to generate electrons near the cathode surface. Holes are immediately collected and the resulting signal is caused by only the electron drift. The photopeak amplitude, assumed to be proportional to

Q which is true only if ballistic deficit is insignificant, is measured as a function of bias, and the result is fit with Eq. 3.7 to extract $\mu_e\tau_e$. By switching the bias polarity, $\mu_h\tau_h$ can be measured using the same technique.

Mobility-lifetime products based on Hecht fitting have been shown to underestimate true $\mu\tau$ due to ballistic deficit and surface trapping [59, 60]. Specifically, the method assumes that surface trapping is minimal and that shaping times are much longer than electron drift times. Additionally, curve fitting is required. Work by Jones *et al.* showed that measured $\mu_e\tau_e$ can vary by up to 30% when the same data are fit with the Hecht relation by different researchers because of subjective fitting constants [60]. Additionally, the authors showed $\mu_e\tau_e$ variations up to a factor of 5 when they used Hecht fitting and different shaping times, particle types, and particle energies on the same detector.

A more direct $\mu_e\tau_e$ measurement for single polarity charge sensing detectors was developed to overcome many of the issues resulting from Hecht fitting [59]. Single polarity charge sensing detectors utilize electrode geometry (e.g. coplanar grids [5], pixels [6], Frisch collar devices [61, 62]) to measure the drift of only one charge carrier type. The technique is particularly useful for materials like CdZnTe, HgI_2, and TlBr, where electron mobilities are significantly greater than hole mobilities.

The two-bias method outlined in Ref. [59] uses the measurement of cathode-side charge collection efficiency at two different biases to measure the $\mu_e\tau_e$:

$$\mu_e\tau_e = \frac{D^2}{\ln\left(N_1/N_2\right)}\left(\frac{1}{V_2} - \frac{1}{V_1}\right) \tag{3.8}$$

where N_1 and N_2 are the photopeak centroids at biases V_1 and V_2, respectively. Assuming uniform bulk trapping,

$$N_1(z) = N_0 \exp\left(-\frac{zD}{\mu_e\tau_e V_1}\right) \tag{3.9}$$

where N_0 is the number of generated electron-hole pairs.

While the two-bias method only requires that N_1 and N_2 be from the same depth, cathode side events are generally chosen because they are easiest to select, have lowest uncertainty, and ensure that the measured $\mu_e\tau_e$ is averaged over the entire bulk. Cathode-side events are typically selected using the cathode-to-anode signal amplitude ratio (CAR) [6]. Because interaction depths can be determined, high energy gamma rays can be used, reducing signal-to-noise ratios and improving results. The two-bias method is not as sensitive to ballistic deficit because rise times in single-polarity configurations are much shorter than electron drift times. Additionally, unlike with Hecht fitting, low fields are not required. The two-bias method is also not sensitive to surface trapping or uncertainty in particle penetration depth because the interaction depth is accurately determined by the CAR: note the CAR will ignore any bulk with heavy surface trapping. Additionally, due to the ratio of the N_1 and N_2 signals, the two-bias method is not sensitive to many systematic effects like non-uniform charge collection and depth-dependent performance variation. Specific descriptions of these improvements are detailed in Ref. [59].

The standard two-bias method assumes a uniform electric field; however, unlike with Hecht fitting, electric filed non-uniformity effects can be corrected as shown in Sec. 4.2.3. It should be noted that the two-bias method assumes electron drift speeds are only determined by applied bias and mobility, and ignores diffusion and inter-cloud repulsion. This condition is achievable with realistic electric field strengths above 1000 V/cm.

The two-bias method was used in this work to calculate the mobility-lifetime products. However, a modification was developed because the original two-bias method assumes an ideal weighting potential for single-polarity charge sensing. Specifically, zero weighting potential throughout the bulk and a rapid increase to one at the anode surface. Sec. 4.2 shows that when the two-bias method is applied to pixelated

detectors, the true $\mu_e\tau_e$ is systematically overestimated by up to 20% for common detector thicknesses and electrode geometries. As a result, a simple correction factor is required:

$$\mu_e\tau_e = k(\mu_e\tau_e)_{TwoBias} \tag{3.10}$$

where $(\mu_e\tau_e)_{TwoBias}$ is the electron mobility-lifetime product calculated from Eq. 3.8 using a pixelated detector.

The two-bias method was furthered expanded in this work by using Eq. 3.8 to calculate $\mu_e\tau_e$ as a function of depth. This was accomplished by noting that if non-cathode side events are used, $D = z$. Therefore Eq. 3.8 becomes:

$$\mu_e\tau_e(z) = \frac{zD}{\ln\left(N_1/N_2\right)}\left(\frac{1}{V_2} - \frac{1}{V_1}\right) \tag{3.11}$$

It is important to note that the $\mu_e\tau_e$ calculated at a specific depth $z = z_i$ is the average $\mu_e\tau_e$ from $0 < z < z_i$. $\mu_e\tau_e$ profiles were used to map trapping non-uniformity throughout the crystal bulk along the depth dimension.

3.3.5 Using the Tl Characteristic X-Ray

After a photoelectric event, the absorber atom is left in an excited state. The resulting decay releases a characteristic x-ray whose energy tends to be larger for high-Z materials. Tl has four probable characteristic x-rays at 70.8 keV, 72.9 keV, 82.6 keV, and 85.9 keV. The Tl x-ray mean free paths are on the order of 0.5 mm (1/2 the pixel pitch), therefore, it is probable that x-rays will escape the pixel where the photoelectric event occurred. If the trigger threshold is greater than 80 keV or the event occurs on an outer pixel with the x-ray traveling out of the detector, the x-ray energy will be lost and an x-ray escape peak will be observed below the photopeak. If thresholds are set below 70 keV and the event occurs on an inner pixel, the x-ray energy can be captured by a neighbor pixel, assuming the interaction does

not occur near the anode. Therefore, a two-pixel event where one of the energy depositions equals the characteristic x-ray energy, is a unique signature of photoelectic interactions. Identifying photoelectric interactions can improve isotope identification, event reconstruction, and multiple pixel energy resolutions. This work explores using characteristic x-rays to improve isotope identification and multiple pixel energy resolution.

An ideal spectrum for isotope identification is a photopeak at the gamma-ray energy with no Compton continuum. In an attempt to create an ideal spectrum, two pixel events from a single ^{137}Cs source and a mixed ^{137}Cs and ^{60}C0 source were binned only if one events was at the Tl characteristic x-ray energy. This filtered spectrum was compared to the one- and two-pixel spectra from the same dataset (see Sec. 7.2.1).

The relative energy resolution of a TlBr detector is given by:

$$R = \frac{2.35\sqrt{E}}{E} \tag{3.12}$$

where E is the energy deposited in the detector. The $\sqrt{E}$ in the numerator results from the Poisson nature of the charge carrier generation: a monoenergetic deposition will create $N \pm \sqrt{N}$ charge carriers. However, if the exact energy (no uncertainty) of a portion of the deposited energy is known, that deposition does not contribute to the overall energy uncertainty. To improve energy resolutions, multiple-pixel events where one deposition was close to an x-ray energy was filtered and the measured energy was changed to the exact x-ray energy. For example, if the two measured energies of a two-pixel event were $E_1 = 592.3$ keV and $E_2 = 72.3$ keV, E_2 would be changed to the true x-ray energy of $E_2 = 72.9$ keV and the event would be processed using the new energy. Using this method, the theoretical energy resolution improves to:

$$R = \frac{2.35\sqrt{E - E_{Tl}}}{E} \tag{3.13}$$

where E_{Tl} is the Tl characteristic x-ray energy. This method was applied to 11 x 11 detectors and the x-ray filtered spectrum was compared to an unfiltered spectrum (see Sec. 7.2.2).

CHAPTER IV

Simulations: Optimizing Pixel Pitch and Calculating a Correction Factor to the Two-Bias Method

Simulations were used in this work for two distinct purposes: 1) Optimize the pixel-pitch to decrease single-pixel double interaction and charge sharing event rates and increase x-ray identification rates, and 2) calculate a correction factor for the two-bias method. Geant4, a Monte Carlo particle tracker, was used for purpose one and Maxwell, a discrete voxel, analytic, electromagnetic field simulator, was used for purpose two.

4.1 Energy Deposition in TlBr

When photons deposit energy into TlBr detectors, the generated photoelectrons create electron clouds with non-uniform charge density.The Tl characteristic x-rays or bremsstrahlung radiation can create additional clouds that overlap the original cloud. Knowledge of the electron cloud density and whether two clouds overlap is important for designing the optimum anode configuration (pixel to pixel-pad ratio) and predicting expected x-ray identification rates (likelihood that a event with energy close to the characteristic x-ray energy, is from a characteristic x-ray event). A Geant4 model

[63] was used to simulate gamma-ray interactions in TlBr to calculate electron cloud sizes and x-ray identification rates. These values were compared to CZT, currently the most advanced room-temperature semiconductor detector material. Experimental data were used to validate the models.

4.1.1 Geant4 Model

A Geant4 model was developed for CZT and modified for TlBr [53]. The model consisted of a 20 x 20 x 15 mm^3 pixelated detector for the electron cloud simulations (to compare to standard CZT designs), and an 11 x 11 x 5 mm^3 pixelated detector for x-ray identification simulations. For most simulations, a ^{137}Cs source was modeled 10 cm from the cathode surface, resulting in a near parallel beam of gamma rays as shown in Fig. 4.1a. For both sets of simulations, all primary (e.g. incident gamma rays), secondary (e.g. generated photoelectrons) and tertiary (e.g. characteristic x-rays and bremsstrahlung radiation) energy depositions and interaction locations were tracked. The electron energy threshold was set to 3 keV, corresponding to an electron cloud size precision of less than 1 μm, the mean free path of a 3 keV electron. The gamma-ray threshold was set to 1 keV to include all characteristic x-rays and bremsstrahlung radiation.

List mode data were output for every interaction and contained the following information: 1) particle type, 2) interaction type 3) energy deposition and 4) interaction position. The electron cloud size was calculated as the furthest distance between any two electron energy depositions from the same photon. Due to their mean free path, characteristic x-rays were considered a different photon while bremsstrahlung were not. Fig. 4.1b shows a schematic of an interaction tracked by the simulation. In the example, an incident gamma ray Compton scatters then undergoes photoelectric absorption. The first interaction creates a bremsstrahlung photon which increases the electron cloud size.

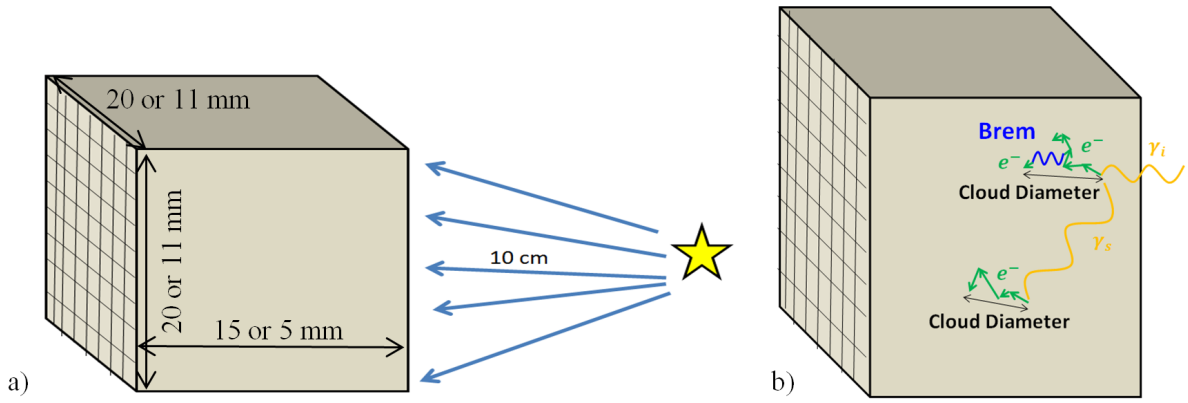

Figure 4.1: a) Schematic of the Geant4 setup. Both TlBr and CZT detectors were modeled for comparison. b) Schematic of a theoretical Compton scattering event.

The simulated energy recorded by each pixel was determined by how much electron cloud overlapped each pixel. This was calculated from the energy density of each cloud. The true event rates (one-pixel, two-pixel, etc. from experimental data) were compared to simulated detector outputs for different event types.

4.1.2 Optimum Pixel Pitch

Fig. 4.2a shows the electron cloud size distribution from 662 keV photoelectric interactions in both CZT and TlBr. Table 4.1 lists the parameters describing each distribution. As expected, the peak of the electron cloud distribution was smaller in TlBr compared to CZT because high-energy photoelectrons created by gamma ray interactions were stopped more quickly in the higher density TlBr. However, due to the higher atomic number, the high diameter tail is more significant in TlBr because the bremsstrahlung spectrum has a higher energy and flux (see Fig. 4.2b). Bremsstrahlung radiation will travel further than the photoelectron, artificially increasing the cloud size for some TlBr events, particularly, those events with high energy bremsstrahlung x-rays. The shape of the distributions, especially in the high energy tail region, influences the different event rates.

For pixelated detectors, the fraction of single-pixel double-interaction (SPDI) and

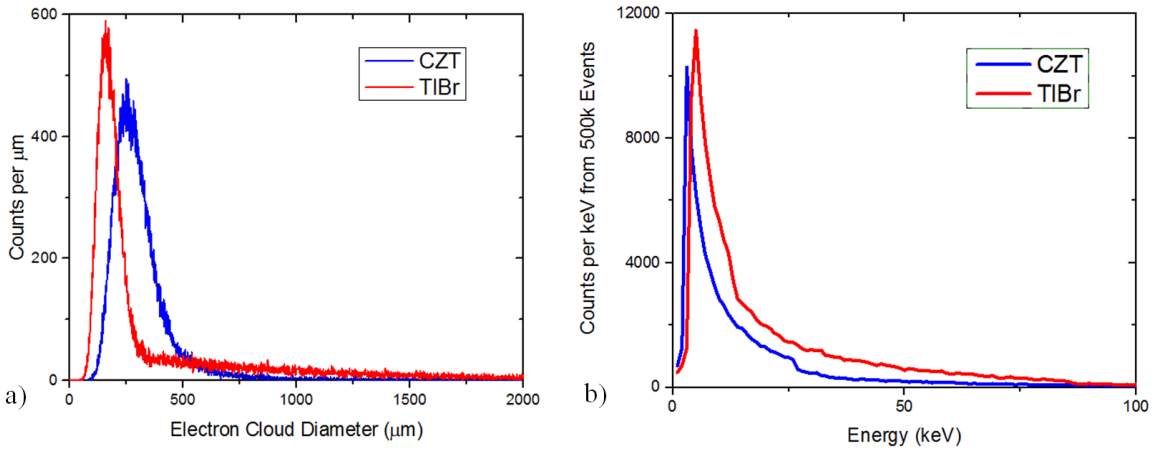

Figure 4.2: a) Cloud size distribution and b) bremsstrahlung spectrum for TlBr and CZT detectors from 500k events.

Table 4.1: Parameters describing the distributions shown in Fig. 4.2a.

Material	Mean (μm)	Median (μm)	Centroid (μm)	Fraction Above 500 μm
TlBr	469	202	160	0.24
CZT	387	283	250	0.09

charge sharing events are heavily dependent on the pixel pitch and generated electron cloud size. SPDI events occur when gamma rays Compton scatter and both the initial gamma ray and scattered gamma ray are collected by the same pixel (see Fig. 4.3a). The probability of SPDI increases with larger pixel pitch. Charge sharing events occur when a single gamma ray interacts under or near the gap between pixels, and a portion of the generated electron cloud is collected by both of the neighboring pixels (see Fig. 4.3b). The probability of charge sharing decreases with larger pixel pitch. For SPDI events, only one pixel triggers as a result of two interactions, while for charge sharing events, two pixels trigger as a result of a single interaction. In both cases, the events are improperly reconstructed because the number of interactions does not match the number of triggered pixels.

Fig. 4.4 shows the SPDI and charge sharing event fractions for 662 keV photopeak events in TlBr and CZT. Two detector sizes are shown, one for a typical TlBr detector, 11 x 11 x 5 mm^3, and one for a typical CZT detector, 20 x 20 x 15 mm^3. Even though

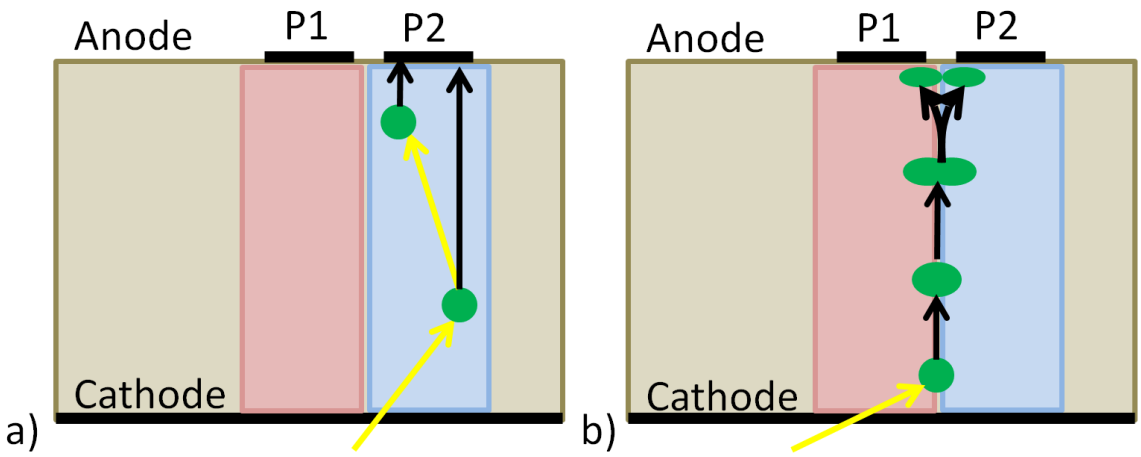

Figure 4.3: a) Schematic of single-pixel double interaction (SPDI) and b) charge sharing events. In both figures, yellow lines indicate gamma- rays, black lines indicate electron cloud travel paths and green circles indicate electron clouds. For SPDI events, two interactions occur but only one pixel (P2) collects charge. For charge sharing events, only one interaction occurs but both pixels (P1 and P2) collect charge. Both event types result in poor reconstruction.

.

the stopping power is lower in CZT, it has a higher Compton scatter cross section compared to TlBr, and as a result, a higher SPDI fraction. For pixel pitches on the order of millimeters, the charge sharing probability increases when the electron cloud size is larger than approximately 500 μm (i.e. when the cloud size is the same order as the pixel pitch). As a result, the charge sharing fraction at 662 keV is larger for TlBr compared to CZT because a larger fraction of events (24% compared to just 8%) result in an electron cloud greater than 500 μm (see Table 4.1). Both of these results are counterintuitive; if bremsstrahlung is not considered, a higher density material (TlBr) should result in a lower charge sharing fraction. Similarly, if the overall Compton scattering cross section is not considered, the higher density material (TlBr) should have a higher probability of SPDI because the scattered gamma ray is more likely to be captured near the first interaction location. Through simulation, these processes can be properly characterized, and the optimal pixel pitch can be determined.

A first order approximation of the optimal pixel size is the intersection of the two event fractions. This minimizes the misclassification rate when SPDI and charge

sharing events are equally weighed. For 5 mm thick detectors, the optimum pixel pitch is ∼1.7 mm for TlBr and ∼1.5 mm for CZT. However, this does not account for the small pixel effect (pitch-to-thickness ratio which allows effective single-polarity charge sensing) which dictates that the pitch for 5 mm thick detectors should be no greater than about 1 mm. For 15 mm thick detectors, the optimal pixel pitch is ∼2.1 mm for TlBr and ∼1.8 mm for CZT. The small pixel effect will still occur for 15 mm thick detectors at these pixel pitches. In general, the optimum pitch is slightly greater for TlBr compared to CZT because of the higher bremsstrahlung energy, which increases with effective atomic number.

4.1.3 X-Ray Identification Rates

As discussed in Sec. 3.3.5, part of this work involved using Tl characteristic x-rays to identify photoelectric interactions. In the simulation, if a Tl characteristic x-ray was identified (i.e. one energy deposition E_i from a multiple-pixel event was within $E_L < E_i < E_H$ where E_L and E_H are bounds around the x-ray energies) there were two possibilities:

1. The event was a photoelectric interaction and counted as a true positive
2. The event was not a photoelectric interaction and counted as a false positive.

The output from the Geant4 simulation, after the charge was drifted and collected by the pixels, was compared to the actual event (whether or not it was a photoelectric event, which was known from the simulation) to determine the true positive and false positive rates for multiple-pixel events. Specifically, the true positive event fraction was the total number of multiple-pixel photopeak events (true) in which one energy deposition was within $E_L < E_i < E_H$ (positive), divided by the total number of multiple-pixel events.

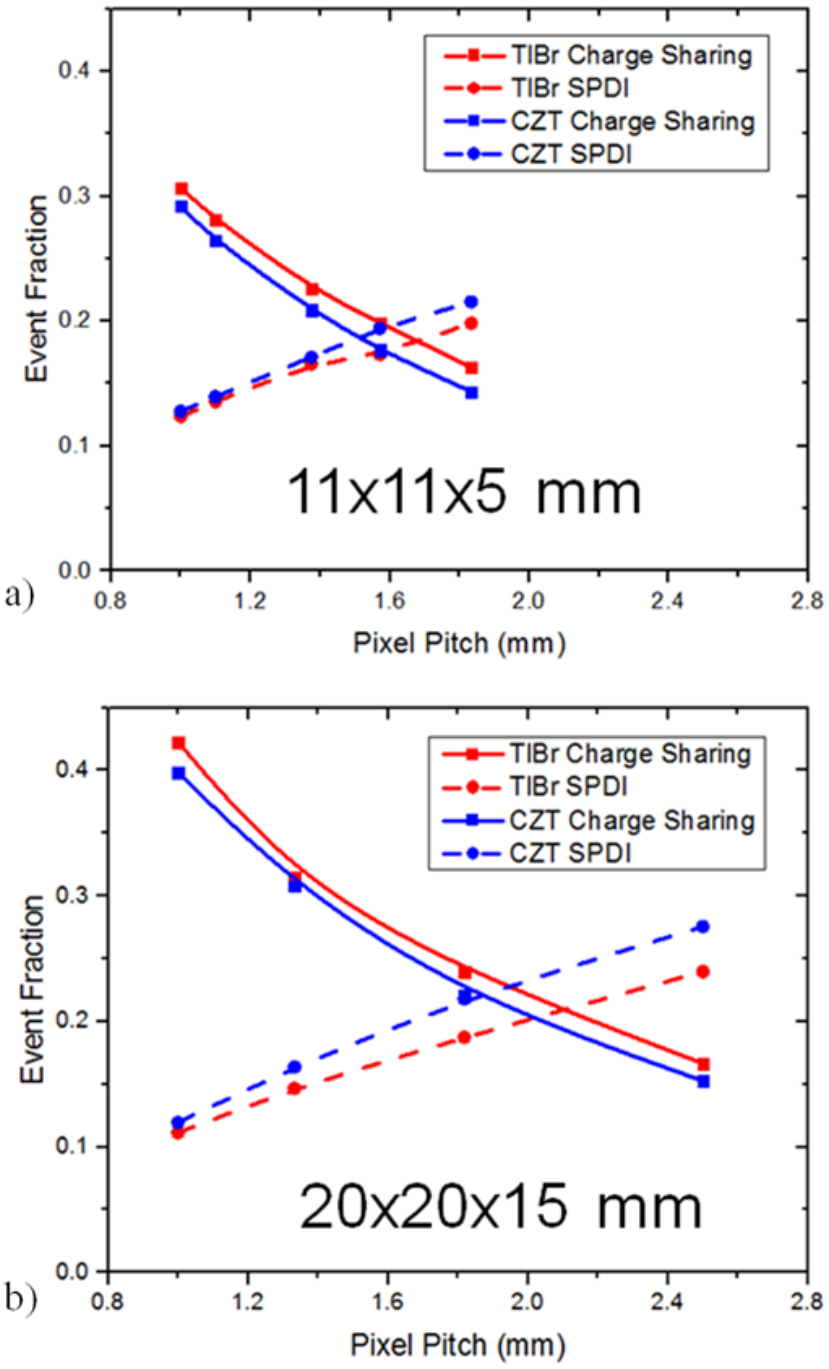

Figure 4.4: Charge sharing and SPDI event fractions for a) 11 x 11 x 5 mm^3 and b) 20 x 20 x 15 mm^3 TlBr and CZT detectors.

Table 4.2: Comparison of simulated and experimental event fractions for an 11 x 11 x 5 mm^3 TlBr detector.

	1 Pixel Fraction	2 Pixel Fraction	3 Pixel Fraction	4 Pixel Fraction
Simulation	0.33	0.41	0.19	0.05
Experimental	0.33	0.38	0.20	0.07

Fig. 4.5 shows true and false positive rates for 11 x 11 x 5 mm^3 and 20 x 20 x 15 mm^3 TlBr detectors. For smaller pixel pitches, characteristic x-rays have a shorter distance to travel to escape the pixel and the true positive rates increase. Similarly, when pixel pitches decreases, charge sharing probabilities also increase. Because charge sharing can result in a small amount of charge deposited in a neighbor pixel, the increased charge sharing at small pixel pitch also increases the false positive rate. For 1 mm pixel pitch (current TlBr design), the true positive event rate for correctly identifying a Tl characteristic x-ray is $\sim$0.15. This means that 15% of all multiple-pixel events are correctly identified as known photoelectric events. The true positive rate for only photopeak events (as opposed to all events) can be calculated by dividing by the photofraction. However, photofractions are not always known in the presence multiple unknown sources. Note that for a large number of events, false positives (assuming a photoelectric interaction occurred when it did not) will not greatly affect the energy spectrum.

4.1.4 Simulation Validation

The Geant4 model was validated by comparing experimental and simulated results. SPDI and charge sharing events greatly affect the number of triggered pixels. Therefore, if these processes are not modeled correctly, the simulated trigger fractions will not match experimental data. Table 4.2 shows a comparison of simulated and experimental event fractions for an 11 x 11 x 5 mm^3 TlBr detector. In all cases, the event fractions agree to within 2%.

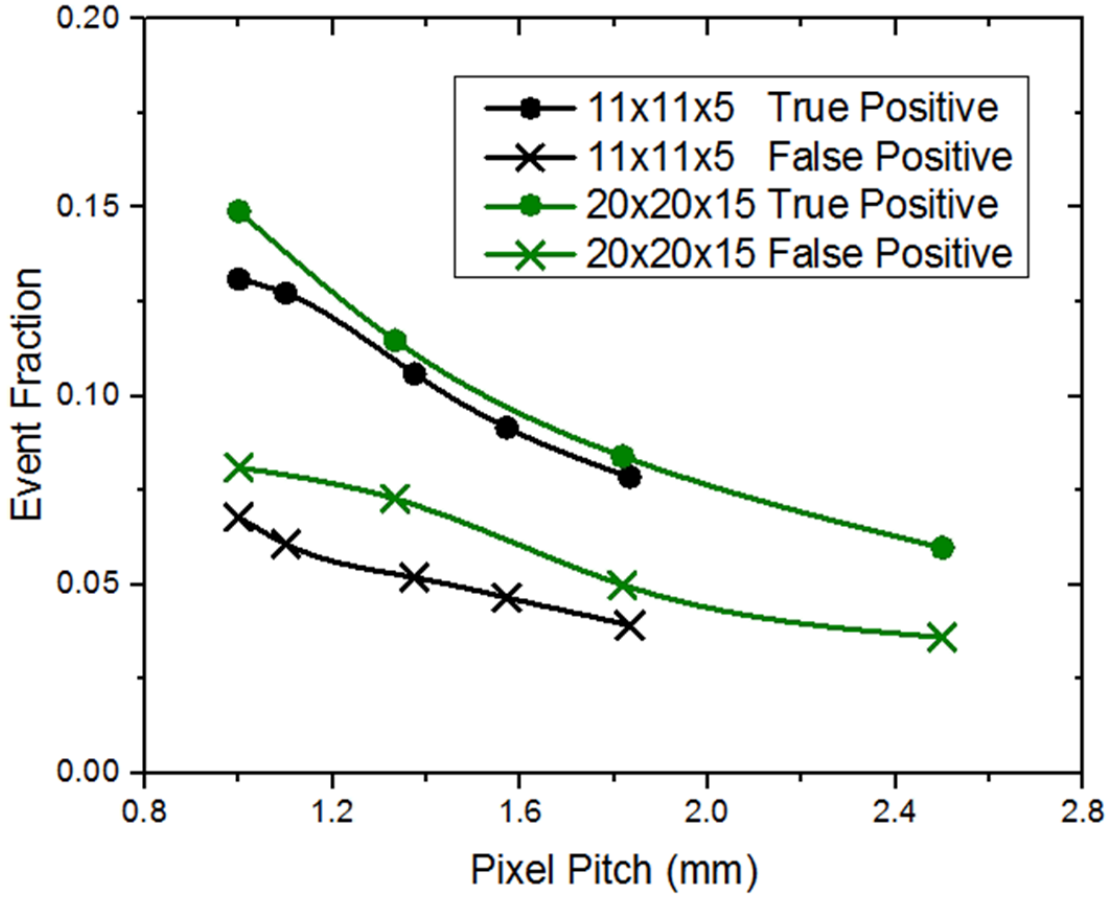

Figure 4.5: True positive and false positive event fractions for two different sized TlBr detectors.

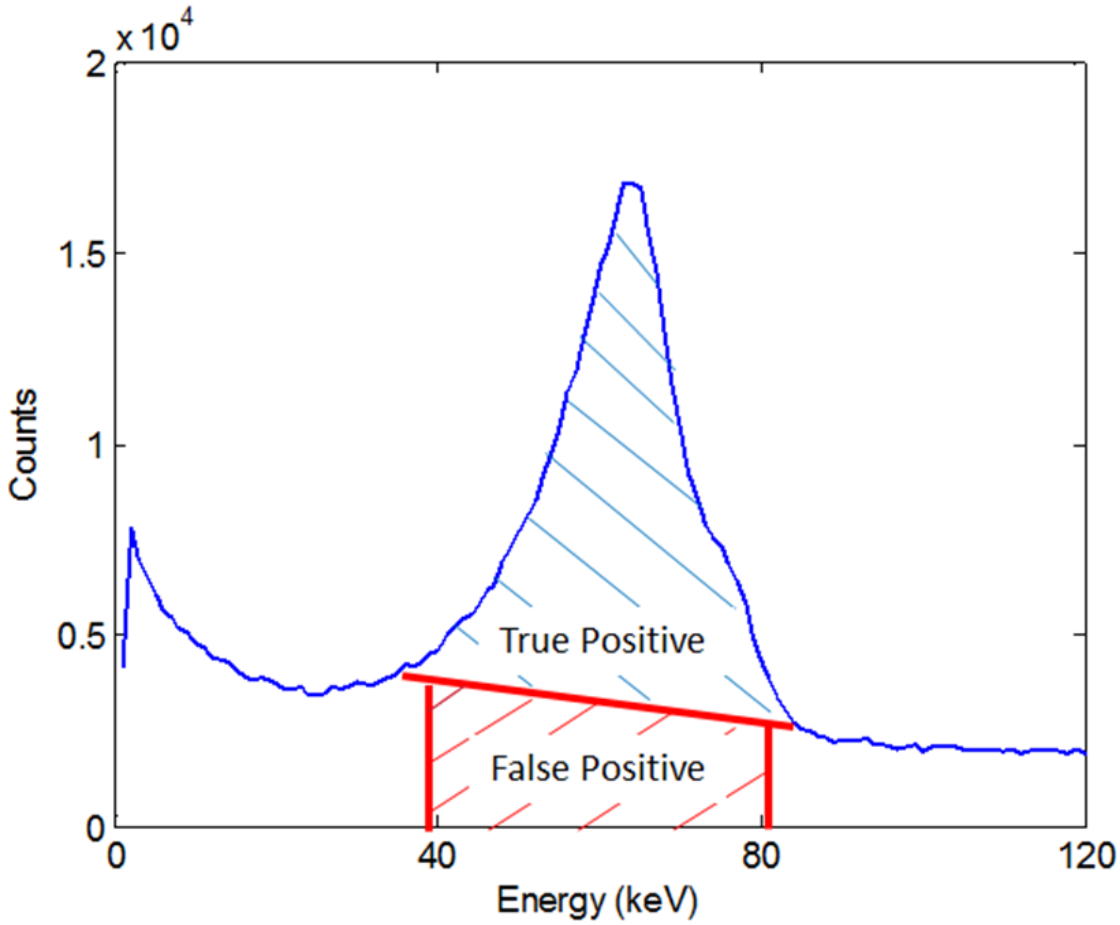

Figure 4.6: Experimental data of single pixel energies from two-pixel events showing how the true positive and false positive fractions were estimated.

The simulated true and false positive x-ray identification rates were also compared to experimental results. Fig. 4.6 shows experimental data of single pixel energies from two-pixel events, zoomed in on the x-ray region. Only one peak was observed for all four dominate energies because of poor energy resolution. The true positive event fraction was the peak count integral divided by the total number of two-pixel events. Similarly, the false positive event fraction was the integral of the counts under the peak divided by the total number of two-pixel events. Table 4.3 shows the comparison between simulated and experimental results. The simulated true/false positive fractions match experimental data, validating the Geant4 model. The effect of energy resolution on x-ray filtering is discussed in Sec. 7.2.2.

Table 4.3: Comparison of simulated and experimental true and false positive fractions for two-pixel events on an 11 x 11 x 5 mm^3 TlBr detector.

	True Positive	False Positive
Simulation	10.3%	6.1%
Experimental	9.9%	5.0%

4.2 Weighting Potential for Mobility-Lifetime Correction Factor

Maxwell [64] was used to model electric fields and calculate weighting potentials for different anode configurations (pixel pitch and detector thicknesses). This was required to calculate the correction factor k to the two-bias method for determining $\mu_e\tau_e$ in pixelated detectors (see Eq. 3.10). The rest of this section describes how simulated weighting potentials were used to calculate k and how the methodology was validated by comparing the simulated results to experimental data from 15 mm thick CZT detectors.

4.2.1 Calculating the Correction Factor k

The Shockley-Ramo theorem states that the induced charge on an electrode is equal to the generated charge multiplied by the weighting potential change (see Sec. 2.1). The two-bias method for calculating $\mu_e\tau_e$ assumes that any trapped charge does not contribute to the signal because it does not go through any weighting potential change (the ideal weighting potential is exactly zero throughout the bulk).

Consider the case outlined in Fig. 4.7 where an interaction occurs at depth z = 4 mm. Note that z = 4 mm is an arbitrary depth and was chosen because it highlights the different effects from trapped versus untrapped charge. While typical $\mu_e\tau_e$ calculations are done at the cathode surface (z = 5 mm), electron clouds from those events must pass through z = 4 mm. To simplify the scenario, let Q_t be all the trapped charge and let it drift 2 mm before being trapped. If Q_c is the collected,

untrapped charge, then the total generated charge is $Q_T = Q_t + Q_c$.

If N_1' is the signal from a pixelated weighting potential and N_1 is the signal from the ideal weighting potential assumed in Eq. 3.8, then N_1' has an added component compared to N_1 because trapped charge Q_t goes through a weighting potential change, and therefore contributes to the signal, in the pixelated case but not in the ideal case. N_1' also has a subtracted component because collected charge Q_c, does not go through the full weighting potential in the pixelated case. The relationship between N_1 and N_1' in the example outlined in Fig. 4.7 is:

$$N_1' = N_1 \left[1 - \phi(4)\right] + \left(N_0 - N_1\right) \left\langle \Delta\phi(4,2) \right\rangle \tag{4.1}$$

where $\phi(4)$ is the pixelated weighting potential at z = 4 mm, and $\langle \Delta\phi(4,2) \rangle$ is the average change in pixelated weighting potential between z = 4 mm and z = 2 mm. The first term represents the subtracted signal as a result of Q_c not going through the full weighting potential. The second term represents the added signal from Q_t which goes through a non-zero weighting potential change. Note that if cathode side events are chosen, the first term goes to N_1.

In the real case, a small amount of charge δq_t is trapped when the untrapped generated charge goes through a incremental depth, δz. If the charge drift is divided into a number of depth bins, then Eq. 4.1 can be replaced with a finite sum:

$$\begin{aligned} N_1'(z_j) = {} & N_1(z_j) \left[1 - \phi(z_j)\right] \\ & + \sum_{i=1}^{j} \left[N_1(z_{i-1}) - N_1(z_i)\right] \left[\frac{\phi(z_i) - \phi(z_{i-1})}{2}\right] \end{aligned} \tag{4.2}$$

where z_j is the j^{th} bin distance from the anode. Again, the first and second terms account for the trapped and untrapped charge, respectively. $N_1(z_i)$ is calculated using

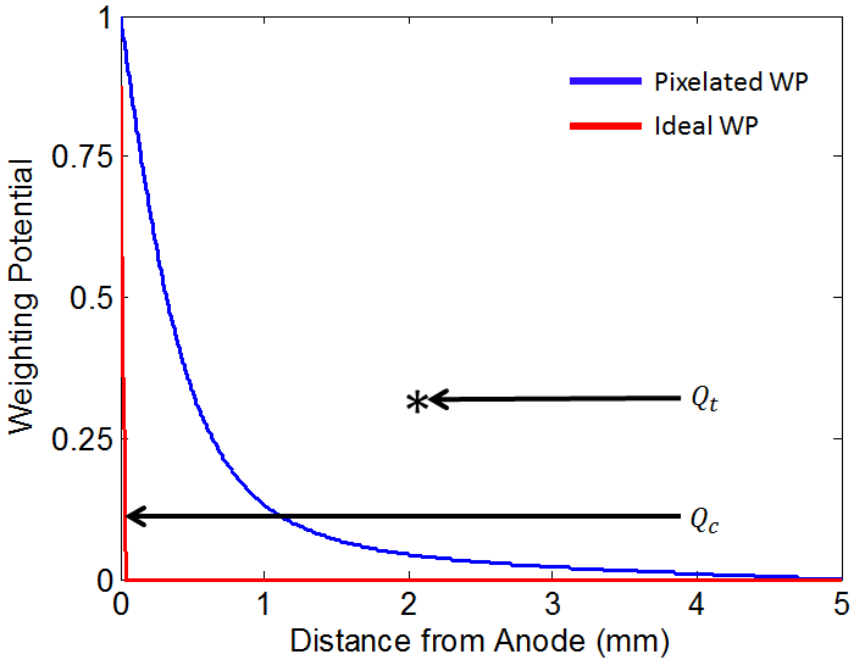

Figure 4.7: Weighting potential for a 5 mm thick ideal detector (red) and 5 mm thick pixelated detector with 1 mm pitch (blue). The total charge generated at 4 mm is $Q_T = Q_t + Q_c$.

Eq. 3.9, therefore, $N_1(z_{i-1}) - N_1(z_i) = \delta q_t$.

Fig. 4.8 shows N_1 and N_1' calculated using Eqs. 3.9 and 4.2, respectively, for the ideal and pixelated weighting potentials shown in Fig. 4.7. One-thousand depth bins were used for the calculations. This was chosen to ensure that the average weighting potential change, multiplied by the trapped signal, approximated the signal induced by the trapped charge. The number of bins was increased until a constant solution was achieved. The signals are normalized because N_0 was set to one. The detector bias V_1 was 1000 V and the $\mu_e\tau_e$ was set to 3 x 10^{-3} cm^2/V, typical values for 5 mm thick semiconductor detectors. Near the cathode surface, the second term in Eq. 4.2 dominates and $N_1' > N_1$. Through the rest of the bulk, the first term dominates and $N_1' < N_1$. The same method was used to generate N_2 and N_2' at $V_2 = 1500$ V.

Fig. 4.9 shows the calculated $\mu_e\tau_e$ using Eq. 3.8 for the pixelated and ideal weighting potentials shown in Fig. 4.7. The N_1 and N_2 signals calculated above (e.g.

N_1 shown in Fig. 4.8) were used for the ideal case and the N_1' and N_2' signals were used for the pixelated case. The N_1, N_2, N_1', and N_2' signals were calculated using $\mu_e\tau_e$ = 3 x 10^{-3} cm^2/V; therefore, the expected $\mu_e\tau_e$ at all depths was 3 x 10^{-3} cm^2/V. Using the ideal weighting potential, the calculated $\mu_e\tau_e$ (red curve in Fig. 4.9) equals the expected $\mu_e\tau_e$ at all depths except right at the anode where there is a rapid change in weighting potential (note that the rise in the calculated $\mu_e\tau_e$ of the ideal weighting potential case near the anode is the result of binning; at some point, the weighting potential had to increase to one). For the pixelated detector, the calculated $\mu_e\tau_e$ (blue curve in Fig. 4.9) is consistently overestimated compared to the expected $\mu_e\tau_e$. At the cathode surface, where most published work using the two-bias method calculate N_1 and N_2, the $\mu_e\tau_e$ is overestimated by roughly 10%. Therefore, a correction factor of $k = 0.896$ needs to be applied to $\mu_e\tau_e$ calculations utilizing the two-bias method when cathode-side events are used with 5 mm thick pixelated detectors with 1 mm pixel pitch.

Fig. 4.10 shows the calculated $\mu_e\tau_e$ for a 15 mm thick detector with 1.72 mm pitch. The $\mu_e\tau_e$ was set to 25 x 10^{-3} cm^2/V and the biases were V_1 = 2500 V and V_2 = 3000 V. The selected electrode configuration, $\mu_e\tau_e$, and biases in Fig. 4.10 matched the experimental parameters discussed in Sec. 4.2.2. While the profile in Fig. 4.10 is similar to Fig. 4.9, the magnitude of the overestimation decreased because the weighting potential of a 15 mm thick detector with 1.72 mm pixel pitch is closer to the ideal weighting potential. The correction factor for this geometry is $k = 0.941$.

Table 4.4 shows cathode-side correction factors for common single-polarity charge sensing electrode configurations with 100 μm gap between pixels. Uncertainties were estimated as the standard deviation of the correction factor for different pixel locations (i.e. center pixel, edge pixel, between center and edge pixel). Uncertainties for all cases was less than 0.33% which is significantly lower than typical uncertainties reported for $\mu_e\tau_e$ values ($\sim$ 5-10%). The correction factor does not depend on the

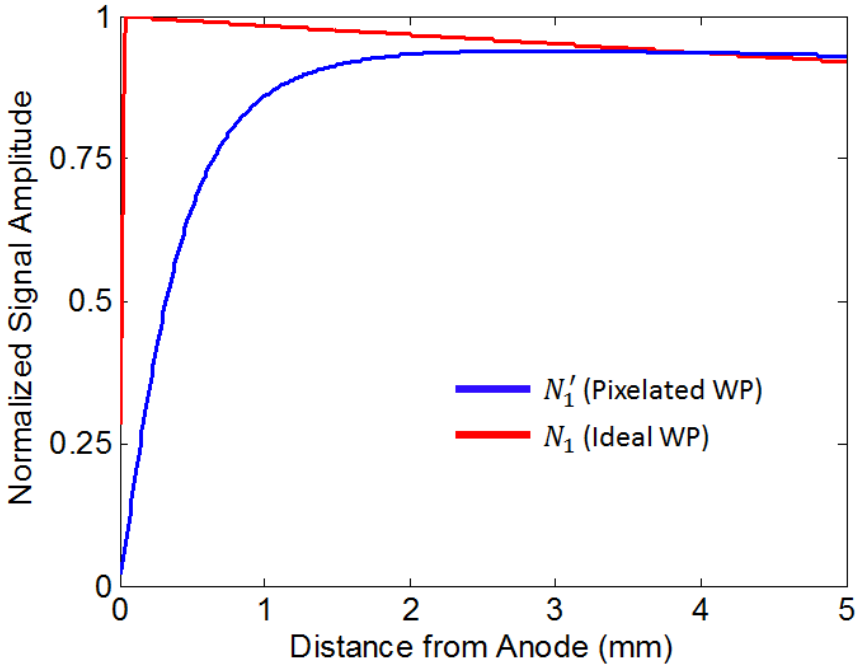

Figure 4.8: Normalized signal amplitudes as a function of depth for pixelated and ideal weighting potentials.

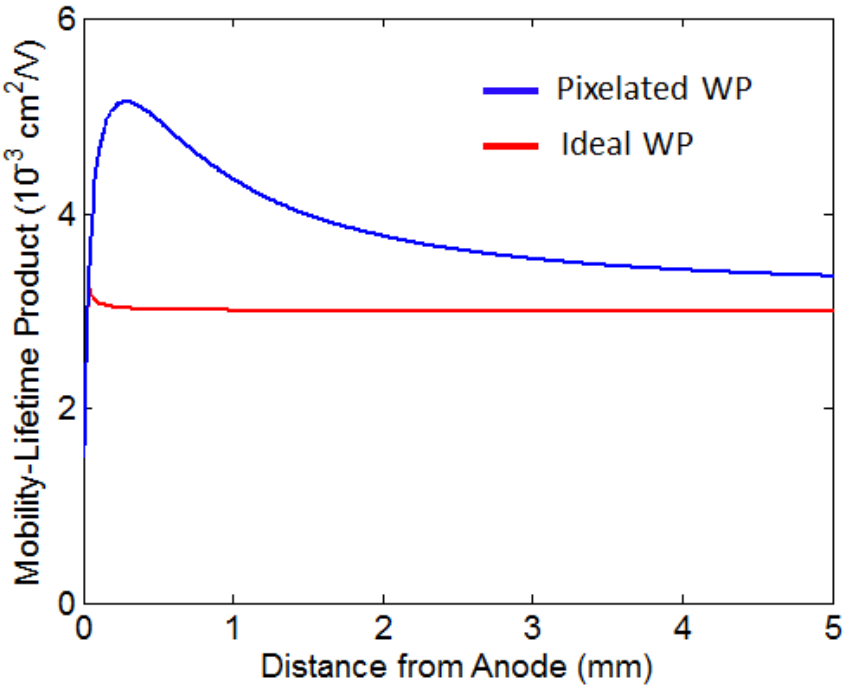

Figure 4.9: Calculated $\mu_e\tau_e$ for an ideal detector and for a 5 mm thick pixelated detector with 1 mm pitch. The true $\mu_e\tau_e$ was set to 3 x 10^{-3} cm^2/V.

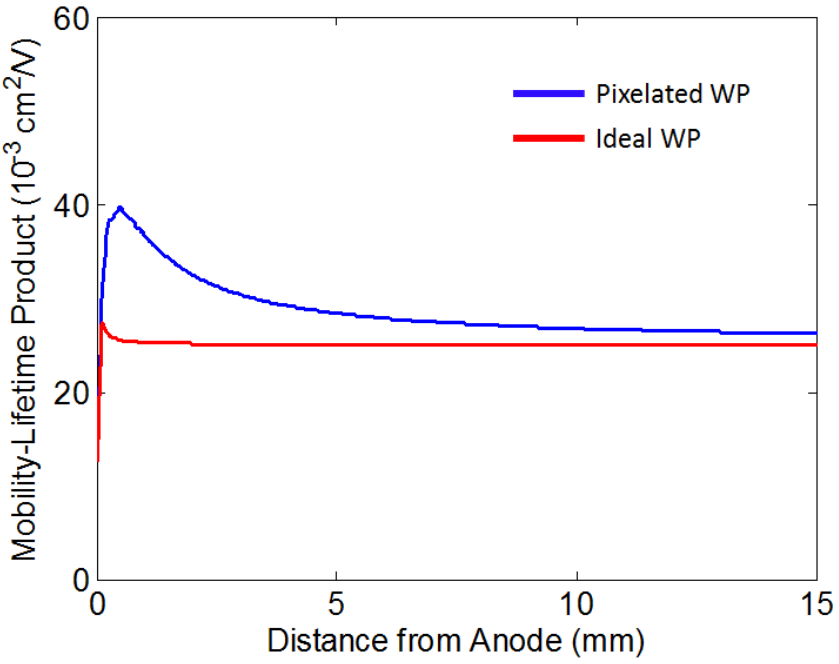

Figure 4.10: Calculated $\mu_e\tau_e$ for an ideal detector and for a 15 mm thick pixelated detector with 1.72 mm pitch. The true $\mu_e\tau_e$ was set to 25 x 10^{-3} cm^2/V

$\mu_e\tau_e$ or the bias values V_1 and V_2 because the origin of the problem is the shape of the weighting potential. This was confirmed by changing V_1, V_2, and $\mu_e\tau_e$; no change was observed in the resulting profile. When $\mu_e\tau_e$ was changed, the relative scale of the calculated $\mu_e\tau_e$ also changed; however, the fractional profile, and therefore the correction factor, was unaffected.

Fig. 4.11 shows correction factors for different pixel pitch to detector thickness ratios (PDR) when a 100 μm and 200 μm gap between pixels was used. In order to maintain the correct pitch, the pixel pad size was decreased by 100 μm for the 200 μm cases. The correction factor changed by less than 0.003 for all configurations. Therefore, the gap size does not significantly affect the correction factor.

Fig. 4.12 shows correction factors as a function of PDR. Correction factors are linear as a function of PDR, except for the 5 x 5 x 5 mm^3 detector with 2 mm pixel pitch. For this case, the pixel was large compared to the detector face, and the correction factor decreased. When the detector face was increased to 40 x 40 mm^2,

Table 4.4: Correction factors for common single-polarity charge sensing configurations with 100 μm gap between pixels. The errors on the correction factors are less than 0.003.

Dimensions (mm^3)	Pixel Pitch (mm)	Pitch/Thickness	Correction Factor
5x5x5	1	0.2	0.896
5x5x5	2	0.4	0.796
10x10x5	2	0.4	0.812
10x10x10	1	0.1	0.949
10x10x10	2	0.2	0.896
20x20x10	1	0.15	0.924
20x20x10	1.5	0.25	0.876
20x20x10	2.5	0.1	0.950
20x20x15	1	0.067	0.967
20x20x15	1.72	0.115	0.941
20x20x15	2	0.133	0.932
40x40x5	1.25	0.25	0.877
40x40x5	1.4	0.28	0.863
40x40x5	1.75	0.35	0.833
40x40x5	2	0.4	0.813

the correction factor was consistent with the other data. The least squares line of best fit for all electrode configurations except the 5 x 5 x 5 mm^3 detector with 2 mm pitch was:

$$k = -0.459 * PDR + 0.993. \tag{4.3}$$

The errors on the slope and intercept were 0.007 and 0.002, respectively. Eq. 4.3 provides a simple method to calculate the cathode-side correction factor for the two-bias method. Eq. 4.3 is limited to detector sizes modeled in this work (listed in Table 4.4), specifically, detectors equal to or larger than 5 x 5 x 5 mm^3 with 1 mm pitch, equal to or smaller than 20 x 20 x 15 mm^3 with 2 mm pitch or 40 x 40 x 5 mm^3 with 2 mm pitch, and with a PDR between 0.07 and 0.4. This range encompasses typical geometries that have utilized the two-bias method [9, 18, 65, 66, 67]. Most of the contribution to the correction factor results from the rapid weighting potential change near the anode. The extent of the rapid change region is roughly equal to

the detector pixel pitch. Therefore, the fraction of the detector which has a non-ideal weighting potential changes linearly with PDR. As a result, Eq. 4.3 is also linear with PDR.

Fig. 4.13 shows residuals between the best-fit line and correction factors. All residuals except the 5 x 5 x 5 mm^3 detector with 2 mm pitch are within 0.9% of the best-fit line. There is a parabolic trend between the true value of the correction factor and the linear fit based on the PDR. In practice, this offset is much smaller compared to the uncertainty inherent in the $\mu_e\tau_e$ measurement. For high performing detectors ($< 1\%$ FWHM at 662 keV), most uncertainty comes from uncertainty in the interaction depth [59]. Large pixelated CZT detectors have a depth uncertainty of about 2.5% (40 depth bins across 15 mm). By propagating the 0.9% maximum error in k through Eq. 3.10, the $\mu_e\tau_e$ uncertainty increases from 2.5% to 2.7%, a marginal increase on the lowest uncertainty case. If the error increase is unacceptable, the true correction factor can be calculated by modeling the weighting potential using the exact device dimensions.

4.2.2 Methodology Validation Using 15 mm Thick CZT Detectors

Previous work has shown that the CAR accurately determines the interaction depth for 662 keV gamma rays in 15 mm thick pixelated CZT detectors [68]. The CAR parameter was used to segment 662 keV energy spectra of three detectors into 40 depth bins. Eq. 3.8 was evaluated as a function of depth using depth-dependent photopeak centroids as N_1' and N_2'. The $\mu_e\tau_e$ profiles calculated for three detectors is shown in Fig. 4.14. Note that the real $\mu_e\tau_e$ profile is likely much more uniform across the bulk; the apparent non-uniformity is a result of using the two-bias method on a pixelated detector. The profiles are not shown for depths under 3.5 mm because of high uncertainty, a result of the fast anode-side weighting potential change.

While the general shape of Fig. 4.14 matches Fig. 4.10 (the $\mu_e\tau_e$ profile is fairly

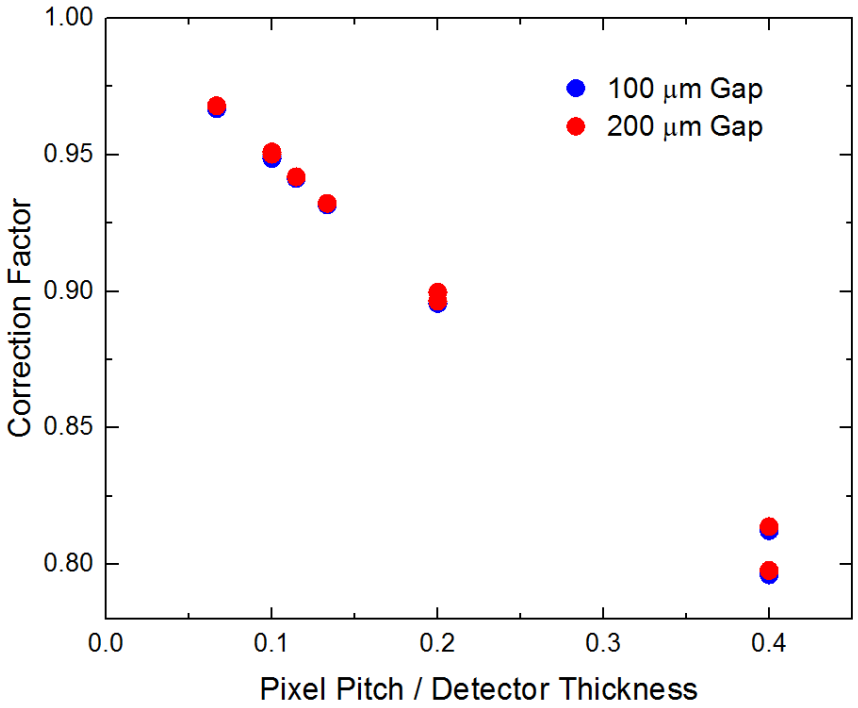

Figure 4.11: Correction factor for various PDR using 100 μm (blue) and 200 μm (red) gaps.

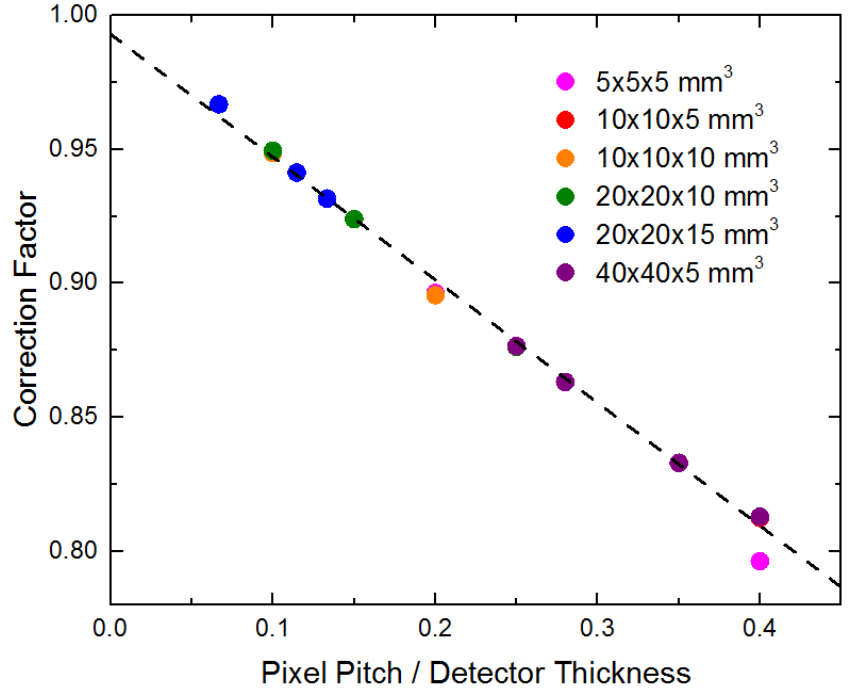

Figure 4.12: Correction factor for various pitch / thickness ratios for 100 μm gaps. The uncertainties were all less than 0.003.

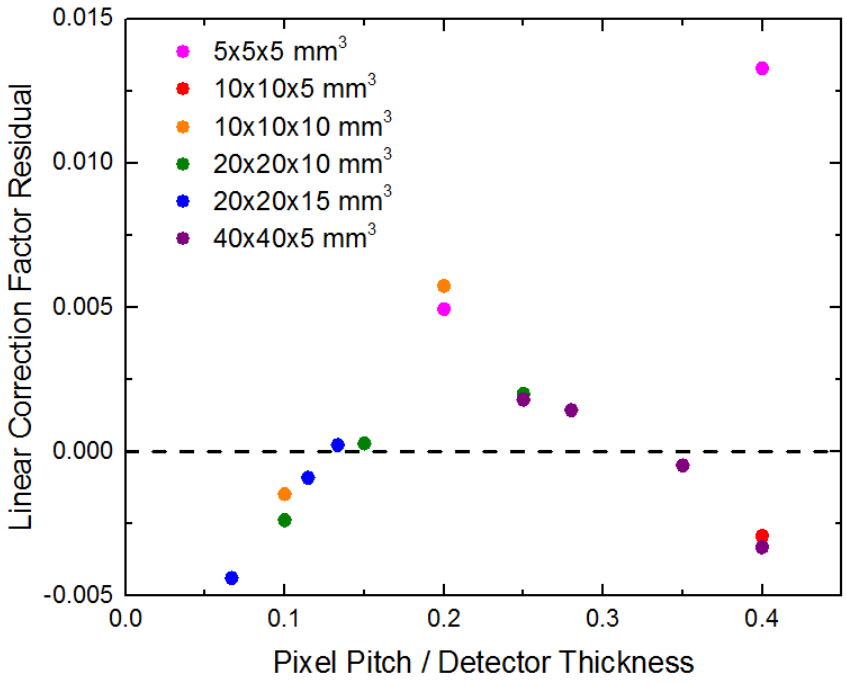

Figure 4.13: Correction factor residuals from the linear least-squares line of best fit.

uniform through most of the bulk and rises quickly near the anode) the coefficient of determination between the $\mu_e\tau_e$ values for detector 5R-9 (green curve in Fig. 4.14, shown again in green curve in Fig. 4.15) and the simulated values (blue curve in Fig. 4.15) is only $R^2 = 0.17$. Additionally, the specific depth where the profile changes from uniform to sharply rising varies from detector to detector.

It is well known that the internal electric field profiles for semiconductor detectors are non-uniform, especially for thicker detectors [54, 69]. Instead, the electric field is weaker near the center of the device and stronger near both electrodes. Fig. 4.15 shows the expected $\mu_e\tau_e$ profile for a 15 mm thick detector with 1.72 mm pitch with expected $\mu_e\tau_e = 28$ x 10^{-3} cm^2/V. The profile is shown for both a uniform electric field and one that is weaker in the center (an approximation of the expected electric field in detector 5R-9). The cathode-side $\mu_e\tau_e$ calculation is largely unaffected by the non-uniform electric field, but the transition depth between uniform $\mu_e\tau_e$ and sharply rising $\mu_e\tau_e$ changes. Additionally, there is a slight dip near the cathode side before

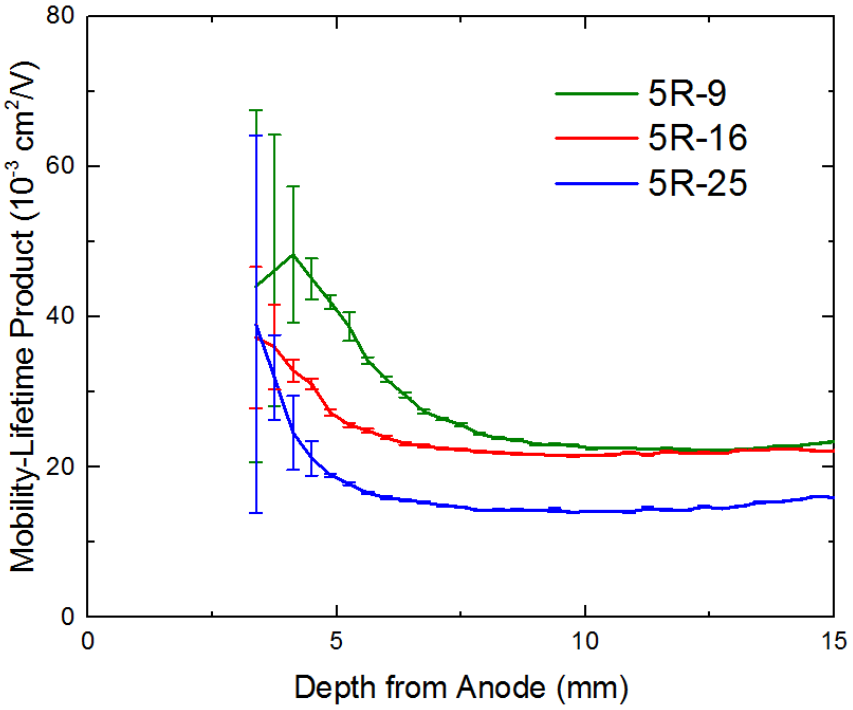

Figure 4.14: Depth dependent $\mu_e\tau_e$ calculated from Eq. 3.8 in a 15 mm thick CZT detector with 1.72 mm pixel pitch.

the $\mu_e\tau_e$ profile increases toward the anode side for the non-uniform electric field case. When the electric field effects are corrected, the coefficient of determination between the experimental $\mu_e\tau_e$ (green curve in Fig. 4.15) and the simulated $\mu_e\tau_e$ values (red curve in Fig. 4.15) increases to $R^2 = 0.90$, indicating much better agreement.

4.2.3 Description of Other Effects

Ref. [60] outlines other effects which can change $\mu_e\tau_e$ calculations, including shaping time, particle type, and particle energy. The two-bias method, unlike Hecht fitting, is insensitive to ballistic deficit as long as shaping times are much longer than anode collection times. Anode collection times are typically much shorter than full drift times for single-polarity charge sensing configurations. Similarly, the two-bias method is insensitive to surface trapping and will not show a significant difference for particle type and energy. Using high energy particles improves the signal to noise

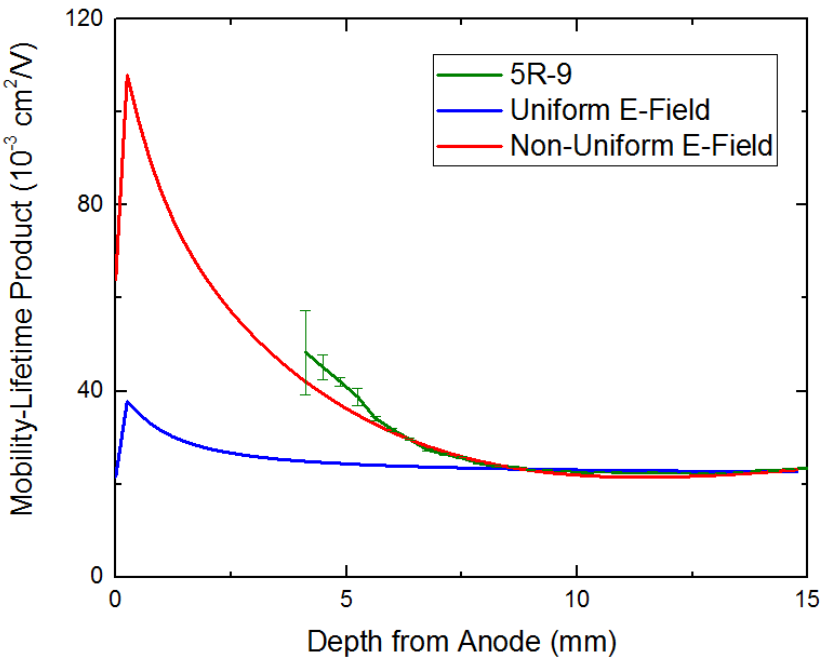

Figure 4.15: Effect of a non-uniform electric field on the $\mu_e\tau_e$ profile.

ratio and, as a result, the precision of $\mu_e\tau_e$, but not the accuracy.

Both Hecht fitting and the two-bias method are sensitive to non-uniform electric fields. If a high resolution electric field profile is known, it can be used to correct the $\mu_e\tau_e$ profile using the more complete form of Eq. 3.8:

$$\mu_e\tau_e = \frac{1}{\ln\left(N_1/N_2\right)}\left[\int_0^z \frac{1}{E_2(z')}dz' - \int_0^z \frac{1}{E_1(z')}dz'\right] \tag{4.4}$$

where E_1 and E_2 are the electric field profiles at different biases. Note that for a constant electric field, Eq. 4.4 reduces to Eq. 3.8.

While there is currently no technique to measure the electric field profile in thick semiconductor detectors with the fidelity required to use Eq. 4.4, the profile can be approximated with continuous functions comparable to profiles obtained from cathode waveform analysis [54]. These electric field profiles can be used to estimate the magnitude of the non-uniform electric field effect on the $\mu_e\tau_e$ measurement.

Fig. 4.16 (created by M. Streicher for Ref. [70]) shows continuous functions of

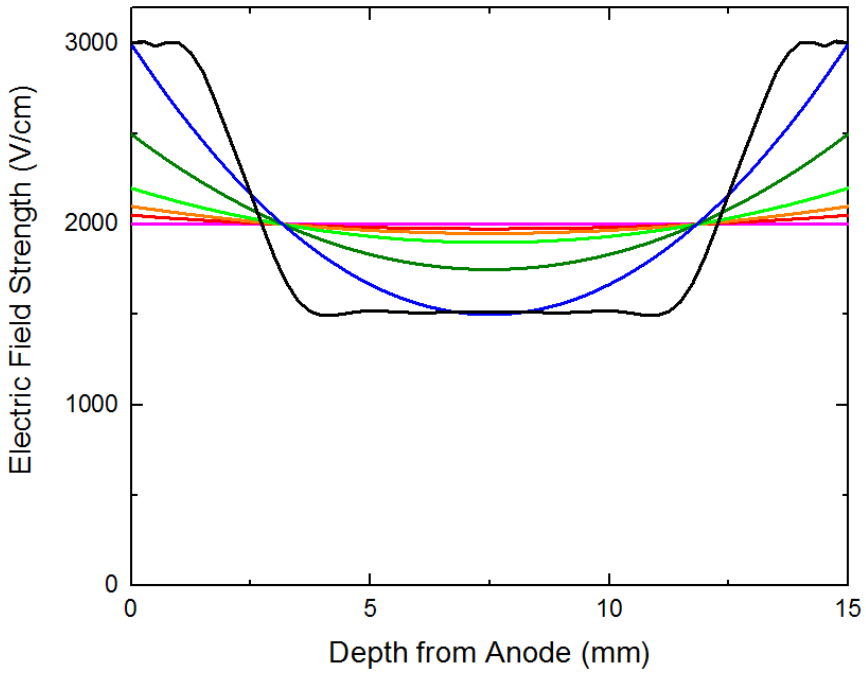

Figure 4.16: Continuous function, non-uniform electric field profiles with similar characteristics of profiles obtained from cathode signal analysis.

non-uniform electric field profiles. Using these profiles and Eq. 4.4, the resulting $\mu_e\tau_e$ profiles were calculated and are shown in Fig. 4.17 (also created by M. Streicher for Ref. [70]). The colors are consistent between the two figures. The magnitude of non-uniform electric field effects to the two-bias method was estimated by calculating the change in $\mu_e\tau_e$ value at the cathode side. This was estimated to be 30% for the most extreme electric field profile (black curve) and 5% for a moderate profile (dark green curve). It should be noted that thiner 5 mm thick detectors tend to have a much more uniform electric field compared to thicker 15 mm thick detectors, in which case the weighting potential correction dominates. In either case, if the electric fields effects are corrected, the weighting potential correction factor must be applied.

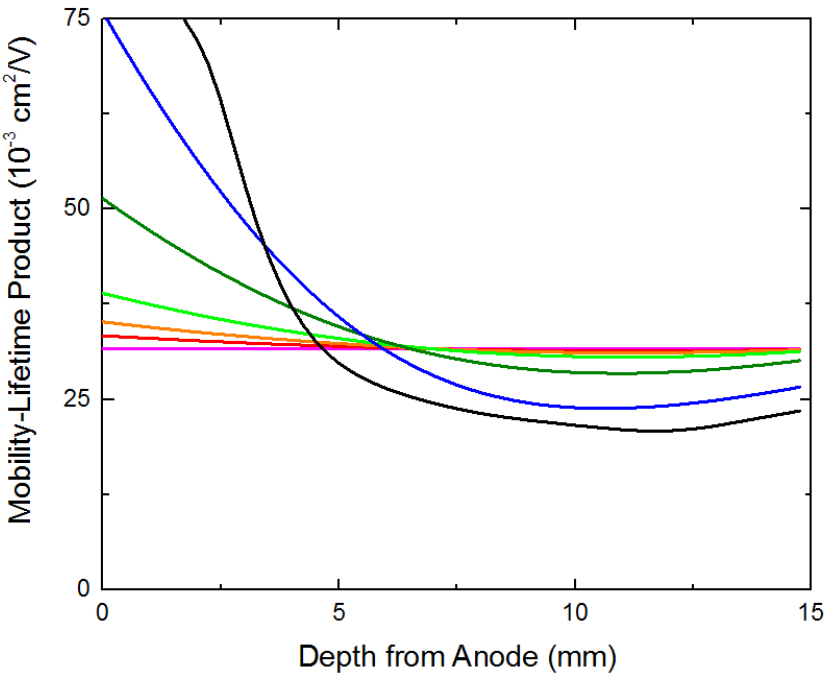

Figure 4.17: Mobility-lifetime profiles for non-uniform electric fields shown in Fig. 4.16 (the colors are consistent between figures). Weighting potential effects were controlled by using an ideal weighting potential.

4.3 Conclusions

Through Geant4 simulation, energy depositions from gamma-ray events were used to calculate electron cloud sizes. It was found that while TlBr has a peak at lower electron cloud size compared to CZT, the bremsstrahlung component creates a large-cloud tail which increases the number of charge sharing events. Using electron cloud data, single-pixel double-interaction and charge sharing event ratios were calculated. Geant4 was also used to model Tl characteristic x-rays and calculate true positive and false positive identification fractions. These simulated values were validated with experimental data and matched to within 2%.

Using Maxwell simulations, it was shown that while the two-bias method provides a simple way to calculate $\mu_e\tau_e$ for single-polarity charge sensing devices, the electrode geometry must be taken into account or the calculated $\mu_e\tau_e$ will be systematically overestimated for non-ideal weighting potentials. Simulations were used to model

weighting potentials and calculate correction factors for the two-bias method. The method was verified by comparing results to a 15 mm thick CZT detector. The general shape of the simulated and experimental cases matched. The profile differences were likely caused by non-uniform electric fields.

CHAPTER V

Characterization and Improvement of TlBr During $-20\,^{\circ}\mathrm{C}$ Operation

5.1 Performance of Stable Detectors

To date, the most consistent way to achieve long term stability ($\sim$ months) with TlBr detectors, is to cool them to $-20\,^{\circ}\mathrm{C}$. Cooling detectors reduces ionic conduction which is the root cause of polarization. However, even under stable conditions, the performance can vary from detector to detector depending on material quality (bulk effect) and surface quality or processing. Poor performance can be isolated to the bulk or surface through depth-dependent analysis of photopeak centroids, energy resolution, and mobility-lifetime product. Each TlBr detector behaved slightly differently; however, general groupings were made depending on overall bulk material and surface quality. This section describes characteristics and performance of TlBr detectors with good bulk material and good surface properties, good bulk material and poor surface properties, and poor bulk material. In general, if the bulk material was poor, there was no method to determine the surface quality because the effects from the poor bulk material dominated the depth-dependent signals.

5.1.1 Good Bulk Material and Good Contacts

The best performing TlBr detectors were those with good bulk material and surface properties. Bulk material affects charge transport while, surface properties affect the final charge collection at the electrode interface. Fig. 5.1 shows a single-pixel depth-corrected ^{137}Cs spectrum for detector 935-16B1L. All prominent features were observed:

1. Photopeak: Full energy deposition of the mono-energetic 662 keV gamma ray.

2. Tl-Escape Peak: The generated Tl characteristic x-ray has sufficient energy to escape the pixel where the photoelectric interaction occurred. If the x-ray escapes the detector, interacts in the guard ring (which is not read out), or creates a pulse below the threshold, the x-ray energy will be lost, resulting in a peak at energy $E = 662$ keV$-E_{Tl}$ where E_{Tl} is the Tl characteristic x-ray energy.

3. Backscatter Peak: A 180 ° Compton scatter occurs in the environment and the scattered gamma ray undergoes a photoelectric interaction in the TlBr detector. The backscatter peak for 662 keV gamma rays is 184 keV.

The overall single-pixel energy resolution was 0.94% FWHM at 662 keV and the peak-to-Compton ratio was 17.43. To date, these values are the best ever achieved on a large volume ($\geq$ 5 mm thick) TlBr detector when all single-pixel events are used (i.e. no pixel or depth selecting). The performance improved to 0.86% FWHM when events from the best pixel were selected (see Fig. 5.2a) and to 0.72% FWHM when events from the best pixel and best depth were selected (see Fig. 5.2b). In both cases, the two groups of Tl characteristic x-ray peaks were resolvable. These groups are 10 keV apart.

Fig. 5.3 shows the depth-dependent energy resolution in each pixel. Due to weighting potential effects, the resolution near the anode was poor in every pixel.

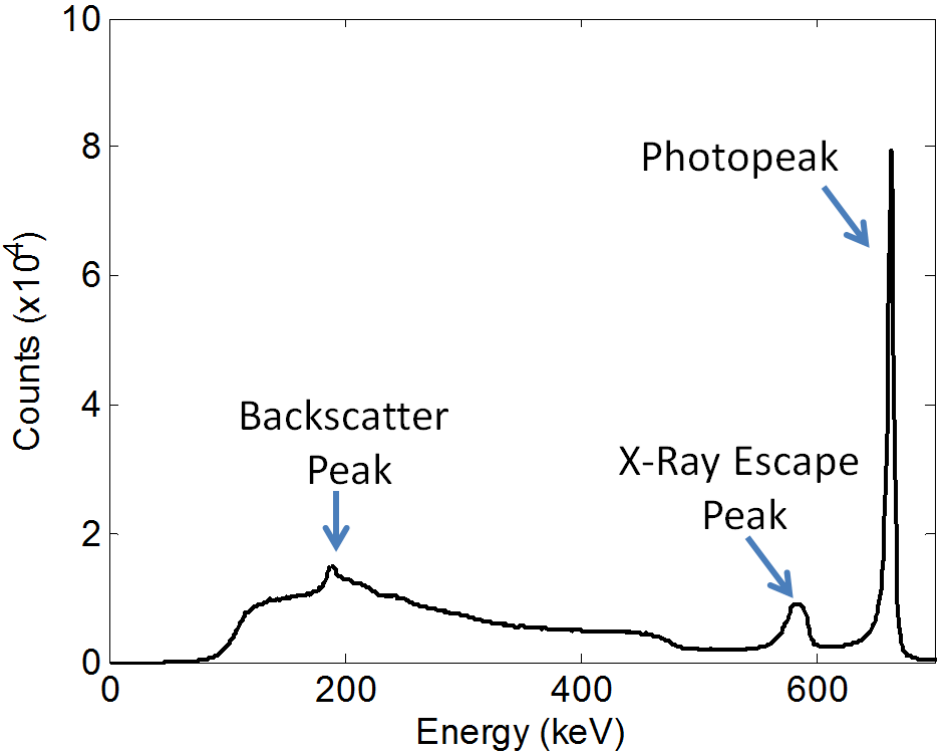

Figure 5.1: Single-pixel TlBr spectrum for detector 935-16B1L showing prominent features. The energy resolution was 0.94% FWHM at 662 keV and the peak-to-Compton ratio was 17.43.

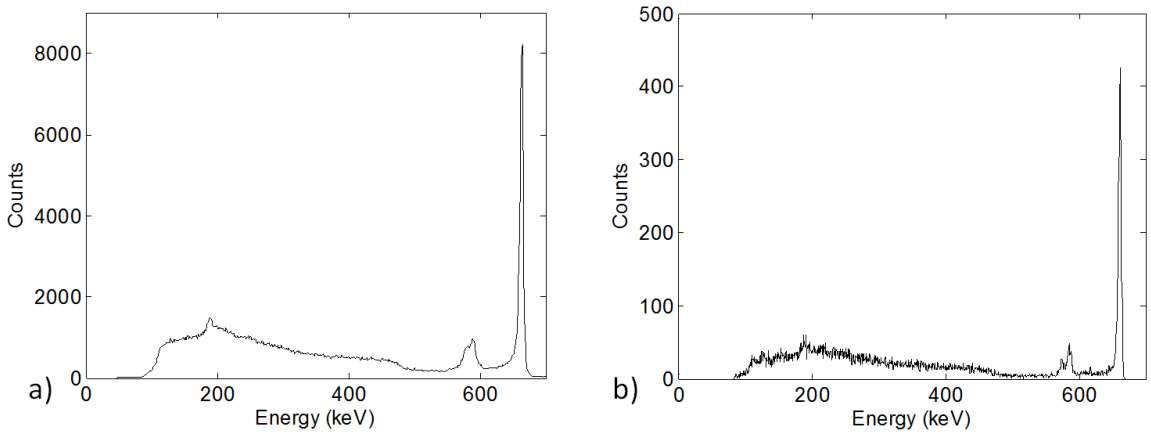

Figure 5.2: a) Pixel 4 (best pixel) spectrum showing 0.86% FWHM at 662 keV. b) Best depth (CAR = 10/15) spectrum showing 0.72% FWHM at 662 keV. The two groups of x-ray peaks were resolvable at this resolution.

However, the profile through the rest of the bulk was relatively uniform. The poor performance in pixel 9 was caused by a data acquisition error. This was verified by switching the readout channels. Detectors with poor bulk material (i.e. high non-uniform bulk trapping) show much worse resolution near the cathode, because cathode-side events travel through more of the bad material (see Sec. 5.1.3). In this case, uniform resolution at all depths indicated good bulk material.

Fig. 5.4 shows depth-dependent photopeak centroids in each pixel of detector 935-16B1L. In general, there are two processes that effect the shape of photopeak centroid profiles: weighting potential effects and trapping. Cathode-side events go through the full weighting potential while center events go through slightly less than the full weighting potential. Therefore, if only weighting potential effects are considered, photopeak centroid profiles would reach a maximum at the cathode surface and monotonically decrease towards the anode surface. Trapping has the opposite effect on photopeak centroid. Electron clouds from cathode-side events travel through more trapping sites as they move toward the anode, decreasing the total number of collected electrons and as a result, the signal amplitude. Therefore, if only trapping is considered, photopeak centroid profiles would reach a minimum at the cathode surface and increase towards the anode. In the real case, the two effects counteract each other and the resulting profile indicates which one is more dominate. In general, detectors with good bulk material exhibit high cathode-side photopeak amplitudes. As expected, the maximum photopeak centroid for detector 935-16B1L occurred at the cathode surface, indicating good bulk material.

The two bias method outlined in Sec. 3.3.4 was used to calculate the mobility-lifetime product for detector 935-16B1L: $\mu_e\tau_e = (6.5 \pm 0.8)$ x 10^{-3} cm^2/V. The correction factor to the two bias method (Eq. 4.3) was calculated to be $k = 0.896$ for a 5 mm thick detector with 1 mm pitch. Therefore, the corrected mobility-lifetime product for detector 935-16B1L was $\mu_e\tau_e = (5.8 \pm 0.7)$ x 10^{-3} cm^2/V. This $\mu_e\tau_e$ value

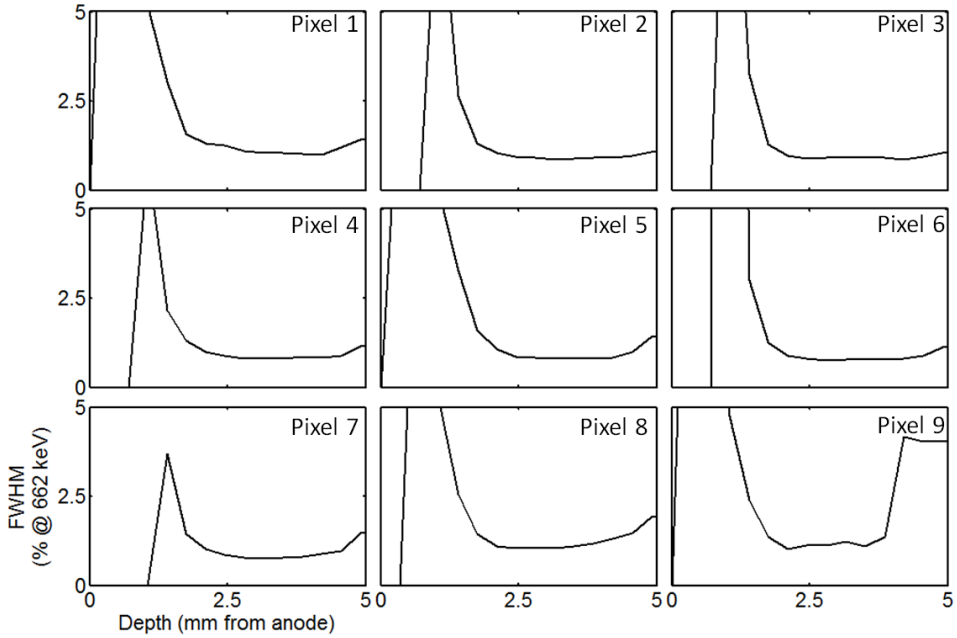

Figure 5.3: Pixel by pixel depth-dependent energy resolution for detector 935-16B1L.

is on the high-end for TlBr detectors (see Fig. 1.1), and consistent with good bulk material.

Fig. 5.5 shows the single-pixel performance for detector 935-16B1L. In general, there was very good uniformity across the device. Again, the fewer counts in pixel 9 was the result of poor data acquisition and was not indicative of true performance. The pixel uniformity, together with overall sub-1% FWHM at 662 keV energy resolution, indicated that surface properties were also good for detector 935-16B1L. Poor surface properties would result in some pixels achieving much worse performance compared to other pixels and very poor overall resolution. Table 5.1 summarizes the performance of other detectors that showed good bulk material and surface properties. In addition to good cathode-side performance and crystal uniformity, the detectors in Table 5.1 show high $\mu_e\tau_e$ and good overall energy resolution.

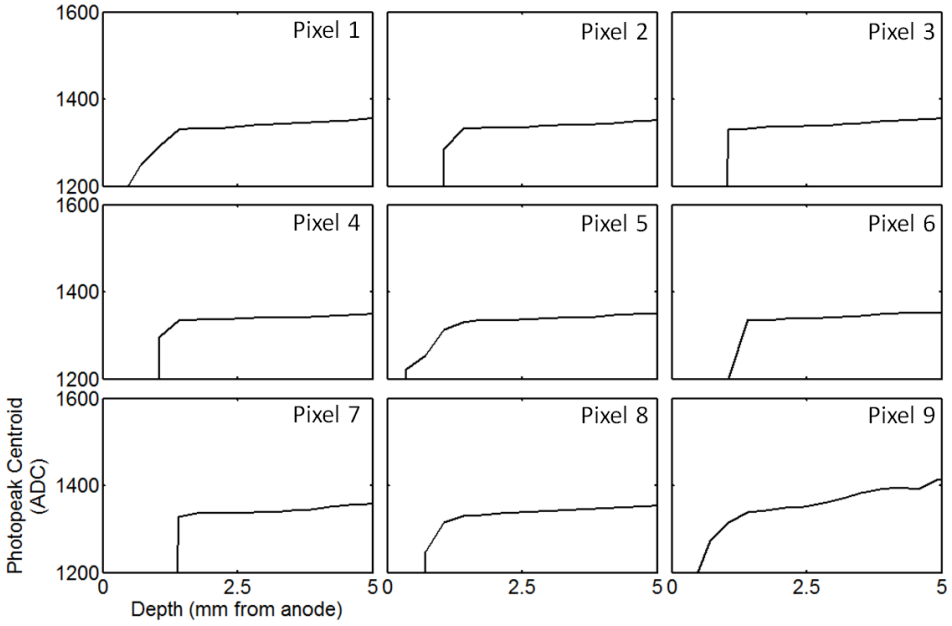

Figure 5.4: Pixel by pixel depth-dependent raw photopeak centroids for detector 935-16B1L.

Table 5.1: Performance of TlBr detectors with good bulk material and surface properties. The $\mu_e\tau_e$ was not calculated for detectors 58A3L or 935-16B1R because they were not operated at multiple biases.

Detector ID	Bias (V)	$\mu_e\tau_e$ (10^{-3}cm^2/V)	Overall Resolution (FWHM at 662 keV)	Best Pixel Resolution (FWHM at 662 keV)
58A3L	1000	-	1.36%	0.96%
935-16B1L	2000	5.8 ± 0.7	0.94%	0.86%
935-16B1R	1000	-	1.70%	1.30%
935-35AA1R	2000	16 ± 4	1.72%	1.22%
935-40BS4R	2000	4.0 ± 0.2	1.35%	1.09%

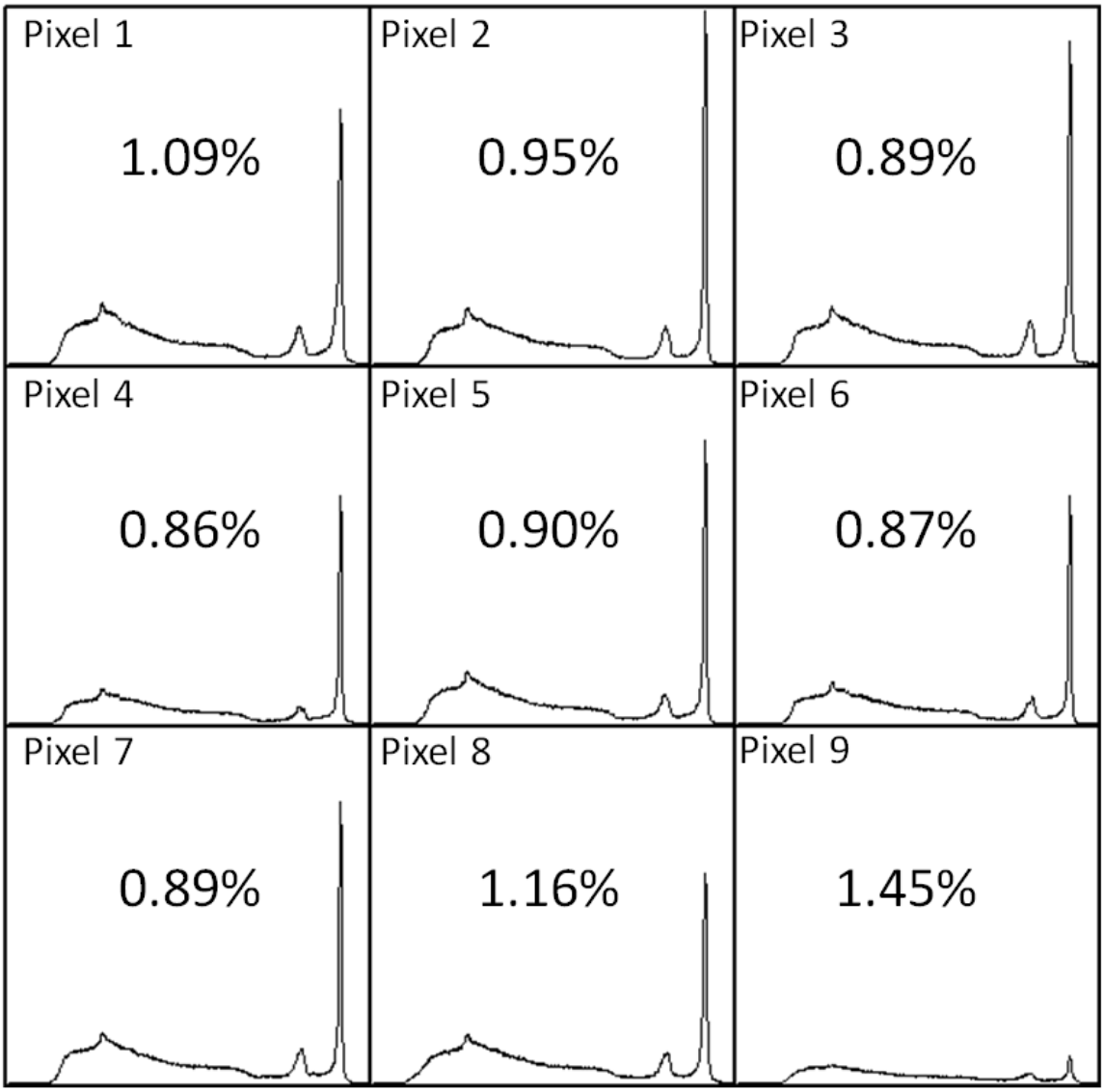

Figure 5.5: Pixel by pixel spectra for the same data shown in Fig. 5.1.

Table 5.2: Performance of TlBr detectors with good bulk material and poor surface properties. The $\mu_e\tau_e$ was not calculated for detector 70BA1R because it was not operated at multiple biases.

Detector ID	Bias (V)	$\mu_e\tau_e$ (10^{-3}cm^2/V)	Overall Resolution (FWHM at 662 keV)	Best Pixel Resolution (FWHM at 662 keV)
44B2L	1000	14 ± 5	2.20%	1.72%
70BA1R	1000	-	2.69%	1.17%
935-45AA2L	2000	6.3 ± 1.0	2.61%	2.02%

5.1.2 Good Bulk Material and Poor Contacts

Detectors with good bulk material and poor surface properties generally showed uniformly poor resolution at all depths because charge was lost at the detector surface, after drifting through the bulk. Therefore, all depths were affected by the same degree and the degradation was uniform. The poor surface could have been the result of bad contact between the electrode and TlBr, a dead layer at the TlBr surface, misalignment between the Au and Cr during metal deposition, or increased trapping from contact-to-bulk interactions.

Fig. 5.6 shows the depth-dependent energy resolution for detector 935-45AA2L, a typical detector with good bulk material but poor surface properties. Similar to detectors with good bulk material and good surface properties, the cathode side showed the near-best performance for most pixels. However, detectors showed uniformly poor energy resolution at all depths. Fig. 5.7 shows the photopeak centroids for the same detector. The cathode side had the largest centroid value, indicating low trapping. Table 5.2 lists other detectors with similar characteristics. The $\mu_e\tau_e$ values were generally very high, similar to the detectors listed in Table 5.1. However, the overall resolution was worse as a result of poor surfaces.

5.1.3 Poor Bulk Material

Detectors with poor bulk material generally fit into one of two categories: detectors with increased bulk trapping over time or detectors with high energy tailing as a result

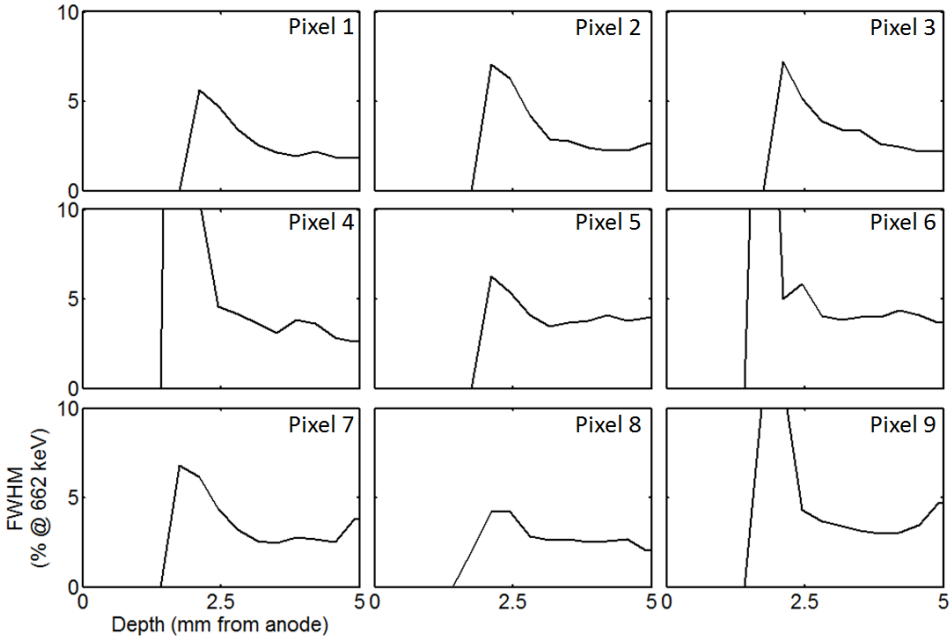

Figure 5.6: Pixel by pixel depth-dependent energy resolution for detector 935-45AA2L, a typical detector with good bulk properties but poor surface properties.

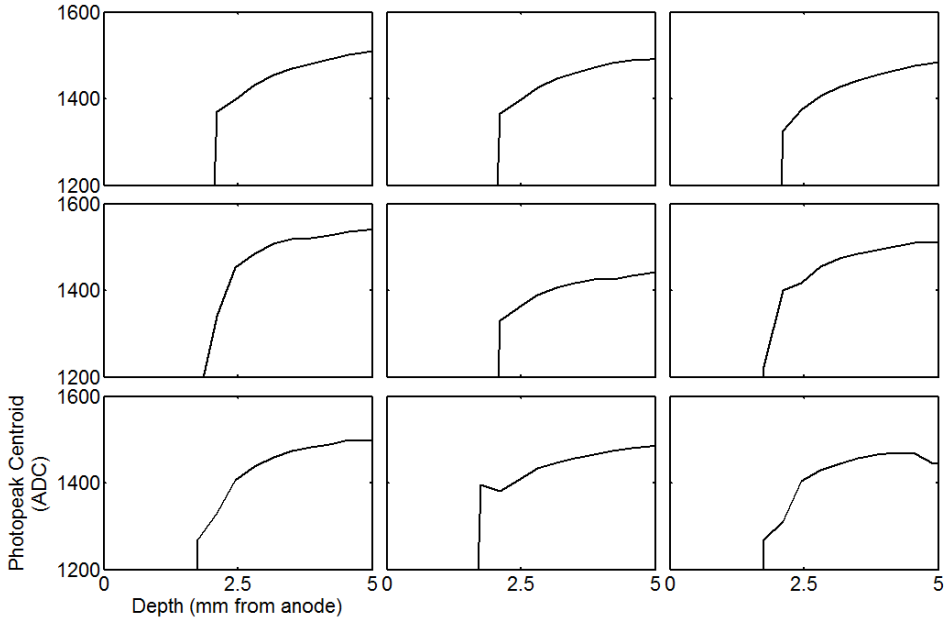

Figure 5.7: Pixel by pixel depth-dependent photopeak centroid for detector 935-45AA2L, a typical detector with good bulk properties but poor surface properties.

Table 5.3: TlBr performance for detectors with poor bulk material. Detector 102-BS2-2 was 10 mm thick. The $\mu_e\tau_e$ was not calculated for multiple detectors either because they were not operated at two different biases or because photopeak centroids were not obvious at low bias.

Detector ID	Bias (V)	$\mu_e\tau_e$ (10^{-3}cm^2/V)	Overall Resolution (FWHM at 662 keV)	Best Pixel Resolution (FWHM at 662 keV)
102-BS2-2	2200	-	2.81%	2.00%
44A12R	1000	-	2.35%	1.50%
45AL(R)	1500	2.9 ± 1.0	2.96%	2.15%
47AR(RR)	1000	-	2.78%	2.02%
57A2L	1000	-	2.4%	2.03%
70BA1R	1000	-	2.69%	1.17%
935-34AA1L	1000	-	1.64%	1.28%
935-34AA2L	1000	-	1.34%	1.15%
935-34AA2R	1800	3.4 ± 0.3	1.88%	1.56%
935-38AA1R	1000	-	1.8%	1.23%
935-43BA1R	1000	-	1.68%	1.43%
935-43BA2R	1000	-	3.04%	1.51%

of Auger recombination. Table 5.3 summarizes all detectors with poor bulk material. For both types, $\mu_e\tau_e$ tended to be low, indicating poor bulk material. Mobility-lifetime products were not calculated for all detectors because most were operated at only one bias. Because increased bulk trapping was time-dependent, some detectors showed good initial resolution, as shown in column 4 of Table 5.3. However, after one to four weeks, resolutions typically degraded to greater than 4% FWHM at 662 keV.

5.1.3.1 Increased Bulk Trapping

Fig. 5.8 shows the time-dependent energy resolution of detector 935-38AA1R. The performance initially degraded quickly and then slowed down after a week of continuous bias at $-20\,^{\circ}$C. Figs. 5.9 and 5.10 show depth-dependent photopeak centroids and energy resolution for different days of operation. As performance worsened, cathode-side photopeak centroids degraded more quickly than the rest of the bulk, indicating increased bulk trapping. Cathode-side-event electron clouds had more bulk to drift through, therefore, if the trapping increased, there was a higher

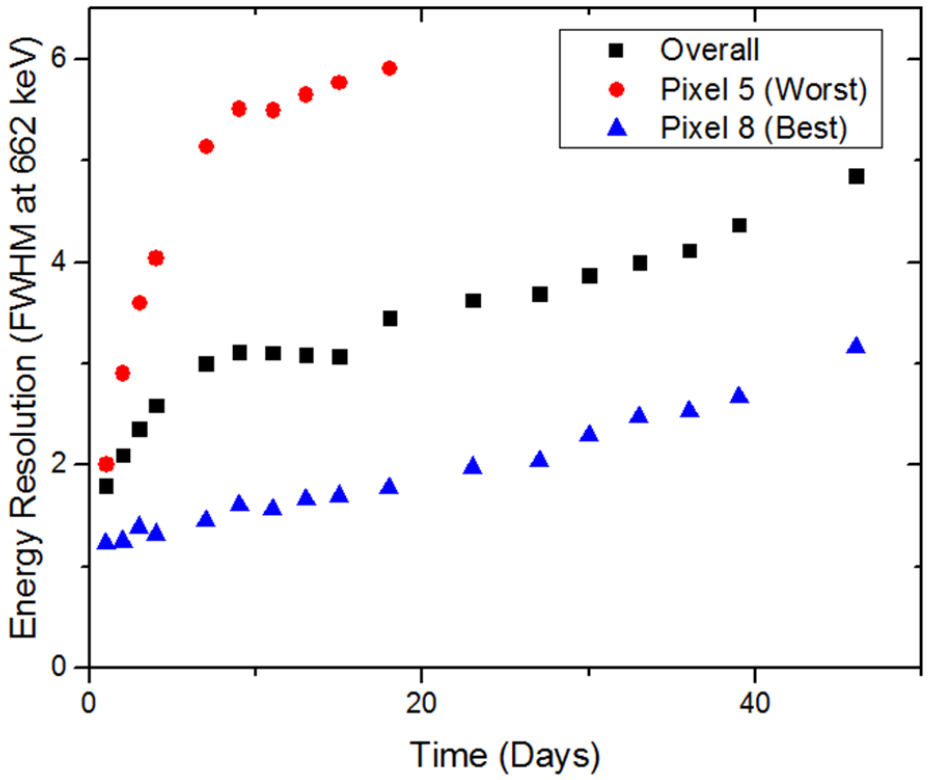

Figure 5.8: Energy resolution as a function of time for detector 935-38AA1R. The performance degradation is caused by increased bulk trapping.

probability that the further drifting electrons were trapped. This resulted in a more rapid decrease in cathode-side photopeak centroids. Similarly, for both days shown in Fig. 5.10, the cathode-side showed the poorest resolution, again a result of higher trapping.

5.1.3.2 High Energy Tailing from Auger Recombination

Some TlBr detectors showed high energy tailing after a week of continuous bias at $-20\,^{\circ}\mathrm{C}$. Fig. 5.11a shows the time-dependent energy resolution for detector 935-34AA2R, which showed high energy tailing around day 14. Fig. 5.11b shows 662 keV energy spectra for days 13 and 20. By day 20, a severe high energy tail developed. Fig. 5.11c shows sample cathode and anode waveforms for high energy tail events. Cathode waveforms were distributed in amplitude, indicating high energy tail events

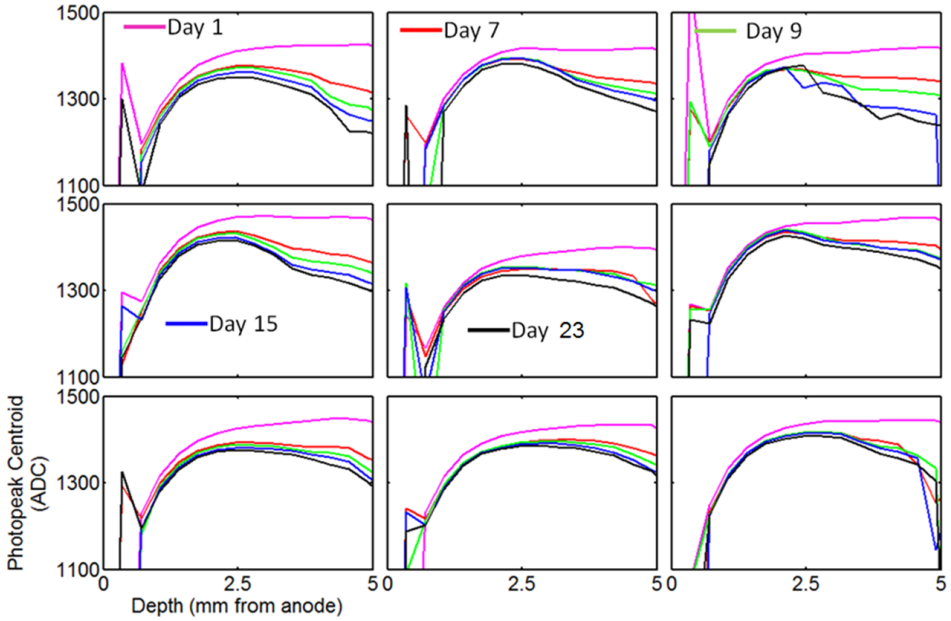

Figure 5.9: Depth-dependent photopeak centroids for detector 935-38AA1R. The faster degradation at the cathode indicates increased bulk trapping.

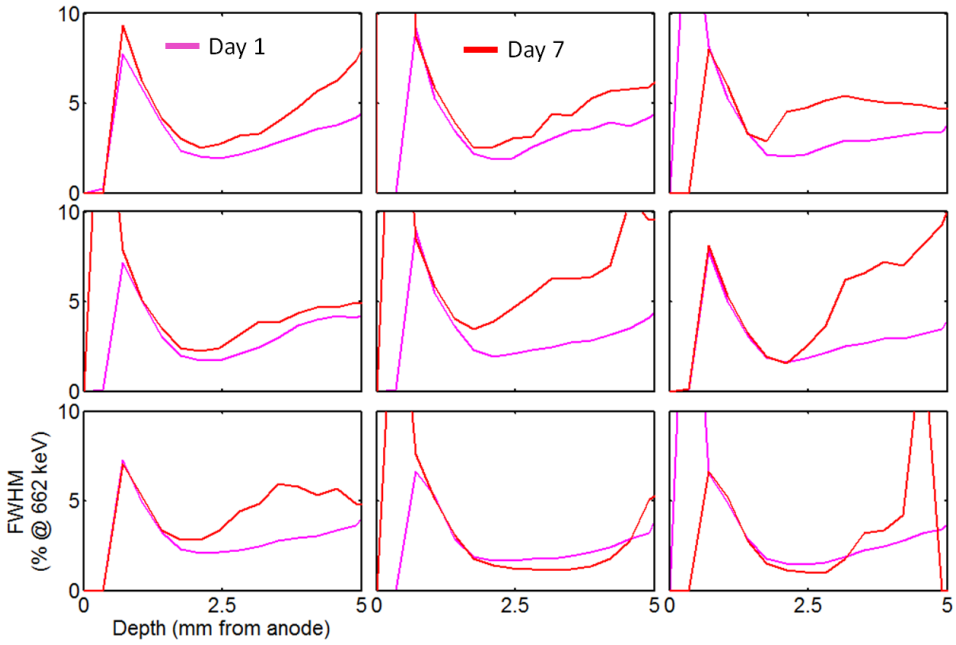

Figure 5.10: Depth-dependent energy resolution for detector 935-38AA1R. The faster degradation at the cathode indicates increased bulk trapping. The resolution was too poor at each depth to calculate the profiles after seven days.

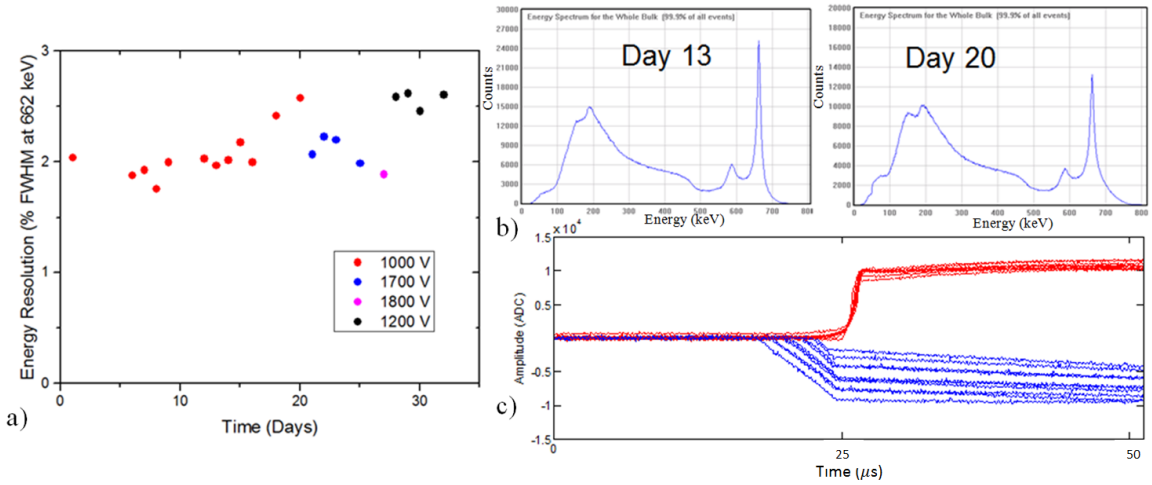

Figure 5.11: a) Resolution as a function of time for detector 935-34AA2R. b) Day 13 and Day 20 energy spectrum. By Day 20, a severe high energy tail was observed. c) Sample cathode (blue) and anode (red) waveforms for high energy tail events. The cathodes show distribution across all depths and the anode show a positive slope after electron collection which resulted in the high energy tail.

occurred at all depths. Anode waveforms showed a distinct slope after initial electron clouds were collected. This extra amplitude resulted in the high energy tail. Anode waveforms for normal photopeak events were flat, or in some cases, even had a slight negative slope from preamplifier decay, as shown in Fig. 3.10.

The ADC difference between the photopeak centroid and 5% of the photopeak maximum (see Fig. 5.12a) was used to quantify the magnitude of the high energy tail. This quantity, summed over all pixels, is shown in Fig. 5.12 as a function of time. The high energy tail got worse with both time and bias. When the detector bias was decreased from 1800 V to 1200 V after 26 days, the high energy tail also decreased. An LED was used to measure freed electron concentrations (proportional to the number of trapped electrons, see Sec. 3.3.3), when severe high energy tailing was first observed on day 14. Fig. 5.13 shows the freed electron concentration and average drift velocity which is proportional to the applied bias. The number of trapped electrons increased with the amount of high energy tailing.

High energy tailing was observed in HgI_2 detectors and thought to be the result of

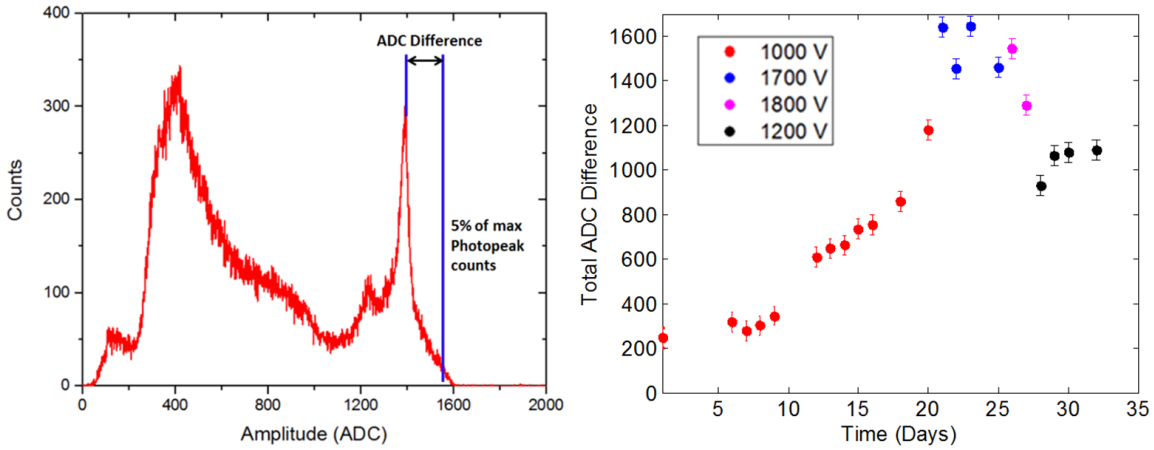

Figure 5.12: a) The high energy tailing was quantified as the ADC difference between the photopeak maximum and 5% of the photopeak maximum. b) Time-dependent change in the total ADC difference summed over all nine pixels.

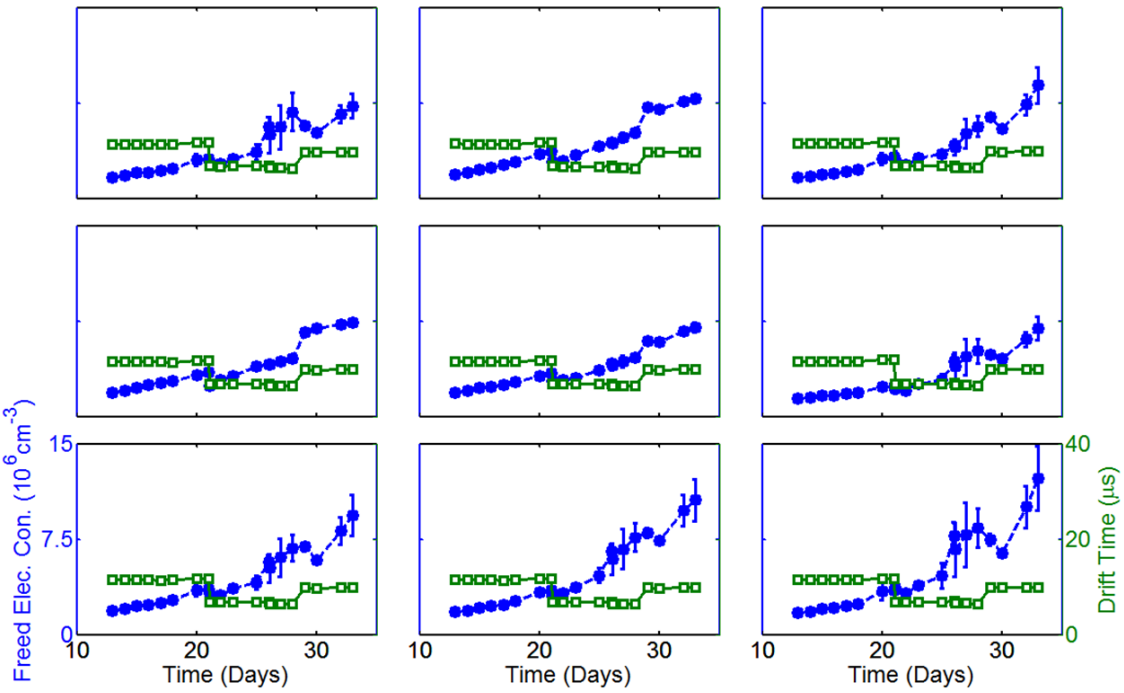

Figure 5.13: Freed electron concentration and average drift velocity. The number of trapped electrons increased when the high energy tail became more severe. The discontinuities in drift time was the result of bias change.

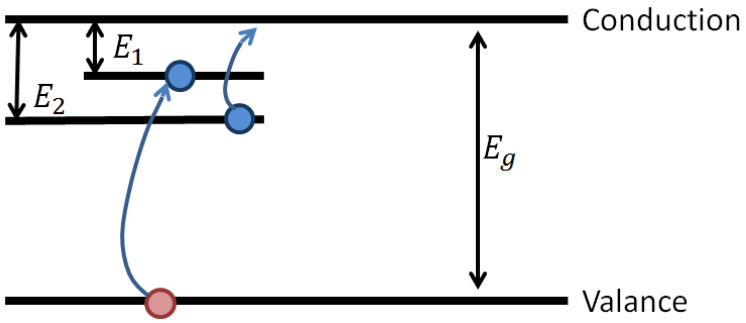

Figure 5.14: Schematic of Auger recombination.

Auger recombination [16]. Auger recombination occurs when a hole from the valance band interacts with a double trap site as shown in Fig. 5.14, copied from Ref. [16]. The hole recombines with one electron, releasing an amount of energy equal to the difference between the valance bad and trap site, $E_g - E_1$ in Fig. 5.14. The released energy frees the second trapped electron to the conduction band. Therefore, Auger recombination converts a hole to an electron. This extra charge ('extra' because pixelated anodes are only sensitive to elections) is observed after the initial cloud is collected because holes are much slower than electrons. The result is a positive anode slope and extra amplitude which causes high energy tailing. Figs. 5.11-5.13 are consistent with Auger recombination. If the number of trapped electrons increased, as shown in Fig. 5.13, then more Auger recombination sites were populated, increasing the chance of hole-to-electron conversion. The added signal from the electrons resulted in the increased high energy tail observed in Fig. 5.12.

Ref. [16] outlined alternative causes for high energy tailing, including severe trapping. In HgI_2, severe trapping was considered unlikely because raw photopeak centroids did not change significantly with bias. Under extreme trapping, photopeak centroids should increase at higher bias because a higher drift velocity reduces the trapping probability. Photopeak centroids in detector 935-34AA2R also showed no change at higher applied bias (see Fig. 5.15a).

The cathode waveforms shown in Fig. 5.11c show a significant 'hole' slope between

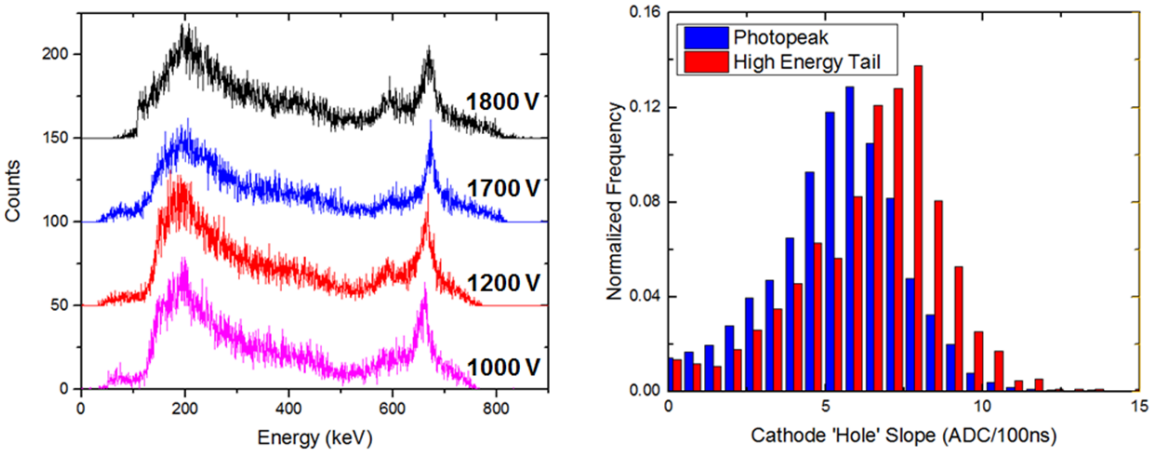

Figure 5.15: a) Raw spectrum in pixel 5 at different biases for detector 935-34AA2R. The insignificant change in photopeak centroid indicates that trapping is not severe and not the cause of the high energy tail. b) 'Hole' slope for photopeak and high energy tail events.

25 μs and 50 μs. If Auger recombination converted holes to electrons for high tail events, cathode slopes after electron collection would show a slight increase for high tail events because the electron mobility is significantly higher than the hole mobility. Fig. 5.15b compares 'hole' slopes between photopeak and high energy tail events. As expected with Auger recombination, average 'hole' slopes were slightly greater for high energy tail events.

If Auger recombination caused high energy tailing, then the counts in the high energy tail should be reduced if the number of populated Auger recombination sites is reduced. This was achieved on detector 935-43BA2R by shining above bandgap LED photons onto the detector. Fig. 5.16 shows the response of detector 935-43BA1R to a 3.1 eV LED. After the 'Before LED' measurement, the LED was turned on for two minutes. As a result of the photons, the high energy tail was reduced and the energy resolution improved. The above bandgap LED saturated the detector with moving electrons and holes. During illumination, holes recombined with trapped electrons and emptied Auger recombination sites. By the next day, the high energy tail returned because Auger sites eventually repopulated. The LED was used again

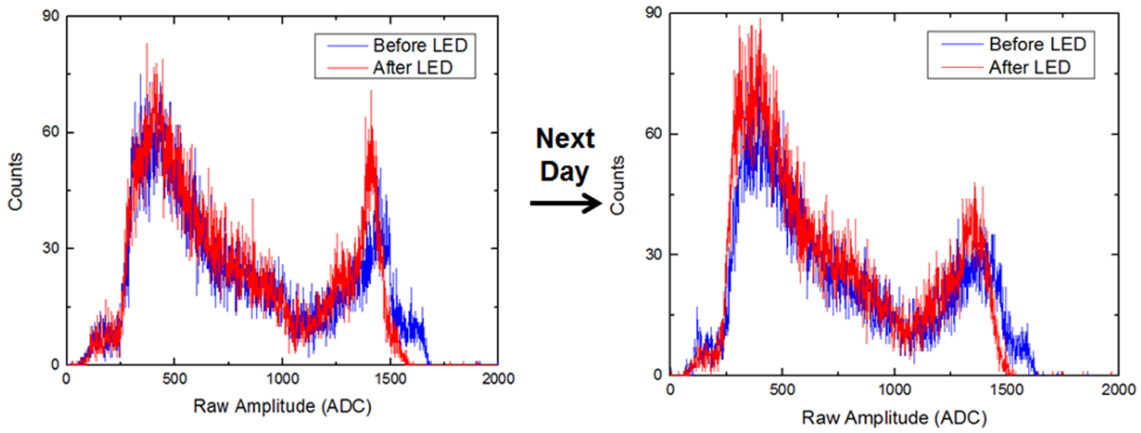

Figure 5.16: Detector 35-43BA2R response to above bandgap (3.1 eV) LED. The high energy tail was reduced because the LED generated holes reduce the number of populated Auger sites.

to show repeatability. These measurements are consistent with Auger recombination sites converting holes to electrons.

5.1.4 Verification of Depth Analysis for Detector Characterization

As shown in previous sections, depth-dependent signal analysis was a critical diagnostic tool. Two detectors were refabricated to verify the accuracy of these techniques. Detector 44B2L was characterized as having good bulk material but poor surface properties. Therefore, refabrication (removing electrodes, reprocessing surfaces, and reapplying electrodes while maintaining bulk material) should improve performance. Fig. 5.17 shows the single-pixel energy resolution for different bias and filter combinations before and after refabrication. A range of energy resolutions, based on bias and filter type, is typical for TlBr. Before refabrication (Jul. 2014, Jan. 2015, Sep. 2015), the detector never achieved better than 1.98% FWHM at 662 keV, regardless of applied bias or filter type. However, after refabrication (Mar. 2015), the detector always achieved better than 1.90% FWHM at 662 keV, likely a result of the improved surface conditions.

Detector 935-38AA1R was characterized as having poor bulk material from in-

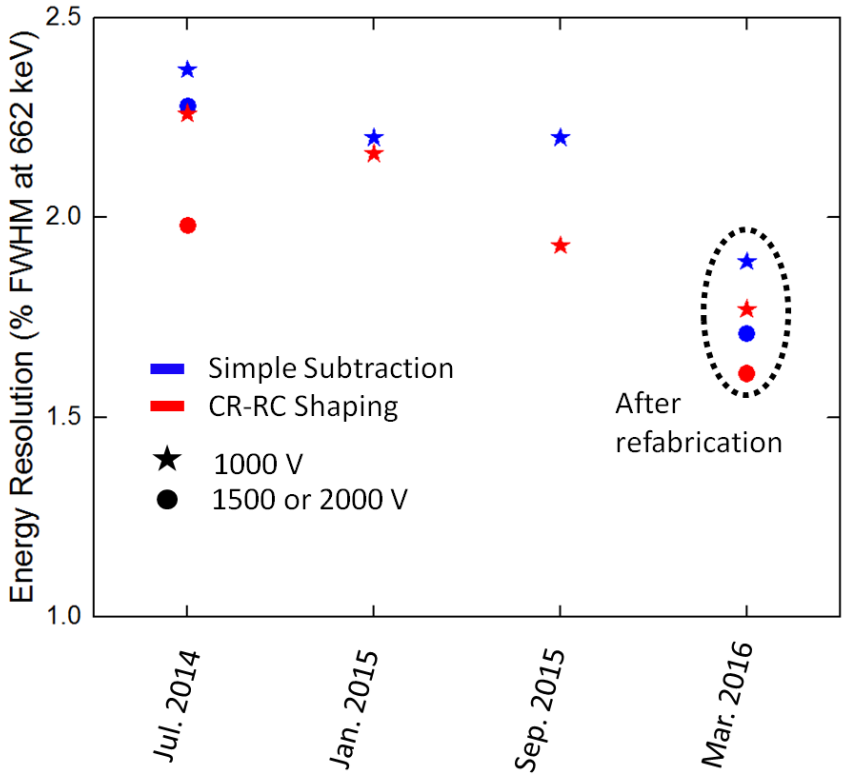

Figure 5.17: Energy resolution of detector 44B2L before and after refabrication under different applied bias and filter combinations.

creased bulk trapping. Therefore, refabrication should have no significant effect on the detector's time-dependent behavior because refabrication was done on the contacts and not the bulk. Fig. 5.18 shows the single-pixel energy resolution and $\mu_e\tau_e$ as a function of time. As predicted by depth analysis, the same degradation in energy resolution was observed. Depth-dependent analysis also predicted that degradation was due to increased bulk trapping. The $\mu_e\tau_e$ decreased during degradation (see in Fig. 5.18), independently verifying increased bulk trapping. Detector performance after refabrication for both 44B2L and 935-38AA1R was consistent with predictions from depth-dependent signal analysis.

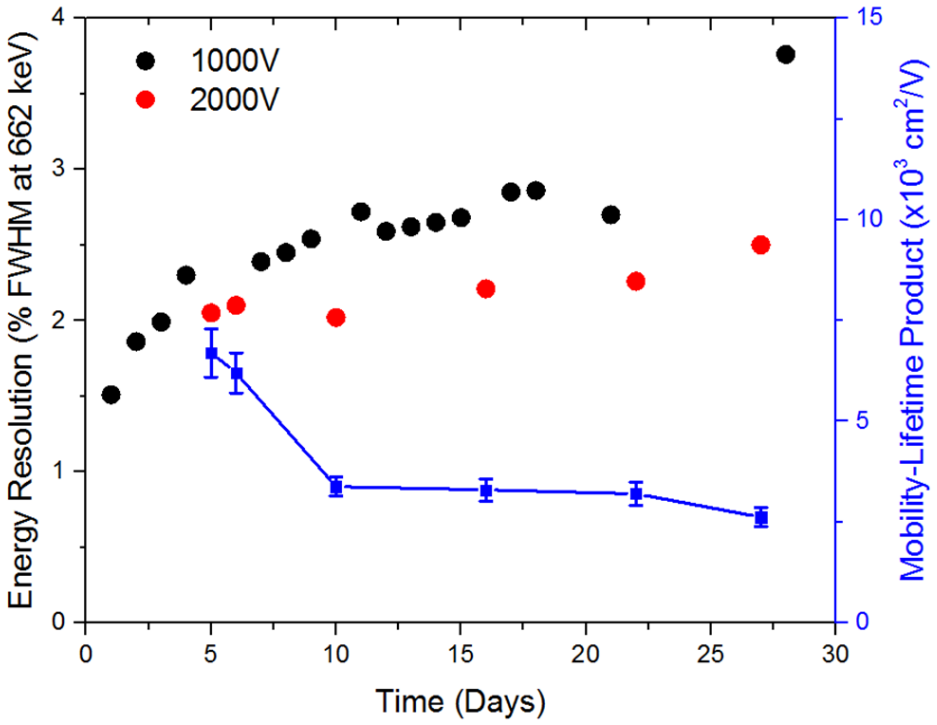

Figure 5.18: Energy resolution (red and black points) and $\mu_e\tau_e$ (blue points) as a function of time for detector 935-38AA1R after electrode refabrication.

5.2 Depth Reconstruction for High-Hole Mobility Detectors

As discussed in Sec. 3.3.2, some TlBr detectors have high hole mobility which can obscure depth reconstruction from cathode-to-anode ratio (CAR). Advanced digital processing methods were developed to accurately reconstruct interaction depths for detectors with high hole mobility. Methods were developed for low, but significant, hole mobility detectors ($\mu_h/\mu_e \sim 0.05$) and for high hole mobility detectors ($\mu_h/\mu_e \sim 0.15$).

For all algorithms, a collimator was used to expose a single detector depth to a fan-beam of gamma rays. Fig. 5.19 shows a typical count distribution for each collimator depth. Vertical lines above each distribution represent the true depth, known from the collimator position. The calculated centroid of each distribution was used as the reconstructed depth and the FWHM was used as the depth resolution.

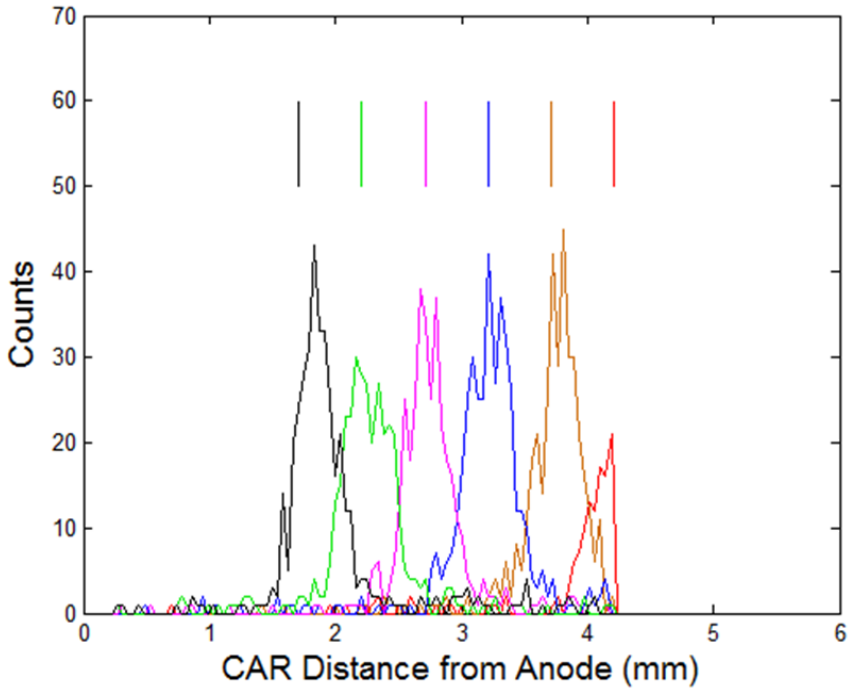

Figure 5.19: Count distribution for each collimator position. Vertical lines represent true depths, known from the collimator positions.

5.2.1 Low Hole Mobility Depth Reconstruction

Fig. 5.20 shows calculated depths from the CAR as a function of true depths, known from the collimator position, with and without the single-slope hole correction algorithm described in Sec. 3.3.2. When no hole correction was applied, interaction depths were systematically overestimated as a result of holes contributing extra amplitude to the cathode signal. When hole contributions were removed, calculated depths equaled true depths at all locations inside the bulk. The best-fit line for the corrected data had a slope of 0.97 ± 0.04 and an intercept of 0.13 ± 0.13, consistent with excellent depth reconstruction.

5.2.2 High Hole Mobility Depth Reconstruction

Fig. 5.21 shows reconstructed depths as a function of the true depths for the Newton-Raphson (NR) fitting, NR-Timing hybrid (NRT), and timing only methods.

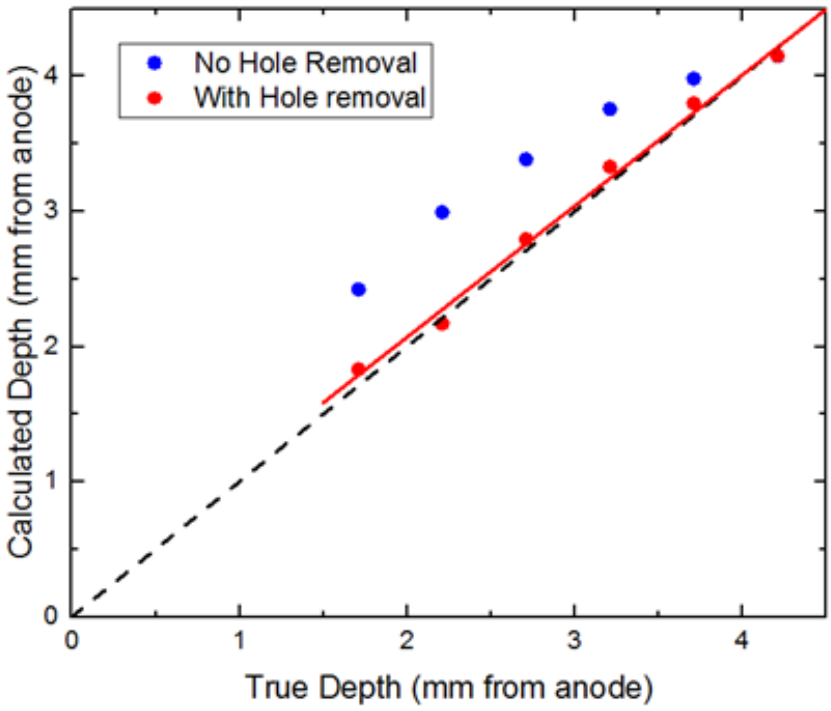

Figure 5.20: Reconstructed depth as a function of true depth with (red) and without (blue) the hole correction.

When the NR algorithm was applied, degenerate waveforms described in Sec. 3.3.2 caused poor depth reconstruction near the cathode. Again, this occurred for all events in which the hole collection time was less than the electron collection time.

The timing method also reconstructed the depths relatively accurately through most of the bulk. The constant offset in reconstructed depths when the timing algorithm was used could be removed through calibration. However, the relative depth uncertainty (or depth resolution) was worse compared to the NR and NRT methods. The relative depth uncertainty (relative because the collimator had a finite width) for the timing and NRT methods were 600 μm and 450 μm, respectively. Low depth uncertainty is critical for high performing imagers because the uncertainty in the interaction depth is the largest contributer to the source-direction uncertainty for 662 keV gamma rays [51].

The best method to reconstruct interaction depth in detectors with high hole mo-

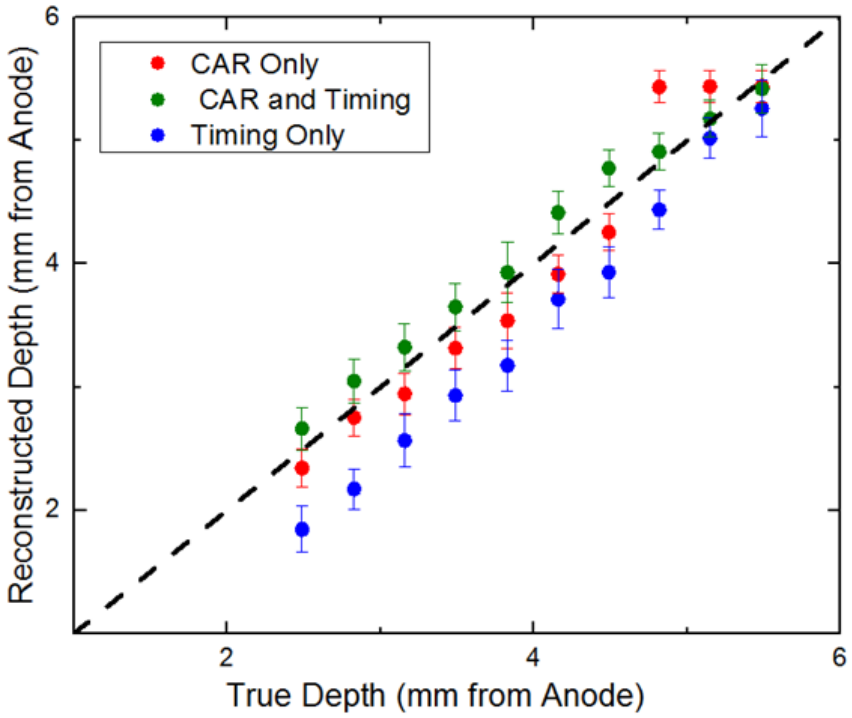

Figure 5.21: Reconstructed depth as a function of true depth for different hole removal algorithms. The NRT method showed the best performance.

bility was the NRT method. Low depth uncertainty was maintained and interaction locations were accurately reconstructed at all depths. The absolute depth resolution was approximately 300-350 μm. This measurement was done by decreasing the collimator width and counting for an extended time at a single depth.

Hole-removal algorithms were developed to maintain high CAR depth-resolution. The theoretical depth resolution for CAR methods can be estimated from error propagation:

$$CAR = \frac{V_C}{V_A}$$

$$\left(\frac{\sigma_{CAR}}{V_C/V_A}\right)^2 = \left(\frac{\sigma_C}{V_C}\right)^2 + \left(\frac{\sigma_A}{V_A}\right)^2$$

where V_C and V_A are the cathode and anode signal amplitudes and σ_C and σ_A are

the signal noises. For pixelated detectors, $\sigma_C >> \sigma_A$ and $V_C \leq V_A$. Therefore:

$$\left(\frac{\sigma_{CAR}}{V_C/V_A}\right)^2 \approx \left(\frac{\sigma_C}{V_C}\right)^2$$

$$\sigma_{CAR} = \frac{\sigma_C}{V_A} \tag{5.1}$$

Note that in pixelated, and all single polarity charge sensing detectors, depth resolution, σ_{CAR}, is independent of interaction depth (because V_A is independent of interaction depth) and only depends on cathode noise. Timing methods use the difference of cathode and anode trigger times to calculate interaction depth. Therefore, both σ_A and σ_C contribute to the uncertainty, and the overall depth resolution is worse compared to CAR methods. This was shown experimentally above.

5.3 Conditioning Phase in Cooled Detectors

Some TlBr detectors undergo a conditioning phase at $-20\,^{\circ}$C which is characterized by improved energy resolution and drift velocity over time during continuous bias. For example, Fig. 5.22 shows the pixel-by-pixel performance of detector 58A3L at $-20\,^{\circ}$C. After four days of applied bias, the resolution improved dramatically in all pixels. Fig. 5.23 shows drift velocity profiles for the same detector after one and twelve days of continuous bias. The average velocity increased and the profile became more uniform during conditioning.

Using new methods described in Secs. 3.3.1.3 and 3.3.3, this work concludes that the increased drift velocity was the result of improved electric fields caused by trapped charge migration. Ultimately, more stable and uniform drift velocities caused improved resolution.

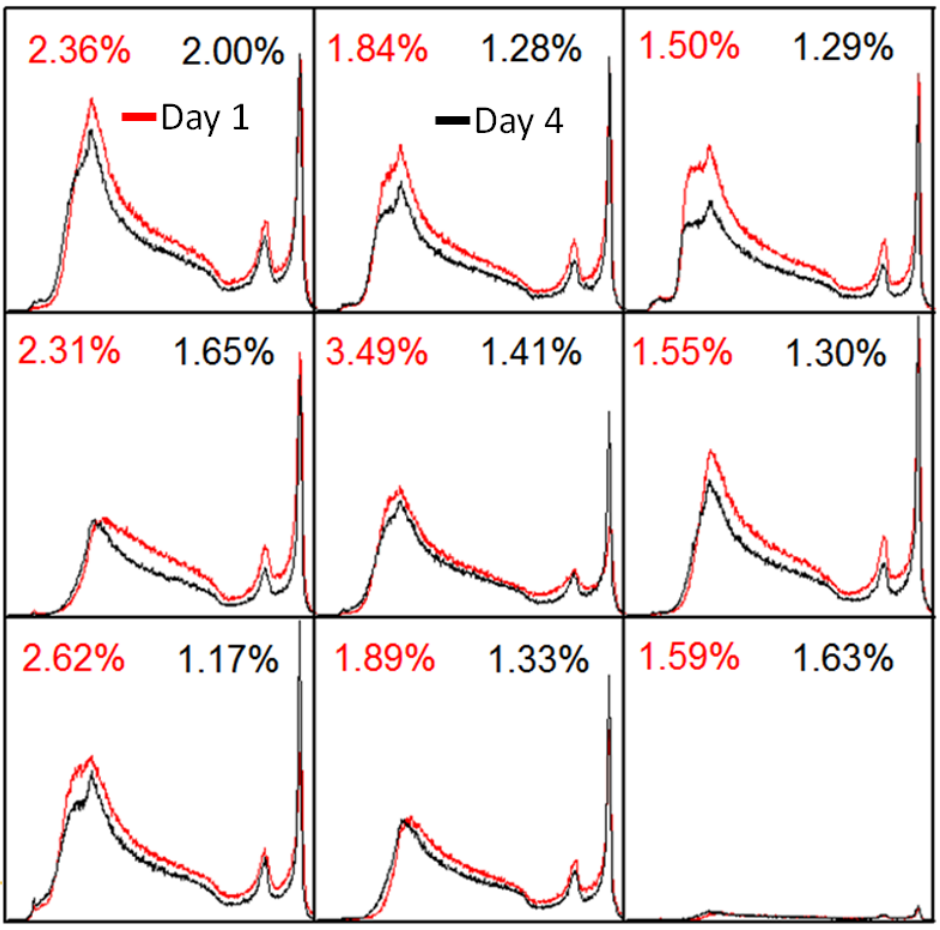

Figure 5.22: Pixel-by-pixel performance of detector 58A3L after one (red) and four (black) days of applied bias. Also shown is the energy resolution at 662 keV.

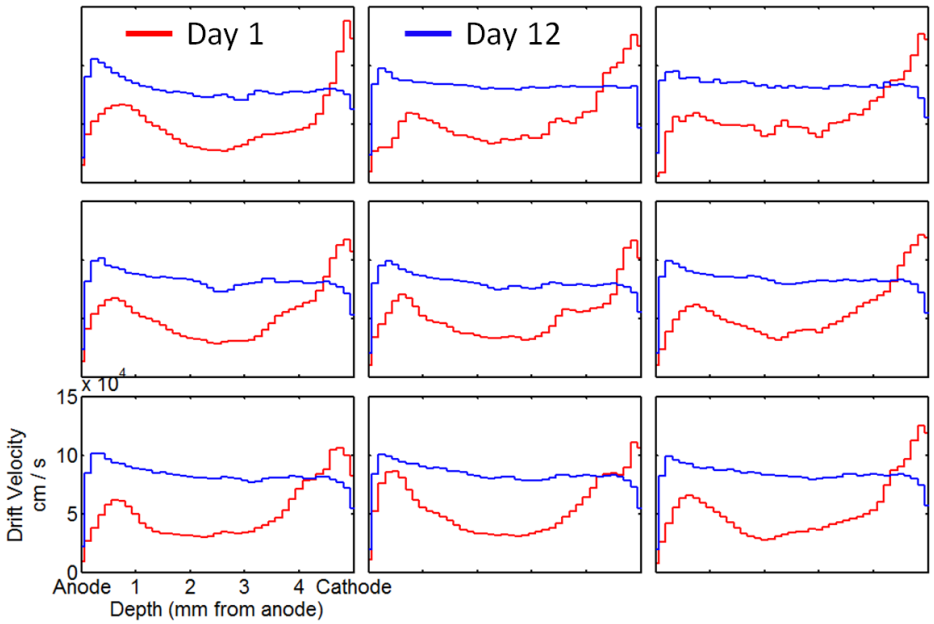

Figure 5.23: Pixel-by-pixel drift velocity profiles after one (red) and twelve (blue) days of applied bias.

5.3.1 Electric Field Stabilization

Previous work has shown that electron drift velocity increases and becomes more uniform during the conditioning phase, as shown in Fig. 5.23 [32, 46]. However, it was unclear whether the improvement was due to a stronger effective electric field or higher mobility: $v_e = E * \mu_e$. Note that while the spatial average electric field is set by the detector bias, there is no such constraint on the average drift velocity: $\langle v_e \rangle = d/t_d$, where d is the detector thickness and t_d is the cathode-side drift time. The average drift velocity can increase by more than 2x when the electric field becomes more uniform. Therefore, it is useful to define the average effective electric field:

$$E_{eff} = \frac{\langle v_e \rangle}{\mu_e}. \tag{5.2}$$

E_{eff} is not constrained by the detector bias and will increase when the true electric field becomes more uniform. For example, consider the two electric field profiles shown in Fig. 5.24. In both cases, the spacial average electric field is 2000 V/cm, as

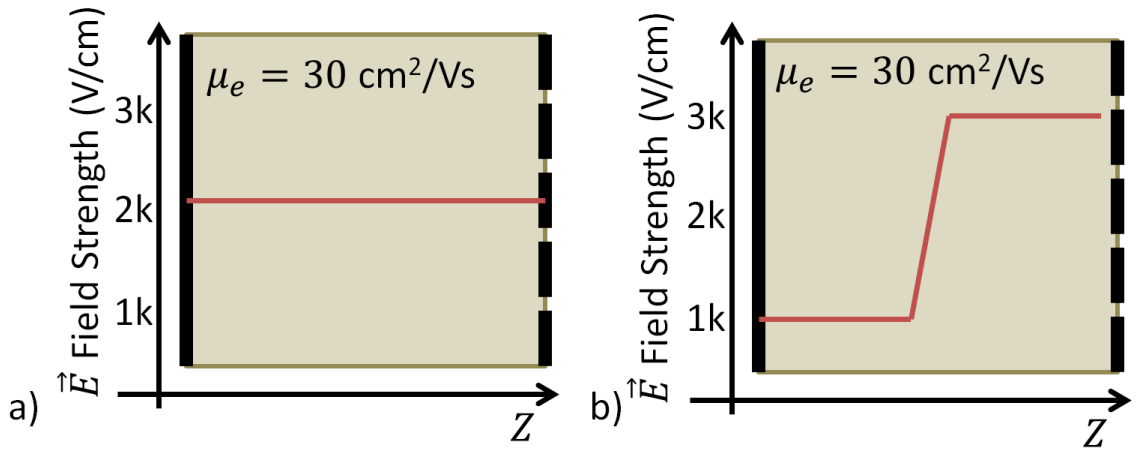

Figure 5.24: a) Uniform electric field and b) non-uniform electric field. Both profiles have the same spacial average electric field, however, the average effective electric field is greater in a) compared to b). Note that the profile shown in b) is unrealistic for TlBr detectors and was only used to show the effect of a non-uniform electric field on the drift time.

dictated by the 1000 V applied bias across the 5 mm thick detector. If the electron mobility is assumed to be 30 cm^2/Vs, a typical value for TlBr, then the drift velocity for the electric field shown in Fig. 5.24a is 6 x 10^5 cm/s and the drift time (t_d) is 8.33 μs. For the non-uniform electric field shown in Fig. 5.24b, the drift velocity is 3 x 10^5 cm/s for the first half of the detector and 9 x 10^5 cm/s for the second half of the detector. Therefore, the total drift times across the fist and second halves of the detector are:

$$t_d = t_1 + t_2 = \frac{0.25\ cm}{3x10^5\ cm/s} + \frac{0.25\ cm}{9x10^5\ cm/s} = 11\ \mu s. \tag{5.3}$$

In both cases, the spacial average electric field is the same. However, the drift time, and therefore the average effective electric field, is lower for the non-uniform profile.

Detector 935-35AA1L had sufficient hole mobility to measure both electron and hole drift velocities simultaneously. Fig. 5.25 shows the hole drift velocity as a function of the electron drift velocity during the conditioning phase of detector 935-35AA1L.

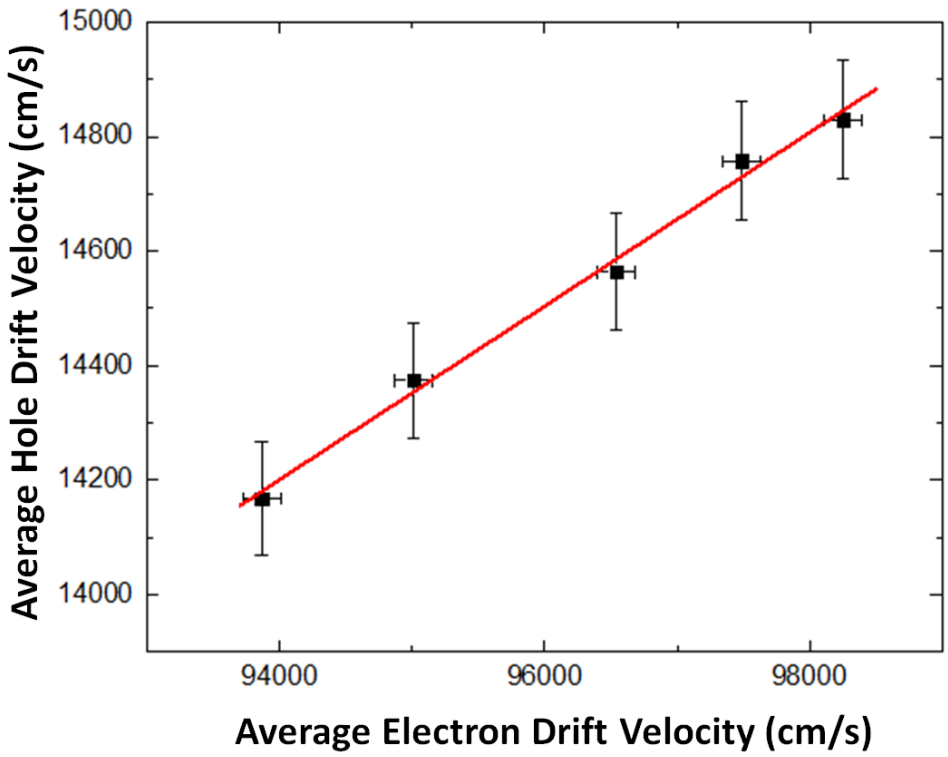

Figure 5.25: Hole drift velocity as a function of the electron drift velocity for detector 935-35AA1L at 2000 V. The least squares line of best fit has the following parameters: Slope = 0.151 ± 0.007, Intercept = 60 ± 700, $r^2 = 0.991$.

The linearity in Fig. 5.25 indicates that either the mobilities were increasing by the same percentage or the effective electric field was increasing. Because mobilities of holes and electrons are governed by valence and conduction band properties respectively, it is more likely that the effective electric field was increasing, resulting in the simultaneous improvement of both electron and hole drift velocities. Additionally, the linear best fit-line has an intercept consistent with zero which is expected if the change was caused by the electric field: zero electric field results in zero drift velocity. However, no such constraint exists if the mobilities were changing. The slope of the least squares best-fit line in Fig. 5.25 gives the mobility ratio: $m = \mu_h \ / \ \mu_e = 0.15$.

5.3.2 Spectroscopy, Active Volume, and the Role of Trapped Electrons

Each TlBr detector conditioned as part of this work demonstrated unique behavior. As a result, two detectors were studied using slightly different procedures in order to fully quantify the conditioning phase.

5.3.2.1 Detector 935-16B1L

Detector 935-16B1L was conditioned at $-20\,^{\circ}\mathrm{C}$ in April 2014. It was subsequently biased down, warmed up to room-temperature, stored in a desiccator for three months, and reconditioned at $-20\,^{\circ}\mathrm{C}$ in July 2014. The time-dependent energy resolution for both tests is shown in Fig. 5.26. Each twenty-four hour dataset had more than four hundred and fifty thousand photopeak counts and as a result, the FWHM uncertainty was negligible. In both measurements, the energy resolution improved dramatically over the first five days, indicating that whatever mechanism caused the improvement, relaxed when the detector was stored without bias.

The photopeak centroid, proportional to charge collection efficiency, as a function of time during days one and eight is shown in Fig. 5.27a. Based on energy resolution and number of photopeak counts, centroid uncertainties were on the order of 0.03% and unobservable on the figure. On day one, photopeak centroids were unstable, artificially degrading energy resolution. On day eight, centroids were stable and good energy resolution was observed.

In contrast to detector 935-35AA1L, detector 935-16B1L did not have sufficient hole transport and the hole drift velocity was not measured. Over the first six days of both the April 2014 and July 2014 conditionings, average electron drift velocities improved from less than 2 x 10^4 cm/s (minimum measurable drift time given the sampling window) to $\sim$ 7.5 x 10^4 cm/s. Based on results from Fig. 5.25, a different detector with high hole mobility, it is likely here too that the electron drift velocity increase was caused by an increase in the effective electric field as opposed to the

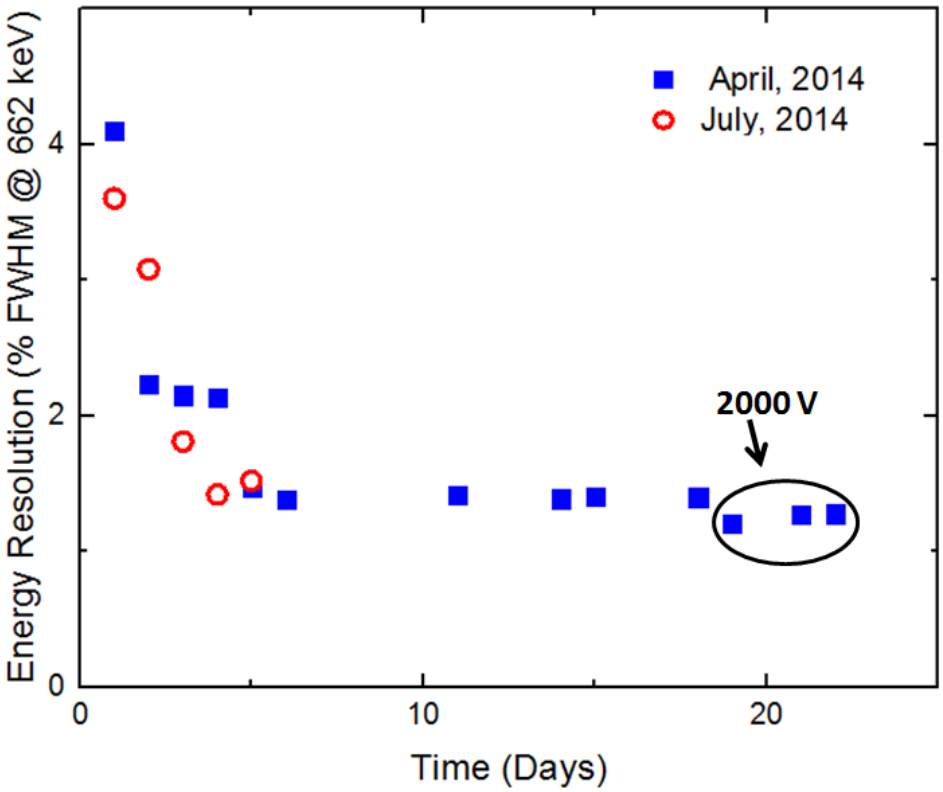

Figure 5.26: Time-dependent energy resolution for detector 935-16B1L during two different conditionings. Except where indicated, the bias was 1000 V.

mobility.

Fig. 5.27b shows the photopeak counts, calculated as the raw anode amplitude between 1200 ADC and 1500 ADC, as a function of depth from CAR, over the first six days of the April 2014 conditioning. On the first day, photopeak counts were recorded only within about 2 mm of the anode surface, indicating that the internal electric field was very weak in the center of the detector. Electron clouds from both cathode-side and center events had to travel through the weak electric field in the center of the detector before being collected by the anode. Therefore, even though the electric field was likely high near the cathode in order to preserve the average electric field set by the cathode bias, no photopeak events were observed near the cathode. The low electric field in the center of the detector caused increased trapping and poor charge collection efficiency for all events which had to travel through the center, including cathode-side events. The high trapping removed photoelectric interactions from the photopeak range defined above: 1200 to 1500 ADC. As the device conditioned and the electric field improved, the detector fraction with poor charge-collection-efficiency decreased from ∼60% on day one, to ∼50% on day 2, to ∼30% on day 3, and to ∼5% on day 4. The energy resolution showed a sharp improvement between day four and day five (see solid squares in Fig. 5.26) corresponding to when the poor region disappeared. This was likely because, for good detectors, cathode-sides typically shows the best energy resolution. Therefore, the best performance was observed when the entire detector (i.e. cathode side) was active.

Due to slow cathode rise times, the exact electric field profile could not be measured during the first three days. However, by day four, entire cathode waveforms were collected in the sampling window and drift velocity profiles were calculated using the method described in Section 3.3.1.3. Using the known 2000 V/cm average electric field to normalize the profile, the depth-dependent electric field was estimated from drift velocity profiles for day four, as shown in Fig. 5.28. Photopeak events were

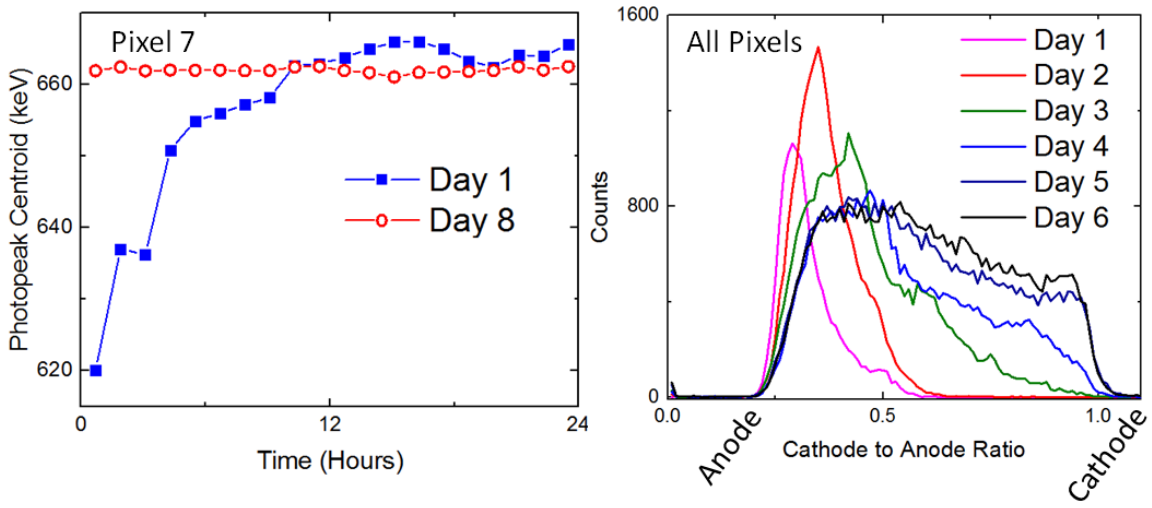

Figure 5.27: a) Photopeak centroid as a function of time over day one (solid squares) and day eight (open circles). b) Total photopeak counts as a function of depth during conditioning.

observed at all depths for the first time on day four (see Fig. 5.27b). Therefore, the electric field in the center must have been greater than a critical value required to observe photopeak events at all depths in detector 935-16B1L. The minimum electric field on day four was roughly 1000 V/cm, which provides an upper bound for this critical field. Prior to day 4, the electric field in the center of the detector must have been below 1000 V/cm because photopeak counts were not recorded at all depths.

Although cathode side drift times were too slow to calculate drift velocity profiles during the first three days, Figs. 5.27b and 5.28 were used to create a cartoon of the expected electric field during all parts of the conditioning phase (see Fig. 5.29). The horizontal dotted line shows the critical electric field at 1000 V/cm that must be achieved in the center of the detector in order to observe photopeak events at all depths.

5.3.2.2 Detector 44B2L

Detector 44B2L was also conditioned two separate times to verify relaxation of conditioning mechanisms. Fig. 5.30 shows the time-dependent energy resolution for

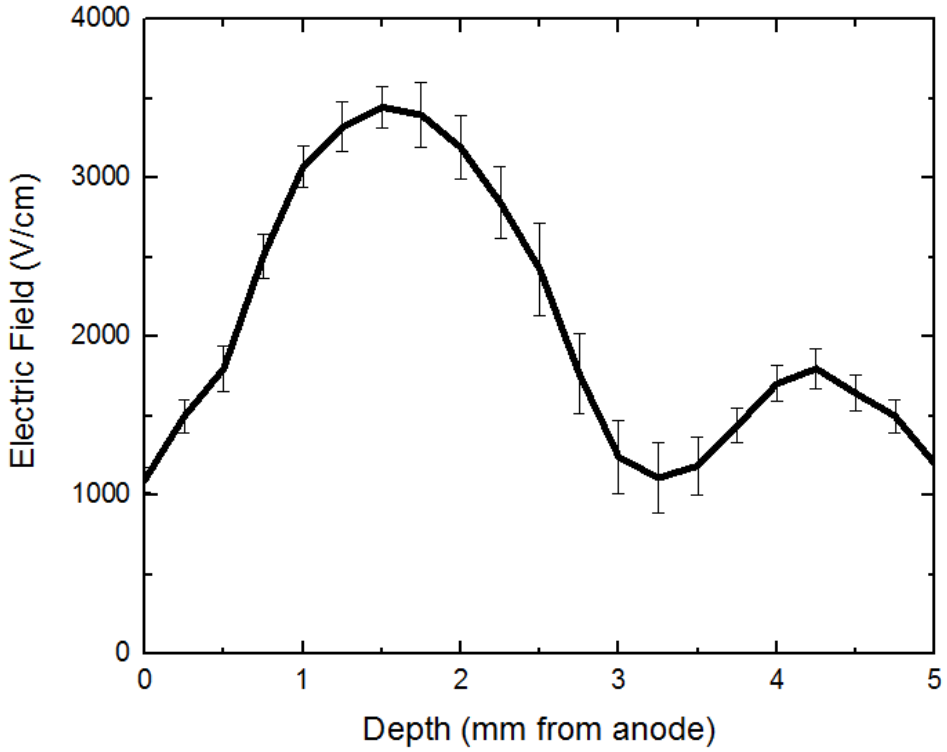

Figure 5.28: Electric field profile for the fourth day of the April 2014 conditioning of detector 935-16B1L. The minimum electric field value sets an upper limit on the critical electric field required to observe photopeak events at all depths.

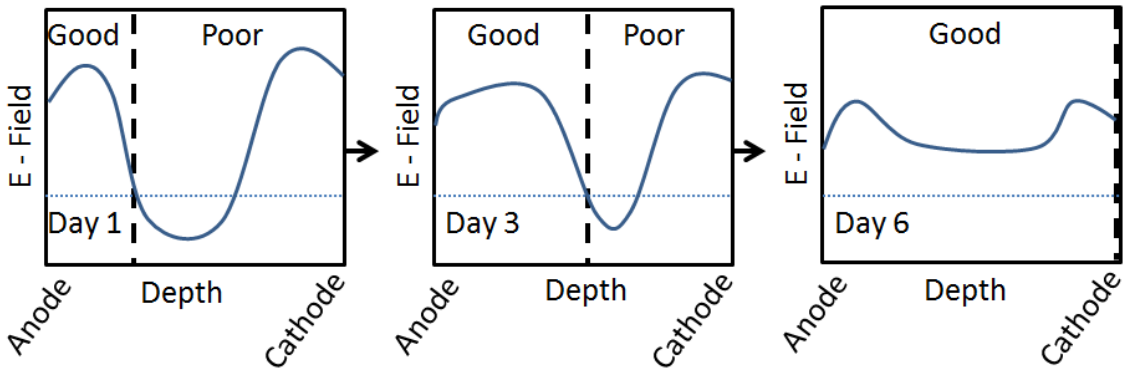

Figure 5.29: Electric field profile cartoon in detector 935-16B1L during the conditioning phase. The horizontal dotted line represents a critical electric field that must be achieved to observe photopeak counts. The vertical dashed line separates the good region (observable photopeak counts) from the poor region (no observable photopeak counts).

the July 2014 and January 2015 measurements. Each twenty-four hour spectrum had more than four hundred and eighty thousand photopeak counts so FWHM uncertainties were negligible. During the January 2015 conditioning, the bias was increased from 750 V to 1000 V after six days. When the bias was 750 V, the January 2015 improvement was slower compared to the July 2014 improvement. After the bias was increased, the conditioning in January 2015 was faster compared to July 2014, indicating that a higher bias can speed up the conditioning phase.

Before each twenty-four-hour measurement during the January 2015 conditioning, an LED was used to illuminate the detector and the concentration of freed electrons from the LED photons was estimated using Eq. 3.6. Fig. 5.31 shows freed electron concentrations and cathode-side-event electron drift-times for each pixel during the January 2015 conditioning phase. Uncertainties were on the order of 4 to 6% and are not visible for some points. The freed electron concentration was the number of detrapped electrons as a result of exactly 6 mA of LED current. The resulting number of photons was well below what was required to free all trapped electrons. Therefore, freed electron concentrations shown in Fig. 5.31 were proportional, but not equal, to the total number of trapped electrons. The proportionality constant was maintained from day to day by using the same LED current (number of photons). As expected, there was a discontinuity in the day 7 drift-times (open squares in Fig. 5.31) when the bias was increased from 750 V to 1000 V. The freed electron concentrations are independent of electric field, therefore, no discontinuity was observed in the solid circles in Fig. 5.31.

The freed electron concentration and drift time, an inverse measure of the effective electric field, decreased continuously in all pixels to less than a fifth of their original values. The freed electron concentration decreased either because the concentration of filled traps decreased from photon and LED excitation, or because the number of trapping sites decreased as charged impurities drifted to the electrode and were

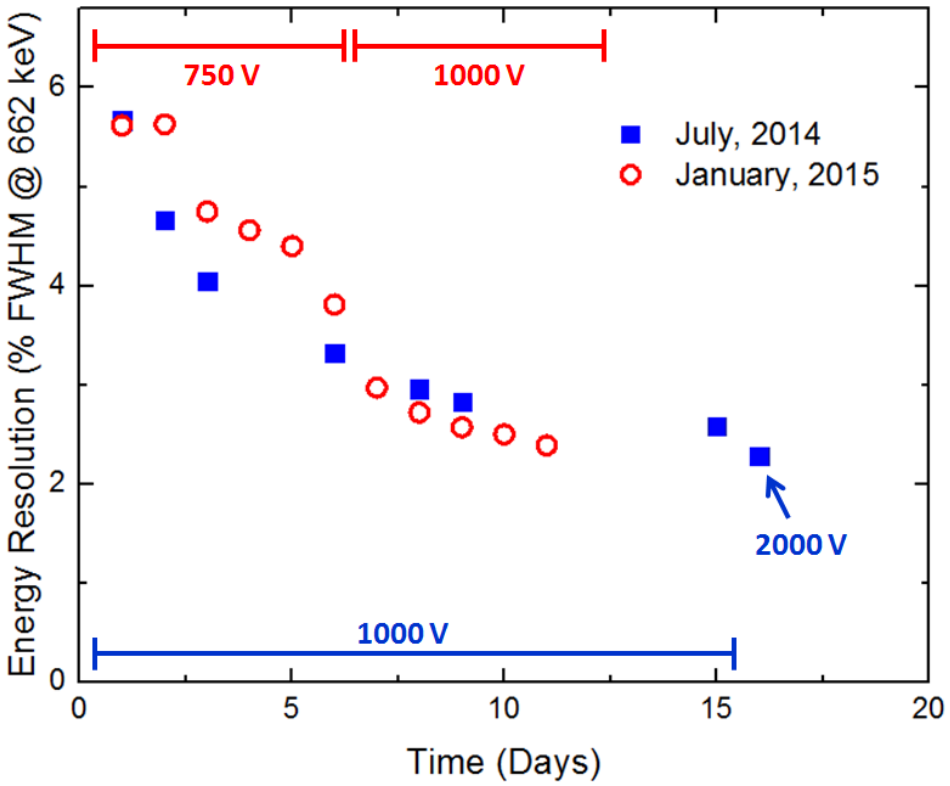

Figure 5.30: Time-dependent energy resolution for detector 44B2L during two different conditionings.

neutralized. In the latter case, lowering the bulk material impurity concentration would shorten the conditioning time. In either case, the total amount of trapped space charge was reduced, resulting in a more uniform internal electric field. From Fig. 5.31, the average effective electric field improved by more than 3x as a result of a more than 4x space charge reduction. The spectroscopy was dependent on the electric field uniformity and improved from 5.6% to 2.4% as a result of the reduced space charge.

Conditioning the detectors multiple times at different biases showed that conditioning mechanisms relaxed when the detector was not at bias and that conditioning speed was dependent on applied bias. Therefore, a higher bias can be applied to condition the detector more quickly. After the device conditions, the bias can be lowered for normal operation.

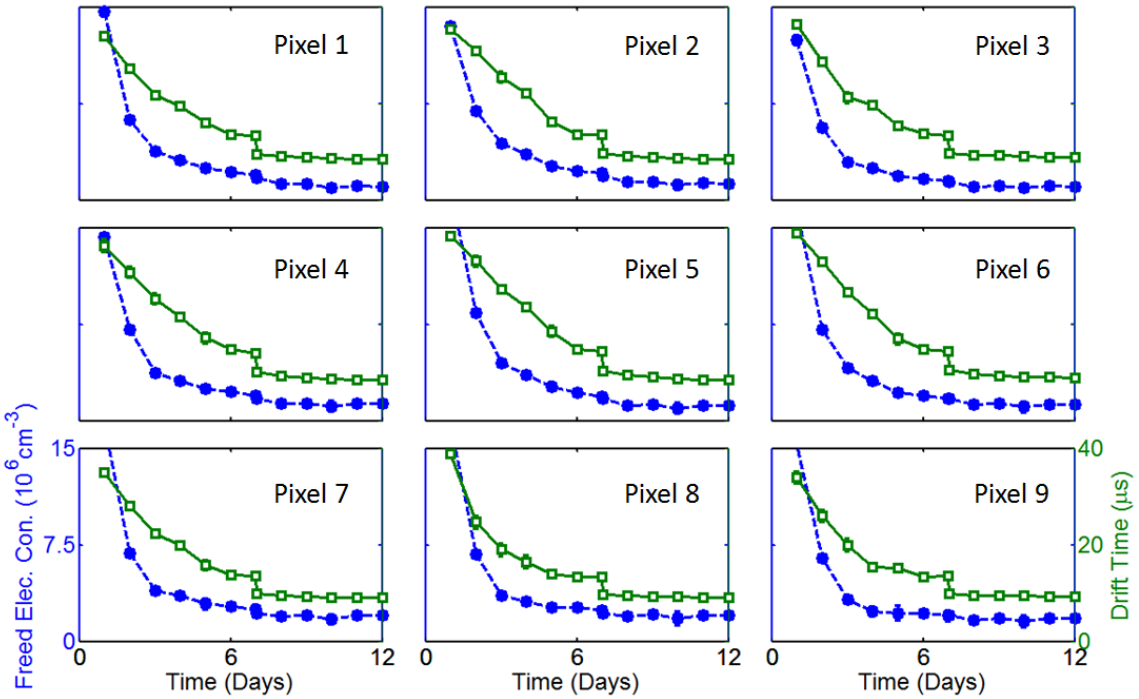

Figure 5.31: Freed electron concentration (solid circle) and cathode-side drift time (open squares) for the January 2015 conditioning in each pixel of detector 44B2L. The discontinuity in the drift time occurs because the bias was increased from 750 V to 1000 V.

Based on these results, it is expected that operating the detector at higher temperatures would decrease the conditioning time because trapped space charge would either migrate more quickly in the case of charged impurities or be freed from thermal excitations in the case of trapped electrons. However, increasing temperature also increases the probability of polarization.

5.3.2.3 Effect of LED Stimulation on the Conditioning Time

As described above, the impurity concentration decrease shown in Fig. 5.31 was caused by either the reduction of filled trap sites from photon and LED excitation, or because the number of trapping sites decreased as charged impurities drifted to the electrode and were neutralized. If the reduction was caused by LED photons and gamma rays freeing trapped electrons, then the conditioning time should decrease if the detector is exposed to an LED for a significant period of time. Fig. 5.32a is the same plot shown in Fig. 5.26, but with an added dataset with periodic LED stimulation. Similarly, Fig. 5.32b is the same plot shown in Fig. 5.30, but with an added dataset with periodic LED stimulation. Various intervals and LED stimulation times were used, but in all cases the conditioning time was not improved (i.e. the new datasets trend with the previous ones).

Fig. 5.33 shows photopeak centroids for detectors 935-16B1L and 44B2L over the same time scale shown in Fig. 5.32. For both detectors, photopeak centroids decreased sharply after the LED illumination. Eventually, original centroids returned. It is likely that LED photons freed trapped electrons, creating more trapping sites for subsequent electron clouds. After some time, the traps were refilled by leakage current, restoring the photopeak centroids to their original positions. The effect was much more pronounced in detector 935-16B1L because the $\mu_e\tau_e$ was only 5.8 $\pm$ 0.7 cm^2/V compared to 14 $\pm$ 5 cm^2/V for detector 44B2L. Because the overall trapping was worse in detector 935-16B1L (lower $\mu_e\tau_e$), the LED freed more trapped

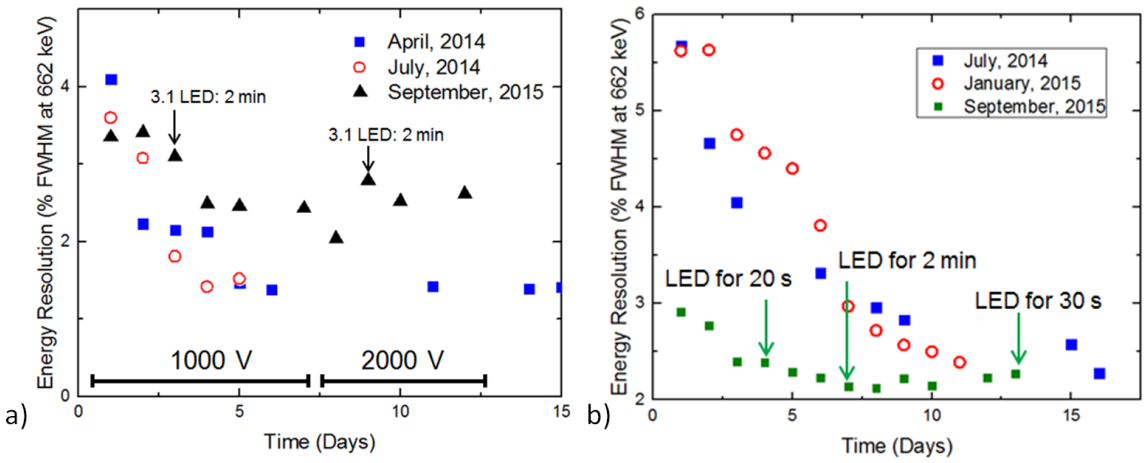

Figure 5.32: Effect of LED on the conditioning phase for detector a) 935-16B1L and b) 44B2L. For both detectors, the LED did not effect the conditioning time.

electrons, creating more empty trapping sites, and the photopeak drops were more severe. Because LED stimulation had no effect on the conditioning time, it is likely that the decrease in freed electron concentrations shown in Fig. 5.31 was the result of fewer trapping sites and not a change in whether a given trapping site was filled or empty. Again, this could be caused by charged impurities drifting out of the bulk under the applied field and being neutralized by the contacts.

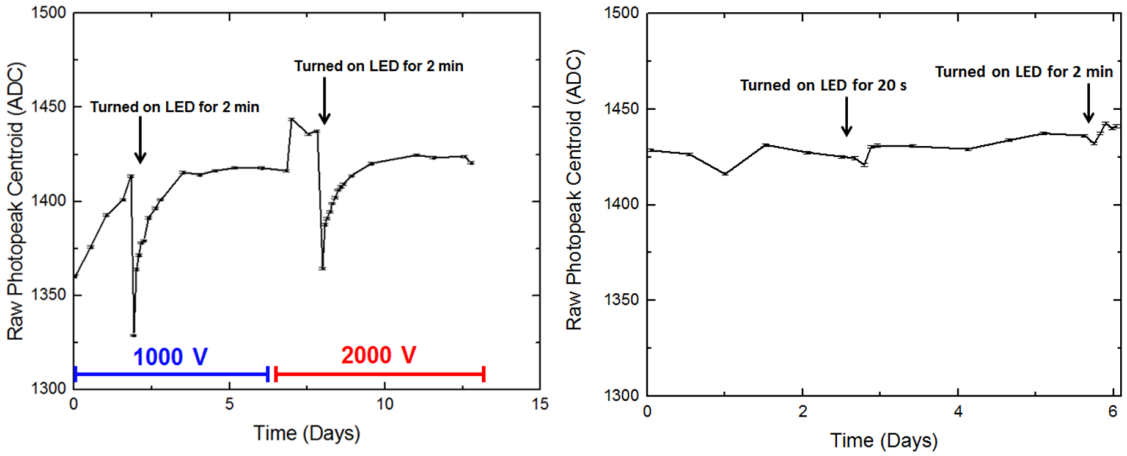

Figure 5.33: Effect of LED photons on the photopeak centroid in detector a) 935-16B1L and b) 44B2L. The LED photons freed trapped electrons, which increased the trapping and decreased the photopeak centroid. The $\mu_e\tau_e$ was higher in detector 44B2L, therefore, the effect was not as large.

CHAPTER VI

Characterization and Improvement of TlBr During Room-Temperature Operation

As described in Chapter I, TlBr detectors degrade after days to months of continuous bias at room-temperature. This so-called polarization is thought to be the result of ionic conduction where Tl^+ and Br^- ions break from their lattice sites and drift under the applied bias. The resulting space-charge buildup under the electrodes either causes an internal field reduction or facilitates contact-to-bulk interactions. This chapter describes work done to understand the mechanisms behind polarization and isolates degradation to near the anode surface. To verify that polarization was a contact phenomenon as opposed to a bulk phenomenon, two polarized detectors were refabricated (electrodes polished off and re-applied). After refabrication, device performance returned.

6.1 Methods

To ensure constant temperature, detectors were polarized in the environmental chamber at 20 °C. A -1000 V cathode bias was applied continuously and the detectors were flood irradiated with 662 keV gamma rays from ^{137}Cs. Due to the poor energy resolution of polarizing detectors, the cathode surface was also irradiated with

5.5 MeV alpha-particles from ^{241}Am. Because of the small mean free path of alpha particles in solids, this provided a mono-energetic source of cathode-side events. These events were used to determine depth-dependent drift velocities using a method similar to the gamma-ray method described in Sec. 3.3.1.3 [32]. Average drift velocities were calculated from drift velocity profiles.

After two detectors were polarized, RMD Inc. removed the electrodes along with 0.5 mm of bulk material under the cathode and anode surfaces. New Cr/Au electrodes were applied and the detectors were retested at $-20\,^{\circ}$C and -1000 V cathode bias.

6.2 Results

Each detector tested showed slightly different characteristics. Therefore, the results are first analyzed on a detector-by-detector basis. Then, common conclusions are used to characterize general room-temperature performance.

6.2.1 Detector 44AB1R

After 15 days of room-temperature operation, detector 44AB1R suffered complete failure, characterized by breakdown between the cathode and anode pixels. After breakdown, no measured signals were observed on the preamplifiers. Fig. 6.1 shows the time-dependent, depth-corrected, 662 keV, single-pixel energy spectrum. After three days of continuous room-temperature operation, the photopeak and Tl characteristic x-ray escape peaks were almost unresolvable. The spectra were normalized by the total number of counts which was not preserved from $-20\,^{\circ}$C to room-temperature. The processing electronics were noisier at room temperature which caused noise triggers and increased system dead time. The total number of counts for the reference spectrum at $-20\,^{\circ}$C, day 1, day 2, and day 3 of room-temperature operation were 2.8 x 10^6, 2.2 x 10^6 , 2.1 x 10^6, and 2.0 x 10^6, respectively. The ratio of counts above 500 keV to the total counts is listed to the right of each photopeak and

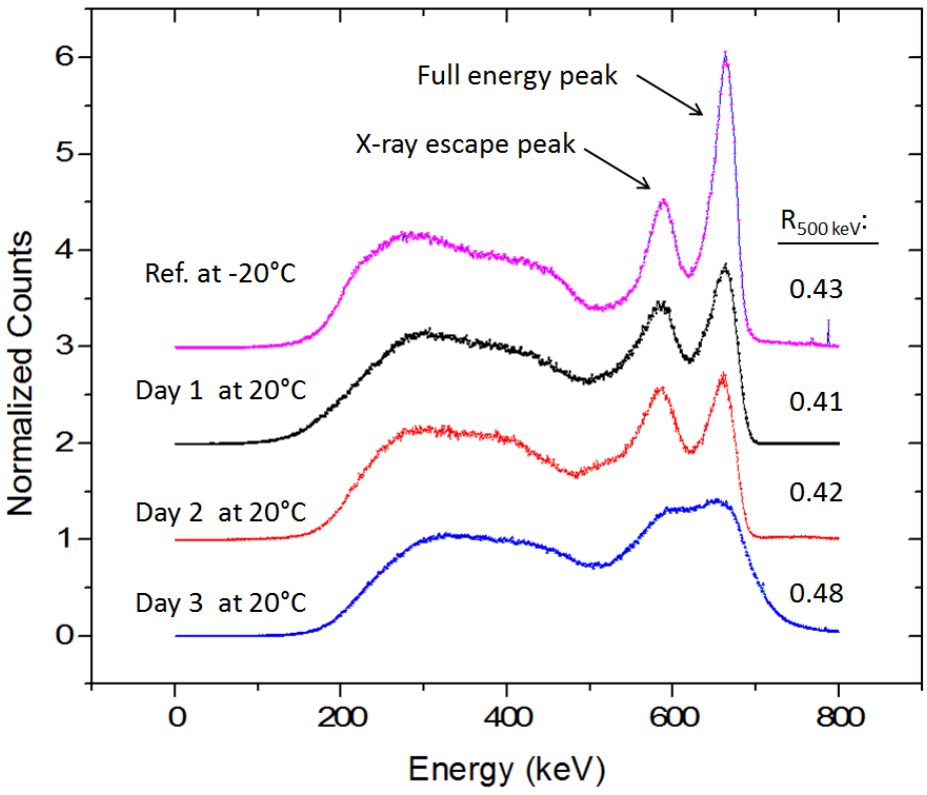

Figure 6.1: Time evolution of the depth-corrected ^{137}Cs energy spectrum for detector 44AB1R. Each spectra was from a 24-hour measurement. The spectrum at $-20\,^{\circ}$C is shown for reference. Days 1-3 were taken at room-temperature. The spectra are offset for clarity.

remained relatively constant, indicating that photopeak events were not preferentially lost to the Compton continuum during polarization.

Fig. 6.2 shows leakage current and average electron drift velocity over the first 300 hours of room-temperature operation. Secs. 3.3.1.3 and 3.3.3 detail how these quantities were measured. The leakage current and average drift velocity are related to the electric field through:

$$I = (n\mu_e qA)\,E \tag{6.1}$$

and

$$v_e = \mu_e E \tag{6.2}$$

where I is the leakage current through the bulk, n is the free electron number density,

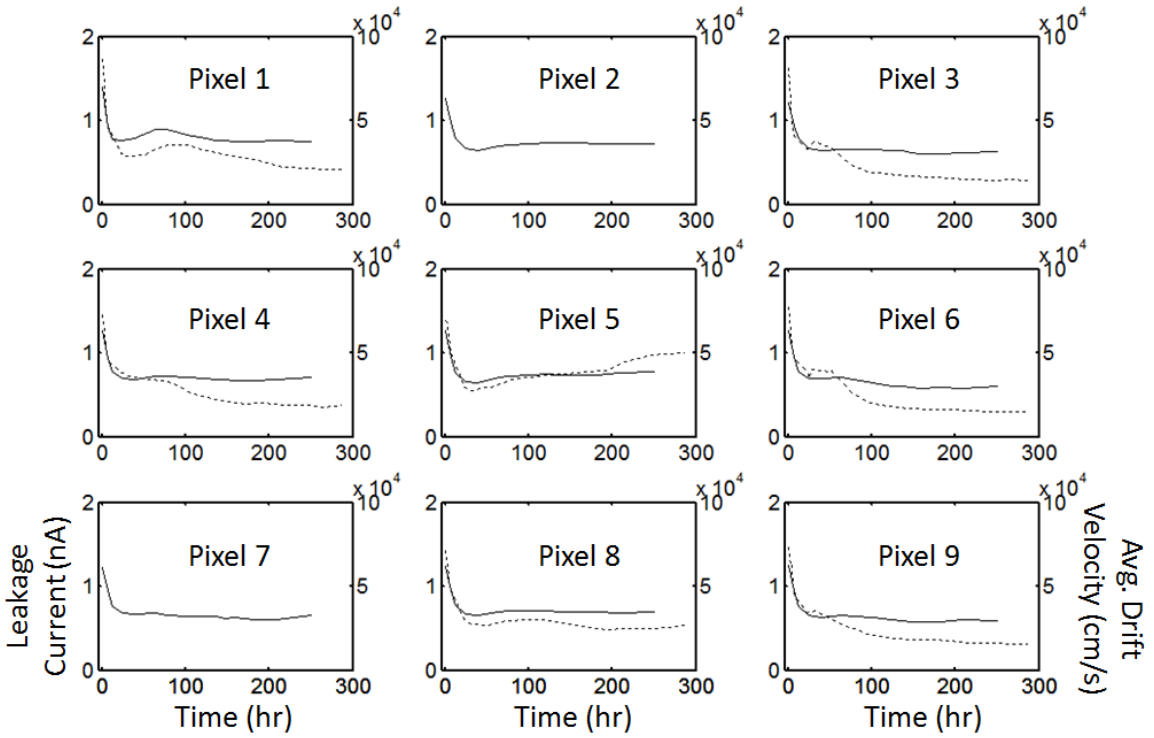

Figure 6.2: Leakage current (dashed curve) and average electron drift velocity (solid curve) over the first 300 hours of room-temperature operation for detector 44AB1R. Both quantities are indirect measurements of the effective electric field. Leakage current data were not available for pixels two and seven.

μ_e is the electron mobility, A is the pixel area, E is the average electric field, and v_e is the electron drift velocity. The detectors did not have a grid between pixels, therefore, there was no extra grid-to-pixel current. From Eqs. 6.1 and 6.2, both leakage current and average electron drift velocity are indirect measurements of the average effective electric field, explaining the correlation observed in Fig. 6.2. As the device polarized and the electric field decreased as a result of ionic conduction, both the leakage current and electron drift velocity also decreased. In all nine pixels, both quantities dropped dramatically over the first twelve hours and then reached a horizontal asymptote, suggesting that most of the electric field reduction occurred at the beginning of room-temperature operation.

From Figs. 6.1 and 6.2, no correlation exists between average electric field and detector performance. For example, the electric field decreased dramatically in the first 12 hours while the detector performance showed minimal change. Similarly, the energy resolution degraded dramatically between days two and three, while there was little change in the electric field strength (hours 24 to 48 in Fig. 6.2). While ionic conduction was likely causing a reduction in electric field strength [38, 71], Figs. 6.1 and 6.2 show that this reduction was not the primary cause of device degradation.

In addition to poor energy resolution, the average raw ADC amplitude of the induced voltage pulses decreased as a function of time. The gamma-ray spectra were too poor to track the photopeak centroid after a few days (see Fig. 6.1), therefore, alpha-particles from ^{241}Am were used to quantify the ADC amplitude shift. Unlike gamma rays, alpha-particles deposit their full energy in a single interaction. As a result, anode alpha spectra contained a full-energy peak and no Compton continuum. Similarly, alpha cathode spectra only contained a full-energy peak because the energy deposition occurred right at the cathode surface. For gamma rays, variation in cathode amplitude from mono-energetic depositions is the result of interactions occurring at different depths. Fig. 6.3 shows the normalized, time-dependent, full-energy,

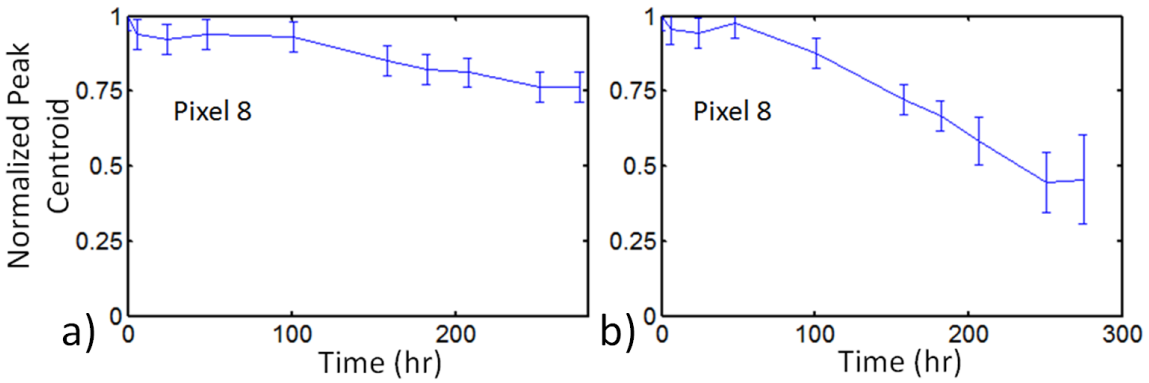

Figure 6.3: Full energy alpha-particle peak centroid shift as a function of time for a) the cathode and b) the anode signals in detector 44AB1R.

alpha-particle peak shift for both cathode and the anode signals in pixel eight. Due to limited geometry, only pixels two, five, and eight had sufficient alpha data. Pixel 8 was representative of all three pixels.

Fig. 6.3 shows that the anode peak shift was much greater than the cathode peak shift. According to the Shockley-Ramo theorem, the induced charge on an electrode is proportional to the generated charge multiplied by the weighting potential change (see Sec. 2.1) The largest weighting potential change for a pixelated anode (see Fig. 6.4b) occurs near the anode surface, therefore, most anode signal induction occurs at the end of electron drift. Any increase in the number of trapping sites, either in the bulk or near the anode surface, will affect the anode signal more than the cathode signal because trapped charge will move through the cathode weighting potential but not the anode weighting potential. The discrepancy between anode and cathode peak shifts as a function of time shown in Fig. 6.3, indicates an increase in the number of trapping sites. Isolating bulk trapping effects from anode-side trapping effects requires depth-dependent photopeak centroid analysis. Due to the rapid spectroscopic performance degradation shown in Fig. 6.1, this analysis could not be performed on detector 44AB1R.

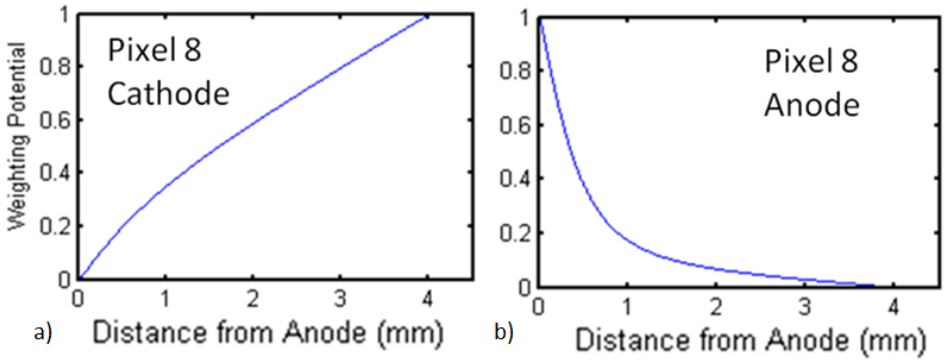

Figure 6.4: a) Cathode and b) anode weighting potentials for detector #44AB1R. The detector was 4 mm thick.

6.2.2 Detector 935-29-AA1-3

Detector 935-29-AA1-3 achieved 2.06% FWHM at 662 keV at $-20\,^{\circ}$C, which was average for pixelated TlBr detectors tested at the University of Michigan [46]. It polarized after 15 days of room-temperature operation. Due to geometric limitations, the alpha-particle efficiency was too low to track the ADC gain shift over time using ^{241}Am. However, the gamma ray energy resolution was sufficient throughout polarization to track the peak shift. Fig. 6.5 shows the photopeak centroid as a function of time for pixel 4. The slope of pixel 4 was 5.9 x 10^{-3} normalized ADC/day and is representative of all nine pixels. The average slope and standard deviation over the nine pixels was 6.0 x 10^{-3} and 2.3 x 10^{-3} normalized ADC/day respectively. From Fig. 6.3b, the slope in pixel 8 for detector 44AB1R was 5 x 10^{-2} normalized ADC/day. The large discrepancy in anode peak degradation between the two detectors could indicate that ionic current was higher in detector 44AB1R.

Fig. 6.6 summarizes the time-dependent gamma-ray energy resolution during room-temperature operation. The energy resolution ranged from 4% to 9% FWHM at 662 keV. Similar to 44AB1R, there was no correlation between the average electric field strength, measured indirectly using average drift velocities and leakage current, and the gamma-ray energy resolution for detector 935-29-AA1-3.

Fig. 6.7 shows cathode waveforms in pixel seven from alpha particles incident

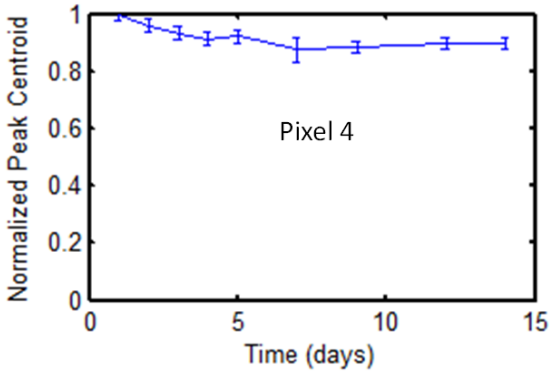

Figure 6.5: Photopeak centroid as a function of time in pixel 4 of detector #935-29-AA1-3. The average degradation was representative of all 9 pixels.

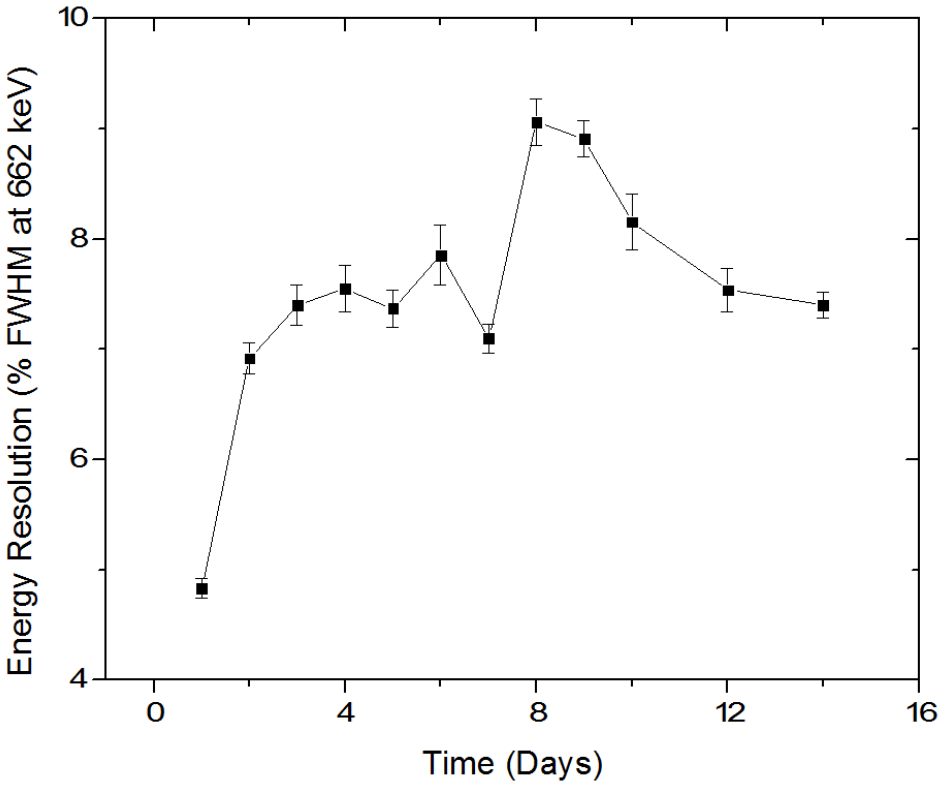

Figure 6.6: Energy resolution as a function of time for detector 935-29-AA1-3.

on the cathode side of the detector after one and eight days of room-temperature operation. Individual waveforms are shown in gray and the average waveform is shown in black. Initially, waveforms were uniform and showed little deviation from the average. During the eighth day, a fast region, evidenced by the steep slope at the end of the drift, developed near the anode side. Additionally, the waveforms show a large deviation in this region. Fast regions near the anode surface have been observed in other 5 mm thick TlBr detectors [46]. The high drift velocity and deviation was likely caused by non-uniform accumulation of negative space charge (the result of ionic conduction) near the anode electrode. According to Poisson's equation, negative space charge under the anode causes a larger electric field in the region of space charge and a lower electric field in the rest of the bulk. Fig. 6.7 indicates that the dominating polarization effects occurred near the anode. If polarization occurred throughout the bulk, there would be significant deviation over the whole waveform instead of just near the anode. Fig. 6.7 shows data from pixel seven which represents all pixels.

Fig. 6.8 shows depth-dependent energy resolution in pixel 6 for days one and twelve, also indicating anode side degradation. If polarization affected the bulk, the energy resolution would degrade more severely near the cathode surface because cathode-side events have to travel through more of the bulk. Instead, Fig. 6.8 shows uniform degradation at all depths, indicating that polarization for this detector was concentrated near the anode surface.

Photopeak amplitude shifts were also observed in detector 935-29-AA1-3. The gamma ray performance remained good enough to observe depth-dependent photopeak amplitude as a function of time during polarization (see Fig. 6.9). The average photopeak amplitude decreased with time, indicating the trapping site concentration increased. Additionally, the photopeak amplitude decreases uniformly at all depths, suggesting that most of the new trapping sites were created near the anode surface. If new trapping sites were created in the bulk, photopeak amplitudes near the cathode

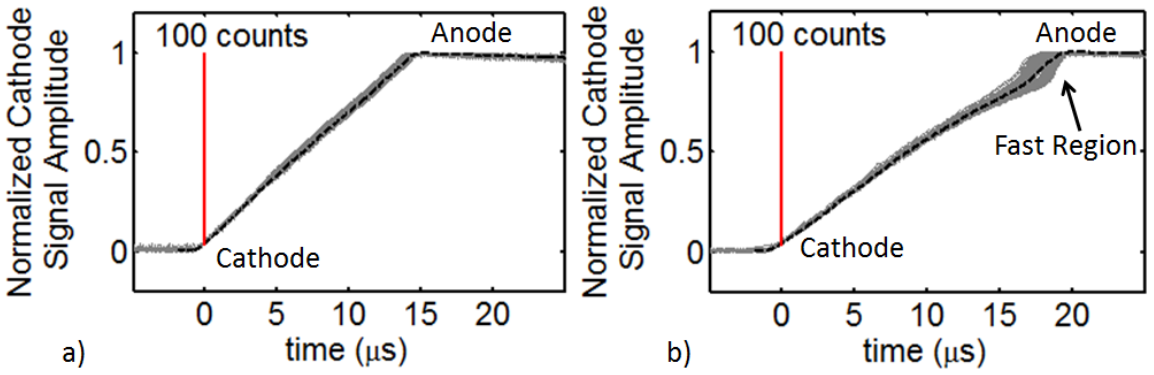

Figure 6.7: Cathode waveforms of alpha-particles incident on the cathode side of detector 935-29-AA1-3 after a) one day and b) eight days of room-temperature operation. Data shown are from pixel seven but are representative of the entire detector.

surface would decrease more rapidly than photopeak amplitudes near the anode surface (e.g. see Fig. 5.9). Pixel 9 had insufficient counts at each depth and should be ignored. Introduction of new trapping sites near the anode surface could be caused by diffusion of Au from the electrode into the crystal, as outlined in Ref. [36]. It is likely that space charge buildup from ionic conduction is necessary for the Au diffusion mechanisms outlined in Ref [36] and Ref. [38]. Therefore, it is expected that both a fast region from the ionic conduction and heavy trapping from Au diffusion occurred near the anode electrode.

6.2.3 Refabricated Detectors

Detectors 70BA1R and 44A12R operated at room-temperature for one and five days respectively. Fig. 6.10 shows the 662 keV gamma ray spectrum after initial bias at $-20\,^{\circ}\mathrm{C}$, during polarization at room temperature, and after refabrication at $-20\,^{\circ}\mathrm{C}$. For both detectors, energy resolution was the best during initial operation, degraded during polarization, and improved to almost initial values after refabrication. During refabrication, 1 mm of material, which was roughly 20% of the bulk crystal, was removed. The anode weighting potential is significantly non-zero approx-

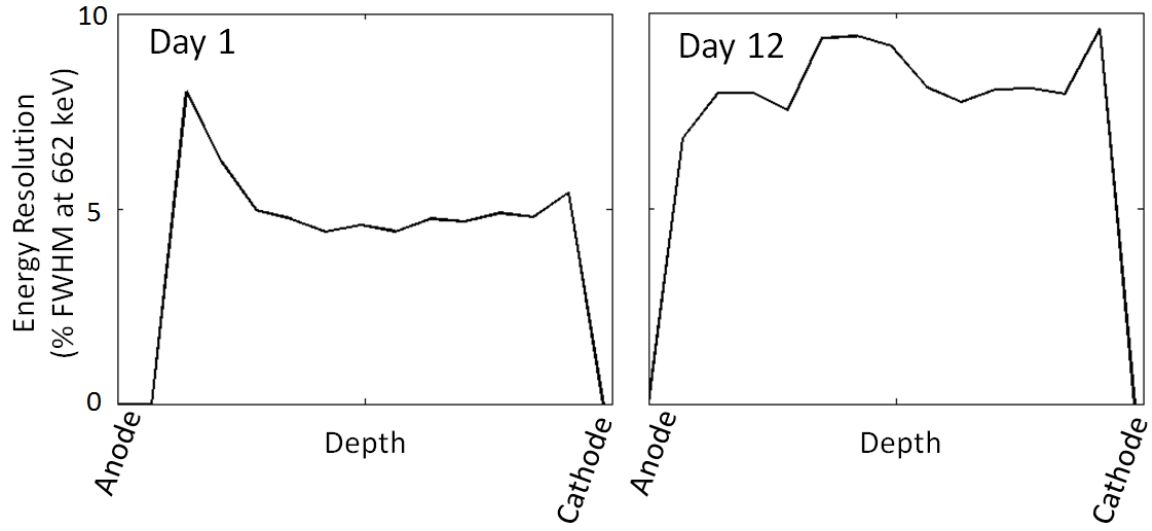

Figure 6.8: Depth-dependent energy resolution at 662 keV for 935-29-AA1-3 after a) 1 day b) 12 days of applied bias at room-temperature. The uniform energy resolution degradation as a function of depth indicates an anode side polarization effect. Data shown are from pixel six but are representative of the entire detector.

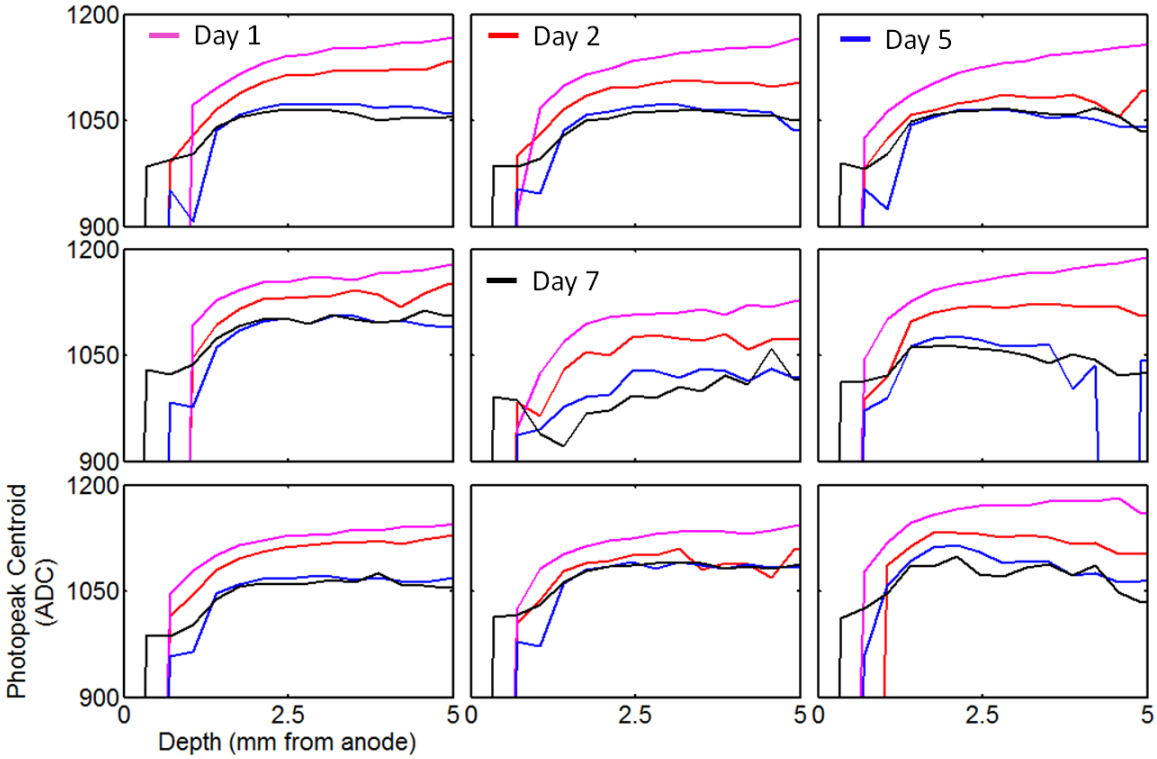

Figure 6.9: Photopeak centroids as a function of depth during day 1, day 2, day 5, and day 7 for detector 935-29-AA1-3. The photopeak amplitudes decreased uniformly at all depths, indicating that trapping sites were created near the anode surface.

imately one pixel pitch from the anode surface, resulting in poor performance near the anode. Therefore, removing 20% of the material caused the poor spectroscopy region to become a larger fraction of the crystal bulk, resulting in slightly worse energy resolution after refabrication. Performance recovery following refabrication indicates that polarization does not permanently damage the bulk material and is localized to near electrode surfaces, confirming depth-dependent signal analysis.

6.2.4 Visual Degradation

In addition to performance degradation, TlBr detectors also showed extreme visual damage after room-temperature operation. Fig. 6.11 shows pixelated anodes for typical detectors after $-20\,^{\circ}\mathrm{C}$ and room-temperature operation. Discoloration after room-temperature operation was likely caused by electrochemical reactions between the bulk and contact. As a result, the degraded electrodes started to look more like bulk TlBr (i.e. the material outside the guard ring and between pixels).

6.2.5 Initial Results with Tl Electrodes

As mentioned in Sec. 1.4.2, TlBr detectors with Tl electrodes show minimal polarization when the polarity of the bias is switched every couple of hours. For example, -1000 V cathode bias is applied for four hours. Afterward, +1000 V cathode bias is applied for four hours to recharge the device. During recharging, the device is inactive. Depth dependent signal analysis was applied to a 5 mm thick pixelated TlBr detector with Tl electrodes, manufactured by K. Hitomi from Tohoku University in Japan, to see if polarization was slowed. Various measurement/recharging times, ranging from four to twenty-four hours were applied over 28 days. The energy resolution remained between 1.6% and 1.8% FWHM at 662 keV during the entire 28 days. Fig. 6.12 shows the drift velocity profile at at three different days. Over the room-temperature operation, there is no change in the profile shape or magnitude,

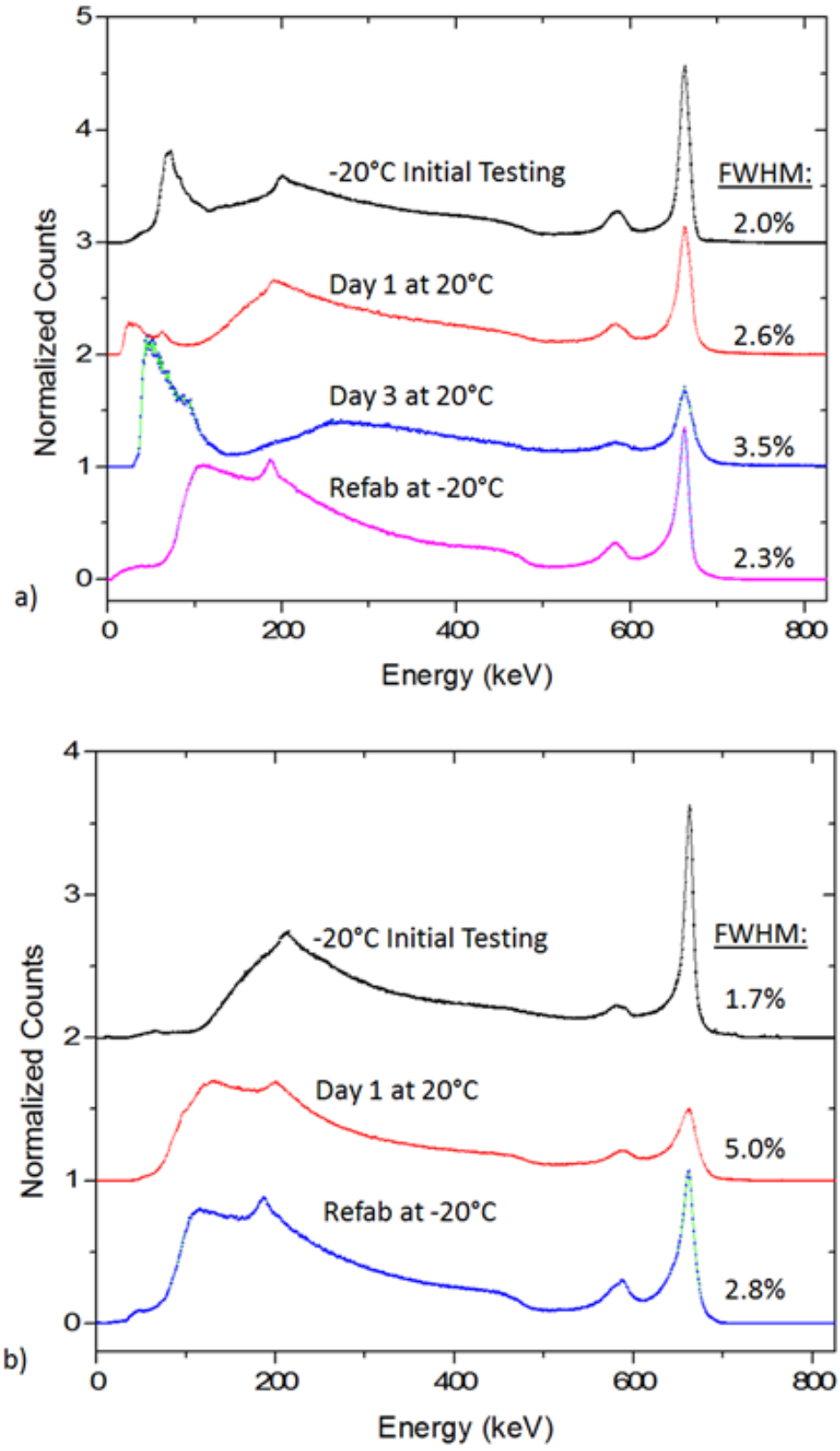

Figure 6.10: Single-pixel, ^{137}Cs energy spectra for detectors a) 44A12R and b) 70BA1R after initial bias, during room temperature operation, and after refabrication.

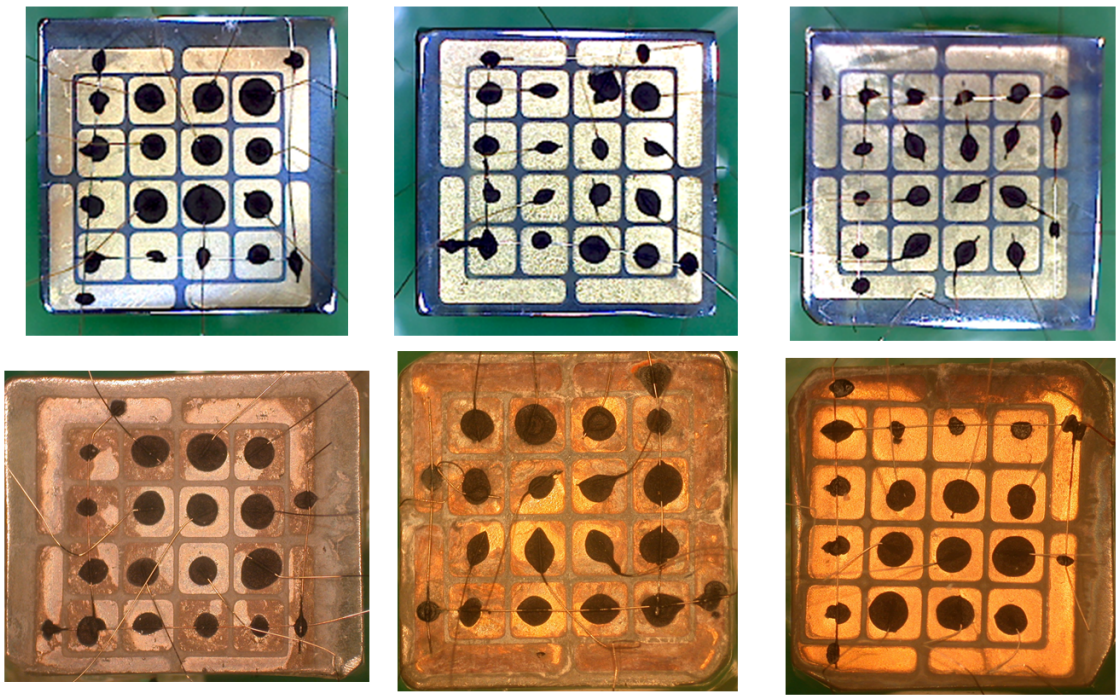

Figure 6.11: Top row: Typical pixelated anode after $-20\,^{\circ}\mathrm{C}$ operation. Bottom row: Typical pixelated anode after room-temperature operation. The degraded anode after polarization is thought to be caused by bulk ions reacting with the contact material.

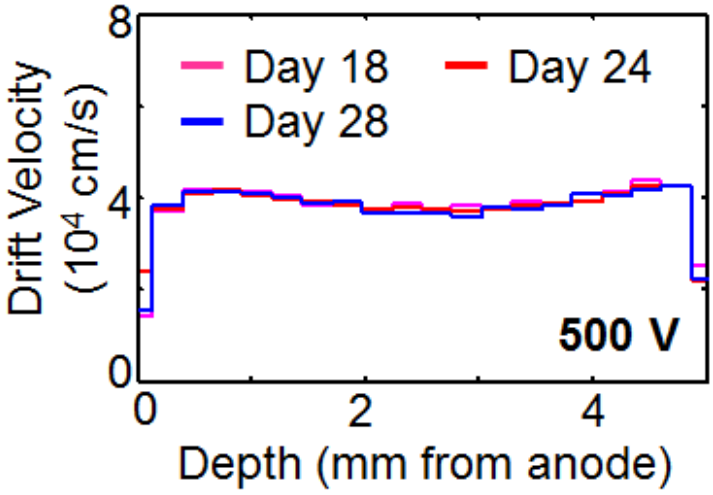

Figure 6.12: Drift velocity profile during different measurement days for a TlBr detector with Tl electrodes at room temperature. No significant change in the profile indicates insignificant polarization.

indicating insignificant polarization.

6.3 Summary

Polarization occurs in TlBr detectors after days to months of room-temperature operation. By studying leakage current, gamma-ray response, and alpha-particle response of two TlBr detectors, it is likely that performance degradation was more heavily influenced by mechanisms occurring near the anode surface as opposed to near the cathode surface or in the bulk. Uniform depth-dependent photopeak amplitude degradation during polarization suggested that trapping sites were formed near the anode, possibly the result of Au migration from the electrode into the crystal. The fact that detectors were responsive to radiation after refabrication, verifies that polarization did not permanently damage the bulk crystal but was localized to within 0.5 mm of the electrode surfaces. Therefore, if long term, room-temperature stabil-

ity of TlBr detectors is desired, future work should continue to focus on improving electrode fabrication to minimize reactions between the surface TlBr and the contact material. Additionally, Tl electrodes were shown to minimize polarization at room temperature.

CHAPTER VII

11 x 11 Pixelated Detectors

Most of the work presented in Chapters V and VI used smaller 3 x 3 pixelated TlBr detectors because of the more versatile readout system (the Gage card sampling frequency and sampling window could be adjusted for virtually any testing scenario). However, 3 x 3 detectors are not practical for field deployable devices because they are fragile (the thin Pd anode wires break or short circuit if they are not handled with extreme care), have a small active volume ($\sim$0.045 cm^3), are time consuming to manufacture (each anode wire is hand bonded to the readout pins), and have limited imaging capabilities.

In an effort to increase detector active volume and use compact digital ASIC readout systems currently used for CZT [53], 11 x 11 pixelated TlBr detectors were developed. These larger detectors were possible because of improvements in TlBr purification and growth techniques.

7.1 Detector Performance

7.1.1 Energy Resolution and Detector Uniformity

As of the writing of this thesis, seven 11 x 11 pixelated TlBr detectors were manufactured by RMD for the University of Michigan. Two detectors (935-41AS2 and 935-43AS6) were sent in an initial batch to verify electrode fabrication processes.

Table 7.1: Performance of 11 x 11 TlBr detectors. All resolutions reported for −20 °C operation.

Detector	Batch	Resistivity (Ω cm)	Energy Resolution (% FWHM at 662 keV)	$\mu_e\tau_e$ (cm^2/Vs)
935-41AS2	1	10^{10}	-	
935-43AS6	1	10^{11}	2.06	
935-34BS3	2	10^{11}	2.40	
935-38AS3	2	10^{11}	3.28	3.8 ± 1.2
935-38AS4	2	10^{11}	2.26	4.4 ± 1.5
935-39BS5	2	10^{10}	3.92	
935-40AS2	2	10^{10}	5.45	

After fabrication verification, five more detectors (935-38AS3, 935-38AS4, 935-34BS3, 935-40AS2, and 935-39BS5) were sent to UM. Based on results from batch 1, these batch 2 detectors included an underfil epoxy on the anode electrode to help maintain bonding when the detectors were cooled to −20 °C.

Fig. 7.1 shows the overall single-pixel spectrum and pixel-by-pixel energy resolution (% FWHM at 662 keV) for detector 935-43AS6 at −20 °C. The two red pixels were not connected to readout channels due to a wiring error. Black pixels with FWHM = 0.00 were poorly bonded to the substrate. The overall single-pixel energy resolution was 2.06% FWHM at 662 keV. In general, inner 9 x 9 pixels outperformed outer pixels because they had smaller effective areas, reducing noise from leakage current.

Fig. 7.2 shows the overall single-pixel spectrum and pixel-by-pixel energy resolution in % FWHM at 662 keV for detector 935-34BS3 at −20 °C. Detector 935-34BS3 was from batch 2, therefore, none of the pixels were poorly bonded. Similar to detector 935-43AS6, inner 9 x 9 pixels tended to outperform outer pixels. Fig. 7.2b shows fairly uniform performance across most pixels. Table 7.1 summarizes the performance of the seven 11 x 11 detectors. Detector 935-41AS2 could not hold a bias higher than 500 V due to high leakage current. In general, high resistivity detectors outperformed low resistivity detectors.

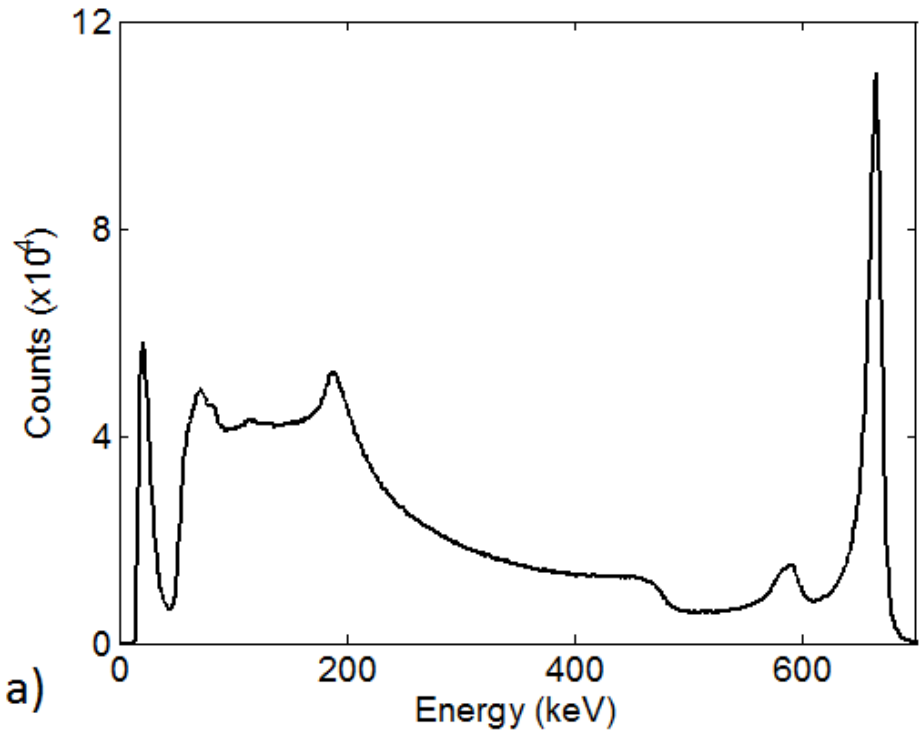

7.06	3.99	0.00	0.00	3.81	3.25	4.23	3.98	2.21	3.09	4.55
4.53	0.00	0.00	2.29	1.84	2.29	2.60	2.34	1.92	2.13	3.06
3.57	2.37	0.00	7.91	2.19	1.88	2.09	1.87	1.68	2.16	2.47
2.59	1.81	2.03	1.91	2.10	1.99	2.30	2.02	1.67	1.69	2.99
2.24	1.63	11.37	1.61	1.66	1.91	2.50		1.82	1.70	2.15
2.13	2.01	1.90	1.68	1.77	1.71	1.66		2.17	1.76	2.09
4.34	1.59	1.86	1.67	1.47	1.45	1.70	3.82	0.00	1.69	3.08
2.18	1.77	1.88	1.95	1.52	1.53	2.48	3.53	0.00	1.87	3.68
3.79	1.45	2.21	1.46	1.48	1.73	2.12	2.60	2.01	0.00	2.05
2.78	2.24	2.29	1.77	1.69	1.92	1.91	1.99	2.17	1.85	0.00
0.00	0.00	2.23	2.54	1.84	2.05	1.83	2.05	2.14	1.25	2.92

b)

Figure 7.1: a) Single-pixel spectrum and b) pixel by pixel energy resolution (% FWHM at 662 keV) for detector 935-43AS6. The red pixels were not connected to readout channels. The overall single pixel energy resolution was 2.06% FWHM at 662 keV.

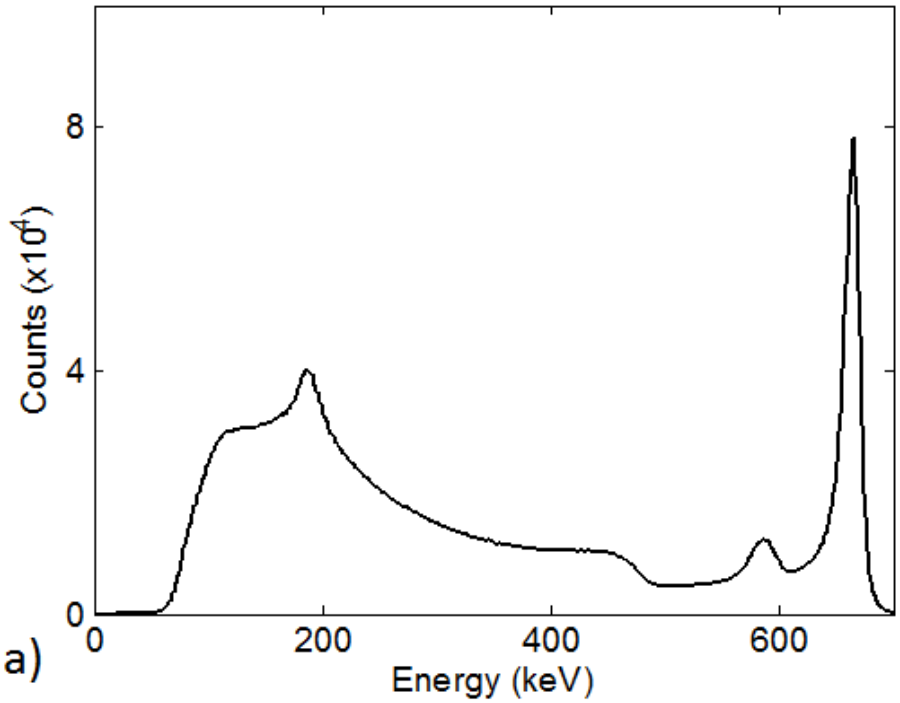

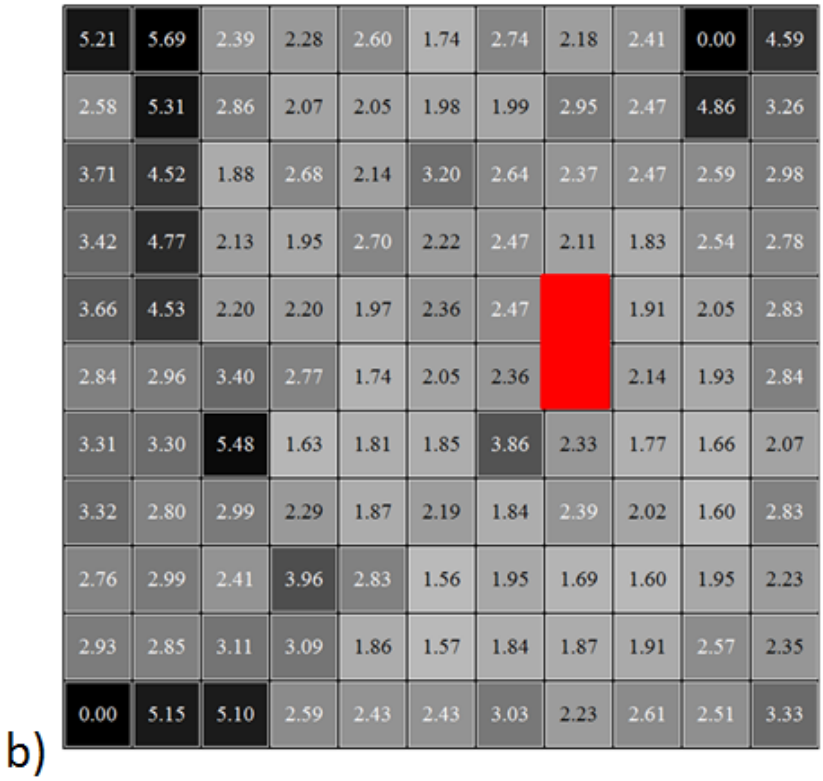

Figure 7.2: a) Single-pixel spectrum and b) pixel by pixel energy resolution (% FWHM at 662 keV) for detector 935-34BS3. The red pixels were not connected to readout channels. The overall single pixel energy resolution was 2.40% FWHM at 662 keV.

7.1.2 Direct Comparison to CZT

One of the major advantages of TlBr over CZT is its high effective atomic number and density. Therefore, TlBr detectors should be more efficient and have higher photopeak fractions. The overall efficiency and performance of a detector is dependent upon processing electronics, therefore, a direct comparison between two detectors must use the exact same data acquisition system. An 11 x 11 pixelated CZT and 11 x 11 pixelated TlBr detector, each nominally 5 mm thick, were flood irradiated with the same ^{137}Cs source, for the same measurement time. Most importantly, the data were processed with same single-module digital ASIC. The pixel-pitch of the CZT detector was 1.72 mm while the pixel pitch of the TlBr detector was 1 mm. The average count rates for the CZT and TlBr detectors were 1663 cts/s and 1115 cts/s, respectively. When corrected for active volume and dead pixels (4 dead pixels on CZT, 17 dead pixels on TlBr), the count rates were 960 cts/s/cm^3 and 2331 cts/s/cm^3, respectively. Therefore, on a per active volume basis, the TlBr detector was 2.4 times efficient compared to the CZT detector. This was expected due to the higher density of TlBr.

Figs. 7.3a and 7.3b show the TlBr and CZT 662 keV spectra. There was significant low energy tailing because the detectors were operated at 500 V to ensure that the TlBr detector did not polarize at room temperature. The photopeak efficiencies were 0.25 and 0.08 for TlBr and CZT, respectively. The theoretical values for photopeak efficiency, estimated from the attenuation coefficients, are shown in parentheses. The measured values were lower than theoretical values because of scattering in surrounding material. A source gamma ray can scatter in surrounding material, depositing some energy. If the remaining energy was deposited into the detector, it would have added a count to the Compton continuum and not the photopeak. Due to a larger effective atomic number, the photopeak efficiency was about 3x greater for TlBr compared to CZT. The energy resolution was much better for CZT, but should

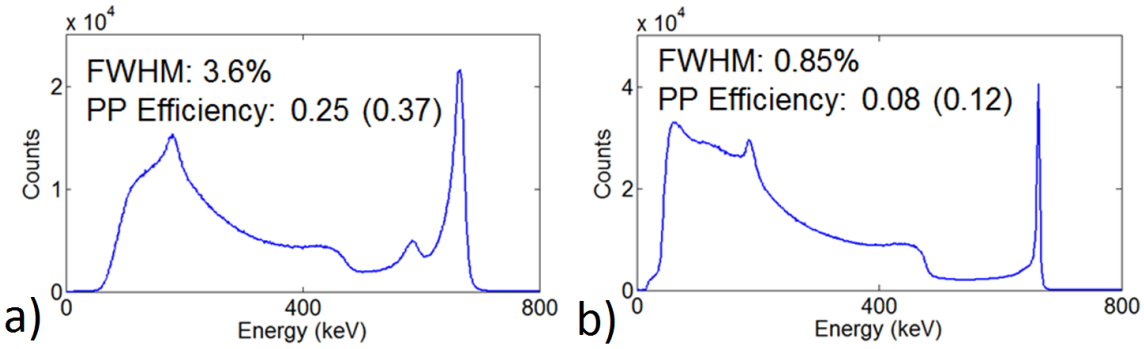

Figure 7.3: All event ^{137}Cs spectrum for a) TlBr and b) CZT. TlBr has a significantly higher effective atomic number, resulting in ∼3x improvement in photopeak efficiency. The values in parentheses are theoretical and overestimate the experimental values because they do not account for scattering from the surrounding material.

improve for TlBr as the material matures.

7.2 Potential of Using the Tl Characteristic X-ray

As described in Sec. 3.3.5, there is a significant probability that characteristic x-rays released from photoelectric interactions in TlBr will escape to a neighboring pixel. The characteristic x-ray events can be identified and used to improve isotope identification and multiple pixel energy resolutions.

7.2.1 Improving Isotope Identification

Fig. 7.4a shows a typical single-pixel spectrum for an 11x11 pixelated TlBr detector. The Compton continuum below the photopeak can act as background for lower energy gamma ray lines. As a result, suppressing the Compton background can help idetify peaks from low activity sources. Fig. 7.4b shows single-pixel energies from two-pixel events (i.e. if a two-pixel event occurs, depositing energies E_1 and E_2, both E_1 and E_2 are separately binned in Fig. 7.4b). As expected, many two-pixel events are the result of a photoelectric event in one pixel and a characteristic x-ray event in another pixel. This resulted in the large peak at the x-ray energies around 75 keV. In reality, there are four peaks from 70-80 keV, but the energy resolution is not good

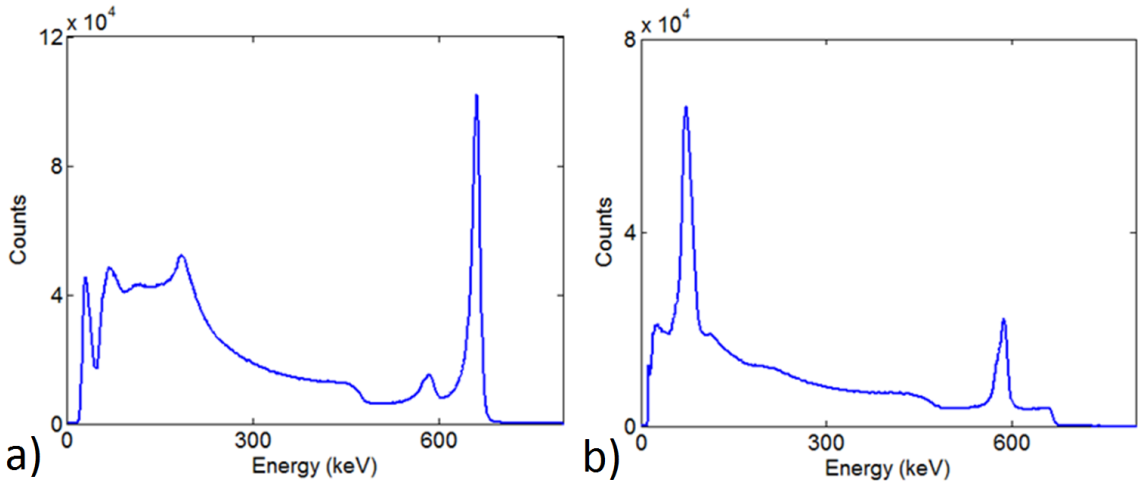

Figure 7.4: a) Single-pixel spectrum and b) single energy from two-pixel events. The peak around 75 keV in b) is the result of characteristic x-rays.

enough to resolve them.

A filtered x-ray spectrum was obtained by binning the summed energy (E_1+E_2) for all events in which one energy deposition (E_1 or E_2) was in the x-ray energy region (68-82 keV). Fig. 7.5 shows the filtered x-ray energy spectrum (red curve) superimposed on the single-pixel spectrum (7.5a, blue curve) and two-pixel spectrum (7.5b, blue curve). Each spectrum was normalized by the number of photopeak counts. From Fig. 7.5a, it was clear that the Compton continuum of the filtered spectrum was depressed compared to single-pixel spectrum. However, while the photopeak energy resolution remained constant, the total number of photopeak events decreased by about an order of magnitude. Fig. 7.5b shows that while filtering on two-pixel events reduced the Compton continuum, the energy resolution was improved with characteristic x-ray filtering. Therefore, this Compton suppression technique could be implemented to reduce the Compton background when a low activity source is in the presence of a higher energy, high-activity source.

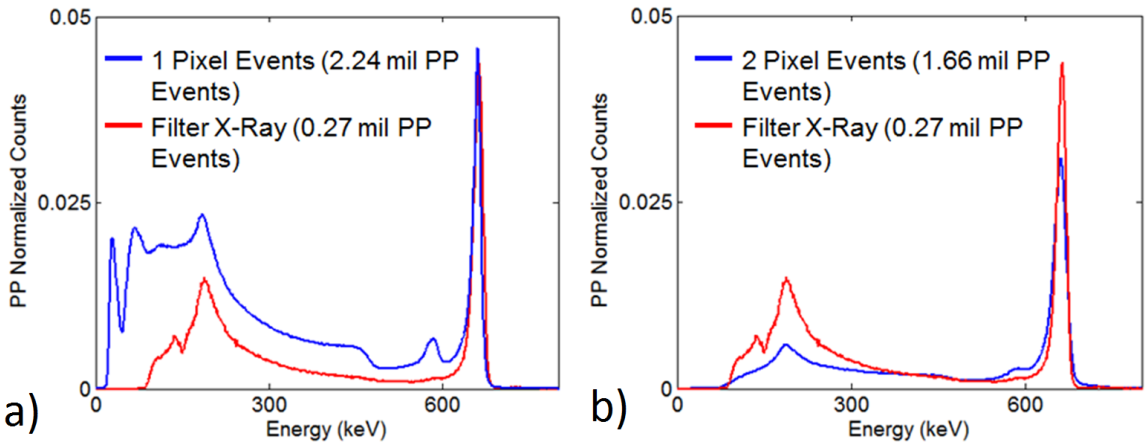

Figure 7.5: a) Single-pixel spectrum (blue curve) and x-ray filtered spectrum (red curve). b) Two-pixel spectrum (blue curve) and x-ray filtered spectrum (red curve).

7.2.2 Improving Multiple Pixel Energy Resolutions

As discussed in Sec. 3.3.5, the energy resolution of TlBr detectors can be improved by identifying Tl characteristic x-ray events and adding back the exact x-ray energy instead of the reconstructed energy. Using this method, the energy resolution for multiple pixel events can improve from

$$R = \frac{2.35\sqrt{E}}{E} \tag{7.1}$$

to:

$$R = \frac{2.35\sqrt{E - E_{Tl}}}{E} \tag{7.2}$$

where E is the deposited energy and E_{Tl} is the Tl characteristic x-ray energy.

In practice, the process is more complicated because Tl has four significant characteristic x-rays. Fig. 7.6 shows simulated characteristic x-ray peaks assuming 0.02%, 1%, and 2% FWHM at 662 keV. When the energy resolution was near perfect (Fig. 7.6a), all four peaks were resolvable. At 1% FWHM energy resolution, there were two groupings separated by about 10 keV. At 2% FWHM, similar to what is currently achieved on the 11 x 11 TlBr detectors, only a single peak was observed. This was

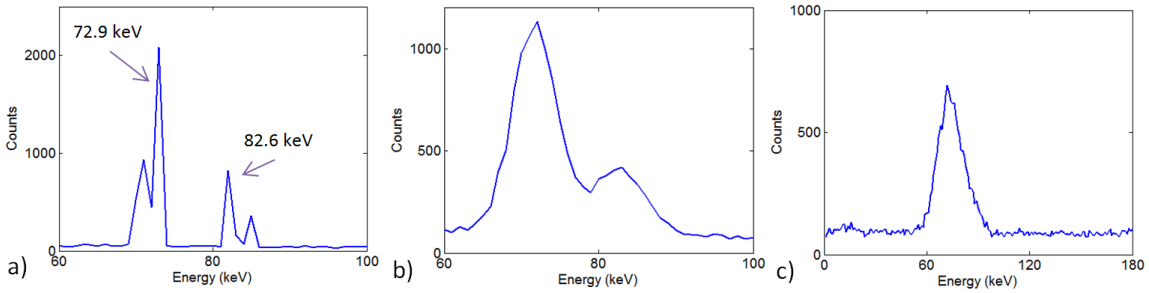

Figure 7.6: Geant4 simulated x-ray regions for TlBr detectors with a) 0.02% b) 1%, and c) 2% energy resolution (FWHM at 662 keV).

consistent with the single x-ray peak observed in Fig. 7.4b.

Because current energy resolution is limited to 2 - 2.5% for 11 x 11 TlBr detectors, only a single filtering window could be applied to identify x-ray events. To improve energy resolution, multiple-pixel events containing at least one event with energy between 68 keV and 82 keV were assigned an energy of exactly 72.9 keV (the most prominent characteristic x-ray energy) during reconstruction. Fig. 7.7 shows the photopeak for experimental data before and after the x-ray filter was applied. As expected, two pixel events showed the most improvement, improving from 3.84% to 3.44% FWHM at 662 keV. This resulted in an overall improvement of 0.1% for all events. In addition to improved energy resolution, the photopeak centroid decreased slightly because every identified x-ray event was set to 72.9 keV, which was below the average x-ray energy. The improvement was significant, but not extreme because only a single x-ray window was applied. Once the overall resolution improves for 11 x 11 detectors and four x-ray windows can be applied, the improvement should be more significant. Using four x-ray windows will also remove the systematic photopeak centroid decrease observed when the filter was applied.

7.3 Compton Imaging

Compton imaging was possible with the 11 x 11 pixelated TlBr detectors because they were 3D position and energy sensitive. Additionally, because the 11 x 11 detec-

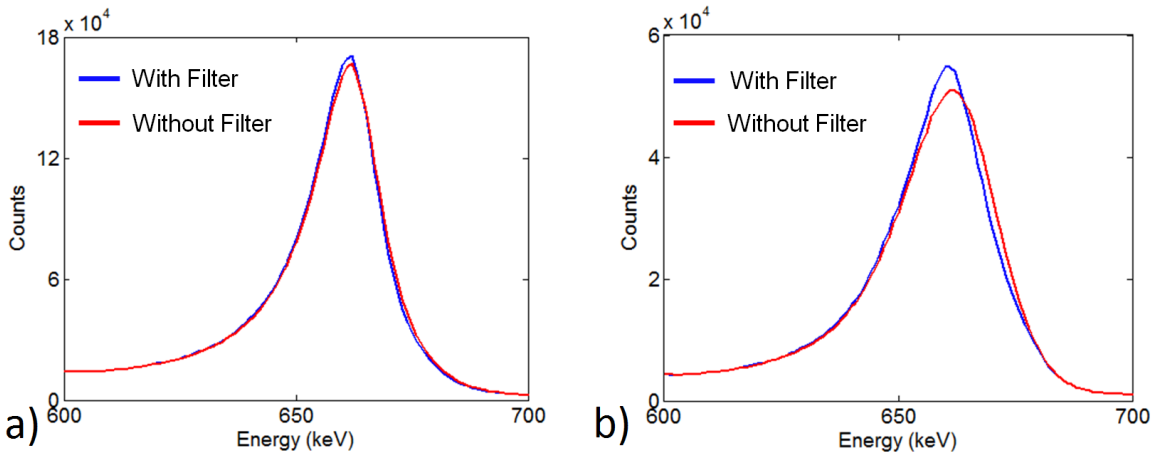

Figure 7.7: Zoom-in of the 662 keV region before and after the x-ray filter was applied to a) all events and b) two-pixel events.

tors (12 x 12 x 5 mm^3) were much larger than the 3 x 3 detectors (5 x 5 x 5 mm^3), the average distance between interactions was greater. Compared to energy resolution, Doppler broadening, and coherent scattering, interaction position uncertainty is the largest contributor to the source direction uncertainty at 662 keV for pixelated detectors with approximately 1 mm pixel pitch [51]. A large spacing between interaction locations will significantly decrease the relative position uncertainty and reduce the source direction uncertainty. For this reason, side-neighbor events, which constitute the smallest distance between interactions, are typically discarded for CZT or TlBr Compton imaging. All events in 3 x 3 pixelated detectors are side-neighbor events, therefore, image quality is very poor.

Fig. 7.8 shows the spectra and images from an 11 x 11 pixelated TlBr detector when ^{137}Cs and ^{60}Co sources were placed on the top and side of the detector box. The images were created using UM Imaging [52]. The top image corresponds to counts in the spectrum near the ^{137}Cs photopeak (highlighted in the top spectrum) and the bottom image corresponds to counts in the spectrum near the ^{60}Co photopeaks (highlighted in the bottom spectrum). It is clear that the two source directions were distinguishable. The ^{60}Co source direction was separated from the ^{137}Cs source direction by approximately 90 ° in both azimuthal and polar angles. The

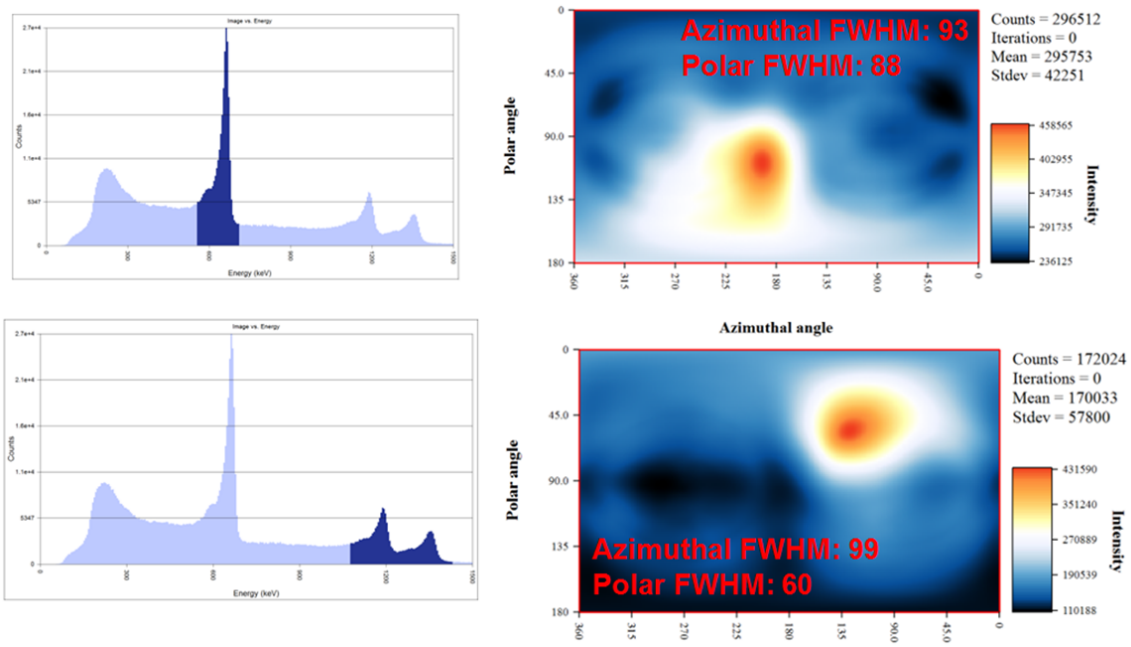

Figure 7.8: Top Row: Compton image of the selected ^{137}Cs photopeak. Bottom Row: Compton image of the selected ^{60}Co photopeaks. The sources were placed on the top and side of the detection box.

TlBr detector was only 5 mm thick, therefore, the resulting images had worse angular resolutions compared to thick CZT detectors [4, 51]. Compton imaging performance should improve once detector volumes increase.

CHAPTER VIII

Summary and Future Work

8.1 Summary

In this thesis, it was shown that TlBr detectors achieved 0.94% FWHM at 662 keV for all single-pixel events, 0.86% FWHM when the best pixel was selected, and 0.72% when the best pixel and best depth were selected. However, these results were limited to stable performance at $-20\,^{\circ}\mathrm{C}$. Using depth-dependent signal analysis, detectors were categorized into 1) good bulk material with good surface properties, 2) good bulk material with poor surface properties, and 3) poor bulk material. Detectors from the second and third categories were refabricated to show that depth-dependent signal analysis correctly attributed poor performance to surface effects in category 2 detectors and bulk effects in category 3 detectors.

Some TlBr detectors exhibited transient performance after applied bias at $-20\,^{\circ}\mathrm{C}$. This conditioning phase was characterized by improved electron drift velocity and energy resolution. Prior to this work, it was unknown whether the drift velocity improvement was caused by an improved electric field or electron mobility. From this work, it was shown that the charged impurity concentration inside the detector decreased as a result of applied bias. This caused the electric field to improve and stabilize, which in turn, improved and stabilized the energy resolution. Conditioning the detectors multiple times at different biases showed that the conditioning mecha-

nism relaxes without applied bias and that the conditioning rate was dependent on the applied bias. Therefore, a higher bias could be applied to condition the detector more quickly. After the device conditions, the bias could be lowered for normal operation.

Proper depth reconstruction is required for imaging, detector diagnostics, and depth correction. Some TlBr detectors showed relatively high hole mobility, complicating the cathode-to-anode ratio method for calculating depth. The effectiveness of different algorithms (one-part linear fit, two-part linear fit, and Newton-Raphson-Timing hybrid) was demonstrated on detectors with varying degrees of hole mobility. In all cases, the interaction depth was reconstructed without significantly degrading the position resolution.

Prior to this work, it was well-known that TlBr detectors polarize during room-temperature operation. The current understanding was that ionic conduction caused a reduction in the internal field which resulted in poor performance. More recent work suggested that interactions between the electrode and bulk material caused the device degradation. By measuring the internal electric field and correlating it to device performance, and by using depth-dependent signal analysis to isolate polarization effects to the surface, it was shown that electrode interactions with the bulk material is more likely the cause of polarization. This was further demonstrated when the detectors returned to performance after they were polarized and refabricated; the refabrication strictly occurred on the surface, leaving the bulk unaffected. The depth-dependent signal analysis and refabrication isolated polarization degradation to within 0.5 mm of the anode electrode.

Finally, good performance on large 11 x 11 pixelated detectors was demonstrated. Detector 935-43AS6 achieved 2.06% FWHM at 662 keV for single-pixel events at $-20\,^{\circ}\mathrm{C}$. The 70-80 keV Tl characteristic x-rays were used to identify photoelectric interactions and improve the two-pixel energy resolution from 3.84% to 3.44% FWHM

at 662 keV. Additionally, Compton imaging was demonstrated for the first time on TlBr detectors.

8.2 Future Work

While TlBr is a promising alternative to CZT for room-temperature gamma-ray spectroscopy and imaging, significant advancements are required for it to be a competitive replacement. The biggest challenge is long-term stability at room-temperature. While this work was able to confirm that polarization was the result of surface reactions, future work must determine how the surface reactions can be mitigated. Detector manufacturers must drive the development of new surface preparation and electrode materials, however, the depth-dependent signal analysis developed by the University of Michigan Orion group will be invaluable in determining the effectiveness of these new processes and materials. Part of this work should also include working with other TlBr vendors, especially those using novel Tl electrodes to stop polarization. Currently, detectors with Tl electrodes have only been tested up to 24 hours of continuous operation. Future work should also include testing these devices for longer periods of time (months) to ensure long-term room-temperature stability.

Throughout the last four years of this work, many detectors have been tested multiple times. In some cases, the different tests occurred months to years apart. Between testings, the detectors were stored without bias in a desiccator. Table 8.1 summarizes the performance of detector 58A3L after multiple tests. The time between the first and last test was over three years. It is clear from Table 8.1 that degradation occurred during storage. The overall energy resolution and difference between the best and worst pixels (a measure of the performance uniformity) both got worse.

The degradation was not the result of the applied bias during testing because no degradation was observed when the detector was tested multiple times within a single month. This has been observed on many other detectors as well. Preliminary depth-

Table 8.1: Performance of detector 58A3L after multiple tests. The detector was stored without bias in a desiccator between tests. The listed resolutions are in % FWHM at 662 keV.

Test Date	Overall Resolution (% FWHM)	Best Pixel Resolution (% FWHM)	Worst Pixel Resolution (% FWHM)
July 2013	1.67	1.47	1.99
Dec. 2013	1.63	1.29	3.09
Mar. 2014	2.57	1.74	3.80
Oct. 2015	3.95	2.40	5.50

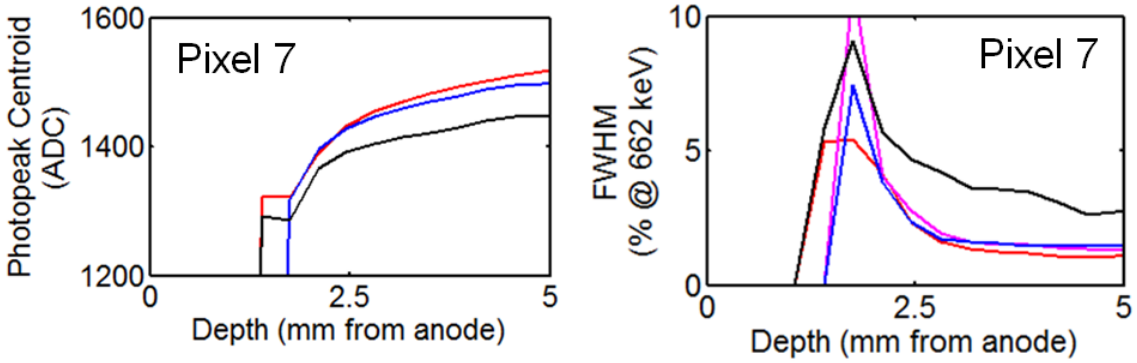

Figure 8.1: Depth-dependent a) photopeak centroids and b) energy resolution for detector 58A3L. The magenta curve is from July 2013, the red curve is from December 2013, the blue curve is from March 2014 and the black curve is from October 2015. The data are shown for pixel 7 and are representative of all the pixels.

dependent signal analysis showed uniform degradation across all depths (see Fig. 8.1), indicating a surface effect. Future work should include determining the cause of the degradation and finding ways to mitigate it. For example, the degradation could be caused by surface oxidation; a protective sealant could be used to encapsulate the detectors.

Finally, more development is required on the 11 x 11 TlBr detectors, which degraded significantly after initial testing. While a strong proof-of-principle was demonstrated in this work, future work should concentrate on leveraging the advantages of TlBr to improve imaging. For example, coded aperture imaging, which would benefit from the high-efficiency and large photoelectric cross-section of TlBr, should be implemented. Once long-term room-temperature stability is achieved with TlBr, hand-held

radiation detectors should be developed. Small volumes are required for hand-help devices, making high-efficiency TlBr a natural material choice.

BIBLIOGRAPHY

[1] Glen F. Knoll. *Radiation Detection and Measurements*. John Wiley & Sons, Inc., New York, fourth edition, 2010.

[2] Canberra Industires Inc. NAIS-2x2 NaI(Tl) LED Temperature-Stabilized Scintillation Detector. http://www.canberra.com/products/detectors/pdf/NAIS-2x2-SS-C38656.pdf, 2011. [Online; accessed June 2015].

[3] Peter R. Menge, G. Gautier, A. Iltis, C. Rozsa, and V. Solovyev. Performance of large lanthanum bromide scintillators. *Nucl. Instruments Methods Phys. Res. Sect. A Accel. Spectrometers, Detect. Assoc. Equip.*, 579(1):6–10, aug 2007.

[4] H3D Website. Polaris H: Gamma Ray Imaging Spectrometers for Nuclear Power Plants. http://h3dgamma.com/nuclearProducts.html. [Online; accessed July 2015].

[5] P. N. Luke. Single-polarity charge sensing in ionization detectors using coplanar electrodes. *Appl. Phys. Lett.*, 65(22):2884–2886, 1994.

[6] Z He, W Li, G F Knoll, D K Wehe, J Berry, and C M Stahle. 3-D position sensitive CdZnTe gamma-ray spectrometers. *Nucl. Instruments Methods Phys. Res. Sect. A Accel. Spectrometers, Detect. Assoc. Equip.*, 422:173–178, 1999.

[7] T. Takahashi and S. Watanabe. Recent progress in CdTe and CdZnTe detectors. *IEEE Trans. Nucl. Sci.*, 48(4):950–959, 2001.

[8] Yuefeng Zhu, Stephen E. Anderson, and Zhong He. Sub-Pixel Position Sensing for Pixelated, 3-D Position Sensitive, Wide Band-Gap, Semiconductor, Gamma-Ray Detectors. *IEEE Trans. Nucl. Sci.*, 58(3):1400–1409, jun 2011.

[9] Feng Zhang, Cedric Herman, Zhong He, Gianluigi De Geronimo, Emerson Vernon, and Jack Fried. Characterization of the H3D ASIC Readout System and 6.0 cmˆ3 3-D Position Sensitive CdZnTe Detectors. *IEEE Trans. Nucl. Sci.*, 59(1):236–242, feb 2012.

[10] M. Streicher, Y. Zhu, F. Zhang, Y. A. Boucher, C. G. Wahl, H. Yang, and Z. He. A portable 2 x 2 digital 3d czt imaging spectrometer system. In *Nuclear Science Symposium Conference Record (NSS/MIC), IEEE*, 2014.

[11] Alexei Churilov, William M. Higgins, Guido Ciampi, Hadong Kim, L Cirignano, Fred Olschner, and K. S. Shah. Purification, crystal growth and detector performance of TlBr. *Proc. SPIE*, 7079:70790K–70790K–8, 2008.

[12] H Kim, L Cirignano, A Churilov, G Ciampi, W Higgins, F Olschner, and Kanai Shah. Developing Larger TlBr Detectors Detector Performance. *IEEE Trans. Nucl. Sci.*, 56(3):819–823, 2009.

[13] W.R. Willig. Mercury iodide as a gamma spectrometer. *Nucl. Instruments Methods*, 96(4):615–616, nov 1971.

[14] A. Holzer and M. Schieber. Reduction of Polarization in Mercuric Iodide Nuclear Radiation Detectors. *IEEE Trans. Nucl. Sci.*, 27(1):266–271, feb 1980.

[15] Vernon Gerrish and Lodewijk van den Berg. Improved yield of high resolution mercuric iodide gamma-ray spectrometers. *Nucl. Instruments Methods Phys. Res. Sect. A Accel. Spectrometers, Detect. Assoc. Equip.*, 299(1-3):41–44, dec 1990.

[16] Vernon Gerrish. Polarization and gain in mercuric iodide gamma-ray spectrometers. *Nucl. Instruments Methods Phys. Res. Sect. A Accel. Spectrometers, Detect. Assoc. Equip.*, 322(3):402–413, nov 1992.

[17] J.E. Baciak and Zhong He. Long-term stability of 1-cm thick pixelated HgI gamma-ray spectrometers operating at room temperature. *IEEE Trans. Nucl. Sci.*, 51(4):1886–1894, 2004.

[18] L. J. Meng, Z. He, B. Alexander, and J. Sandoval. Spectroscopic performance of thick HgI2 detectors. *IEEE Trans. Nucl. Sci.*, 53(3):1706–1712, 2006.

[19] Robert Hofstadter. Thallium Halide Crystal Counter. *Phys. Rev.*, 72(11):1120–1121, dec 1947.

[20] K.S. Shah, J.C. Lund, F. Olschner, L. Moy, and M.R. Squillante. Thallium bromide radiation detectors. *IEEE Trans. Nucl. Sci.*, 36(1):199–202, 1989.

[21] F. Olschner, M. Toledo-Quinones, K.S. Shah, and J.C. Lund. Charge carrier transport properties in thallium bromide crystals used as radiation detectors. *IEEE Trans. Nucl. Sci.*, 37(3):1162–1164, jun 1990.

[22] F. Olschner, K.S. Shah, J.C. Lund, J. Zhang, K. Daley, S. Medrick, and M.R. Squillante. Thallium bromide semiconductor X-ray and γ-ray detectors. *Nucl. Instruments Methods Phys. Res. Sect. A Accel. Spectrometers, Detect. Assoc. Equip.*, 322(3):504–508, nov 1992.

[23] K Hitomi, M Matsumoto, O Muroi, T Shoji, and Y Hiratate. Characterization of thallium bromide crystals for radiation detector applications. *J. Cryst. Growth*, 225(2-4):129–133, may 2001.

[24] K. Hitomi, O. Muroi, M. Matsumoto, R. Hirabuki, T. Shoji, T. Suehiro, and Y. Hiratate. Recent progress in thallium bromide detectors for X- and γ-ray spectroscopy. *Nucl. Instruments Methods Phys. Res. Sect. A Accel. Spectrometers, Detect. Assoc. Equip.*, 458(1-2):365–369, feb 2001.

[25] J. Vaitkus, J. Banys, V. Gostilo, S. Zatoloka, A. Mekys, J. Storasta, and A. Žindulis. Influence of electronic and ionic processes on electrical properties of TlBr crystals. *Nucl. Instruments Methods Phys. Res. Sect. A Accel. Spectrometers, Detect. Assoc. Equip.*, 546(1-2):188–191, jul 2005.

[26] Keitaro Hitomi, Tadayoshi Shoji, and Keizo Ishii. Advances in TlBr detector development. *J. Cryst. Growth*, 379:93–98, sep 2013.

[27] T. Onodera, K. Hitomi, T. Shoji, Y. Hiratate, and H. Kitaguchi. Spectroscopic performance of pixellated thallium bromide detectors. *IEEE Trans. Nucl. Sci.*, 52(5):1999–2002, oct 2005.

[28] H. Kim, A. Churilov, G. Ciampi, L. Cirignano, W. Higgins, S. Kim, P. ODougherty, F. Olschner, and Kanai Shah. Continued development of thallium bromide and related compounds for gamma-ray spectrometers. *Nucl. Instruments Methods Phys. Res. Sect. A Accel. Spectrometers, Detect. Assoc. Equip.*, 629(1):192–196, feb 2011.

[29] T Onodera, K Hitomi, T Shoji, and Y Hiratate. Pixellated thallium bromide detectors for gamma-ray spectroscopy and imaging. *Nucl. Instruments Methods Phys. Res. Sect. A Accel. Spectrometers, Detect. Assoc. Equip.*, 525(1-2):199–204, jun 2004.

[30] Keitaro Hitomi, Tadayoshi Shoji, and Yoshio Niizeki. A method for suppressing polarization phenomena in TlBr detectors. *Nucl. Instruments Methods Phys. Res. Sect. A Accel. Spectrometers, Detect. Assoc. Equip.*, 585(1-2):102–104, jan 2008.

[31] Burçin Dönmez, Zhong He, Hadong Kim, Leonard J. Cirignano, and Kanai S. Shah. The stability of TlBr detectors at low temperature. *Nucl. Instruments Methods Phys. Res. Sect. A Accel. Spectrometers, Detect. Assoc. Equip.*, 623(3):1024–1029, nov 2010.

[32] Crystal L Thrall, William R Kaye, Zhong He, Hadong Kim, Leonard Cirignano, and Kanai Shah. Transient Behavior in TlBr Gamma-Ray Detectors and Its Analysis Using 3-D Position Sensing. *iee*, 60(2):1162–1167, 2013.

[33] J. Vaitkus, V. Gostilo, R. Jasinskaite, a. Mekys, a. Owens, S. Zatoloka, and a. Zindulis. Investigation of degradation of electrical and photoelectrical properties in TlBr crystals. *Nucl. Instruments Methods Phys. Res. Sect. A Accel. Spectrometers, Detect. Assoc. Equip.*, 531(1-2):192–196, sep 2004.

[34] S R Bishop, G Ciampi, C D Lee, M Kuhn, H L Tuller, W Higgins, and K S Shah. Ionic Conductivity of TlBr Candidate Gamma Ray Detector. *IEEE Trans. Nucl. Sci.*, 59(5):2424–2427, 2012.

[35] V. Kozlov, M. Kemell, M. Vehkamäki, and M. Leskelä. Degradation effects in TlBr single crystals under prolonged bias voltage. *Nucl. Instruments Methods*

Phys. Res. Sect. A Accel. Spectrometers, Detect. Assoc. Equip., 576(1):10–14, jun 2007.

[36] A. M. Conway, L. F. Voss, A. J. Nelson, P. R. Beck, T. A. Laurence, R. T. Graff, R. J. Nikolic, S. A. Payne, L. J. Cirignano, and Kanai Shah. Fabrication Methodology of Enhanced Stability Room Temperature TlBr Gamma Detectors. *IEEE Trans. Nucl. Sci.*, 60(2):1231–1236, apr 2013.

[37] Will Koehler, Zhong He, Crystal Thrall, Sean O Neal, Hadong Kim, Leonard Cirignano, and Kanai Shah. Quantitative Investigation of Room-Temperature Breakdown Effects in Pixelated TlBr Detectors. *IEEE Trans. Nucl. Sci.*, 61(5):2573–2578, 2014.

[38] Keitaro Hitomi, Yohei Kikuchi, Tadayoshi Shoji, and Keizo Ishii. Improvement of energy resolutions in TlBr detectors. *Nucl. Instruments Methods Phys. Res. Sect. A Accel. Spectrometers, Detect. Assoc. Equip.*, 607(1):112–115, aug 2009.

[39] Lars F. Voss, Adam M. Conway, Robert T. Graff, Patrick R. Beck, Rebecca J. Nikolic, Art J. Nelson, Stephen a. Payne, Hadong Kim, Len Cirignano, and Kanai Shah. Surface processing of TlBr for improved gamma spectroscopy. *IEEE Nucl. Sci. Symp. Conf. Rec.*, pages 3746–3748, 2010.

[40] A. M. Conway, L. F. Voss, A. J. Nelson, P. R. Beck, R. T. Graff, R. J. Nikolic, S. a. Payne, H. Kim, L. J. Cirignano, and K. Shah. Long-term room temperature stability of TlBr gamma detectors. *SPIE 8142, Hard X-Ray, Gamma-Ray, Neutron Detect. Phys. XIII*, 8142:81420J, 2011.

[41] W. Shockley. Currents to Conductors Induced by a Moving Point Charge. *J. Appl. Phys.*, 9(10):635, apr 1938.

[42] S. Ramo. Currents Induced by Electron Motion. *Proc. IRE*, 27(9):584–585, sep 1939.

[43] Zhong He, Glenn F Knoll, David K Wehe, Ronald Rojeski, Carlos H Mastrangelo, Mark Hammig, Carla Barrett, and Akira Uritani. 1 -D position sensitive single carrier semiconductor detectors. *Nucl. Instruments Methods Phys. Res. Sect. A Accel. Spectrometers, Detect. Assoc. Equip.*, 380:228–231, 1996.

[44] Feng Zhang. *Events Reconstruction in 3-D Position Sensitive CdZnTe Gamma Ray Spectrometers*. PhD Thesis, University of Michigan, 2005.

[45] W. Li, Z. He, G.F. Knoll, D.K. Wehe, and C.M. Stahle. Spatial variation of energy resolution in 3-D position sensitive CZT gamma-ray spectrometers. *IEEE Trans. Nucl. Sci.*, 46(3):187–192, jun 1999.

[46] Crystal Thrall. *Alternative Wide-Band-Gap Materials for Gamma-Ray Spectroscopy*. PhD Thesis, University of Michigan, 2013.

[47] M Singh. An electronically collimated gamma camera for single photon emission computed tomography. Part I: Theoretical considerations and design criteria. *Med. Phys.*, 10(4):421–7, jan 1983.

[48] M Singh and D Doria. An electronically collimated gamma camera for single photon emission computed tomography. Part II: Image reconstruction and preliminary experimental measurements. *Med. Phys.*, 10(4):428–35, jan 1983.

[49] Jason Jaworski. *Compton Imaging Algorithms for Position-Sensitive Gamma-Ray Detectors in the Presence of Motion*. PhD Thesis, University of Michigan, 2013.

[50] C.E. Lehner. 4/spl pi/ Compton imaging using a 3-D position-sensitive CdZnTe detector via weighted list-mode maximum likelihood. *IEEE Trans. Nucl. Sci.*, 51(4):1618–1624, aug 2004.

[51] Dan Xu. *Gamma-ray imaging and polarization measure using 3-d position-sensitive CdZnTe detectors*. PhD Thesis, University of Michigan, 2006.

[52] Chris Wahl. *Imaging, Detection, and Identification Algorithms for Position-Sensitive Gamma-Ray Detectors*. PhD Thesis, University of Michigan, 2011.

[53] Yuefeng Zhu. *Digital Signal Processing Methods for Pixelated 3-D Position Sensitive Room-Temperature Semiconductor Detectors*. PhD Thesis, University of Michigan, 2012.

[54] Will Koehler, Zhong He, Sean O'Neal, Hao Yang, Hadong Kim, Leonard Cirignano, and Kanai Shah. Quantification of the Conditioning Phase in Cooled Pixelated TlBr Detectors. *IEEE Trans. Nucl. Sci.*, 62(4):1785–1790, aug 2015.

[55] Ijaz-ur Rahman and Robert Hofstadter. Thallium halide radiation detectors. *Phys. Rev. B*, 29(6), 1984.

[56] Qing Wang, Seigo Ito, Michael Grätzel, Francisco Fabregat-Santiago, Iván Mora-Seró, Juan Bisquert, Takeru Bessho, and Hachiro Imai. Characteristics of high efficiency dye-sensitized solar cells. *J. Phys. Chem. B*, 110(50):25210–21, dec 2006.

[57] Juan Bisquert, Francisco Fabregat-Santiago, Ivan Mora-Sero, Germa Garcia-Belmonte, and Sixto Gimenez. Electron Lifetime in Dye-Sensitized Solar Cells: Theory and Interpretation of Measurements. *J. Phys. Chem. C*, 113(40):17278–17290, oct 2009.

[58] R. James T. Schlesinger. *Semiconductors for Room Temperature Nuclear Detection Applications, series. Semiconductors and Semimetals*. Academic Press, 1995.

[59] Z. He, G. F. Knoll, and D. K. Wehe. Direct measurement of product of the electron mobility and mean free drift time of CdZnTe semiconductors using position sensitive single polarity charge sensing detectors. *J. Appl. Phys.*, 84(10):5566, nov 1998.

[60] K. A. Jones, A. Datta, K. G. Lynn, and L. A. Franks. Variations in $\mu\tau$ measurements in cadmium zinc telluride. *J. Appl. Phys.*, 107(12):123714, jul 2010.

[61] Alireza Kargar, Andrew M. Jones, Walter J. McNeil, Mark J. Harrison, and Douglas S. McGregor. CdZnTe Frisch collar detectors for γ-ray spectroscopy. *Nucl. Instruments Methods Phys. Res. Sect. A Accel. Spectrometers, Detect. Assoc. Equip.*, 558(2):497–503, mar 2006.

[62] A.E. Bolotnikov, G.S. Camarda, G.A. Carini, M Fiederle, L. Li, Douglas S. McGregor, Walter J. McNeil, G.W. Wright, and R.B. James. Performance Characteristics of Frisch-Ring CdZnTe Detectors. *IEEE Trans. Nucl. Sci.*, 53(2):607–614, 2006.

[63] GENAT4 Website. Geant4: a toolkit for the simulation of the passage of particles through matter. https://geant4.web.cern.ch/geant4/. [Online; accessed Jan 2016].

[64] Maxwell Website. Maxwell: Explore engineering simulation. http://www.ansys.com/. [Online; accessed Jan 2016].

[65] Keitaro Hitomi, Toshiyuki Onodera, Tadayoshi Shoji, Yukio Hiratate, and Zhong He. TlBr Gamma-Ray Spectrometers Using the Depth Sensitive Single Polarity Charge Sensing Technique. *IEEE Trans. Nucl. Sci.*, 55(3):1781–1784, jun 2008.

[66] J.E. Baciak. Spectroscopy on thick HgI2 detectors: a comparison between planar and pixelated electrodes. In *2002 IEEE Nucl. Sci. Symp. Conf. Rec.*, volume 1, pages 439–443. IEEE, 2002.

[67] I. Jung, H. Krawczynski, A. Burger, M. Guo, and M. Groza. Detailed studies of pixelated CZT detectors grown with the modified horizontal Bridgman method. *Astropart. Phys.*, 28(4-5):397–408, dec 2007.

[68] Willy Kaye. *Energy and Position Reconstruction in Pixelated CdZnTe Detectors.* PhD Thesis, University of Michigan, 2012.

[69] Yvan A. Boucher, Feng Zhang, Willy Kaye, and Zhong He. New measurement technique for the product of the electron mobility and mean free drift time for pixelated semiconductor detectors. *Nucl. Instruments Methods Phys. Res. Sect. A Accel. Spectrometers, Detect. Assoc. Equip.*, 671:1–5, apr 2012.

[70] W. Koehler, M. Streicher, Sean O'Neal, and Zhong He. A correction factor to the two-bias method for determining mobility-lifetime products in pixelated detectors. *IEEE Trans. Nucl. Sci.*, 2016. Accepted.

[71] S. R. Bishop, W. Higgins, G. Ciampi, A. Churilov, K. S. Shah, and H. L. Tuller. The Defect and Transport Properties of Donor Doped Single Crystal TlBr. *J. Electrochem. Soc.*, 158(2):J47, feb 2011.